Study of the Limits of Single-Photon Detection in Lumped Element Kinetic Inductance Detectors

Josie Dzifa Akua Parrianen

A thesis submitted to Cardiff University

in partial fulfillment of the requirements for the degree of

Doctor of Philosophy

Defended: 25th February 2019

Pour ma famille. Toujours.

Acknowledgements

I would like to take the opportunity to thank the many people who have supported and guided me through this endeavour. First must be my supervisor Dr. Simon Doyle. His deep understanding of LEKIDs have helped me to understand concepts in very different ways. We have had many long and interesting conversations trying to understand some of my results. He has also been very supportive in the human context, for which I am incredibly grateful. I couldn't have asked for a better supervisor. Thank you. I would also like to thank Chris Dunscombe for his technical support and enduring patience; Andreas Papageorgiou for his incredible insights and never-ending excitement for interesting data; Pete Barry for technical support; and the rest of the KIDs group at Cardiff, without whom this journey would not have been enjoyable.

I must also thank my friends. Never once have they lost faith in my ability and resolve to complete this work. In that, and for them, I have managed to keep my resolve. Thank you for keeping me within the realms of reality.

And to the wonderful beings at Cog; particularly those of you at No. 5. Thank you for letting me take over the kitchen. Most importantly thank you for our random chats – it kept me sane.

Lastly, I would like to thank my family. Maman, you've helped guide me along the way and now I'm here. I could never have done it without you. Papa, although you probably don't realise it, your insights have led me here. I am proud to be your daughter. Uncle R, you have always helped put perspective on the worth of things. Nana, thank you for all your love and support. And to my brother J, you have steered me true. I am forever grateful.

Abstract

Kinetic inductance detectors (KIDs) have shown promising single-photon detection capabilities. However, there has also been a consistent deviation from the limit in energy resolution predicted by Poisson statistics. The consistent underperformance suggests some additional mechanism has not been taken into account. The work in this thesis has taken the novel approach of using aluminium (Al) lumped element (LE) KIDs to model single-photon detection based on Mattis-Bardeen and Kaplan theory.

This work has demonstrated generation-recombination (GR) noise limited performance predicted by theory, when taking into account the quasiparticle density and lifetime saturation at low temperatures. The model requires a single fitting parameter that accounts for the quasiparticle generation efficiency η. This work shows $\eta = 0.4$ is more appropriate for 30 nm Al film.

It has also been recognised, through simulation and measurement, that there is a position dependence in the response to photon absorption, which is dependent upon LEKID architecture. An attempt was made to mitigate this effect by using a hybrid device: an additional niobium (Nb) absorbing layer is used to cover the assumed non-responsive regions of the LEKID structure. However, large amounts of scatter in resonator position across the test array – thought to be due to processing effects – have made it difficult to identify between Al and hybrid devices. Experimental procedures were developed to assist device identification with some degree of success but further development work is required. Nonetheless, the same test array has shown single-photon detection in Al LEKIDs at visible and near-infrared wavelengths.

Contents

List of Figures

List of Tables

Chapter 1

Introduction and Background

1.1 Thesis Outline

This thesis presents the development and testing of single-photon detection in aluminium (Al) lumped element kinetic inductance detectors (LEKIDs). Kinetic inductance detectors (KIDs) are now well-known cryogenic photon detectors. They are competitive photometry detectors with broad applications and have recently been proven as good energy-resolving, single-photon detectors. The work presented in this thesis aims to show how the underlying physics both allows and limits single-photon detection in LEKIDs. The contents of the following chapters are outlined as follows:

Chapter 1: Introduction and Background

This thesis summary and an introduction to the possible application of energy-resolving, single-photon LEKIDs. The requirements and characterisation of single-photon detectors (SPDs) are described along with examples of popular SPDs. LEKIDs

are then introduced with an overview of how they operate as photon detectors.

Chapter 2: Fundamental Physics of LEKIDs

A complete overview is given of the fundamental physics which determine how LEKIDs are able to generate a response from absorbed photons.

Chapter 3: Optical Response in LEKIDs

The detection principle of LEKIDs is descibed, which brings together the theory described in chapter 2. The noise contributions are also introduced and described in some detail. Based on theory alone, the optical response of LEKIDs is modelled in both steady-state and single-photon detection regimes. The energy resolution and its limitations are also described here. The local dependence of a LEKIDs response is additionally explored.

Chapter 4: Proof of Concept

The first published results of single-photon detection in Al LEKIDs is presented in detail.

Chapter 5: Single-Photon LEKID Design Evolution

An overview of the main design considerations for LEKIDs is given. These include factors which were accounted for in the design process towards an optimised design for single-photon detection in LEKIDs. A thorough description of the pixel designs and the test array design is given.

Chapter 6: Local Response Dependence

The local response dependence of the resonator designs described in Chapter 5 is simulated. The variation in response due to the location, within the meander, of an absorption event is investigated.

Chapter 7: Measurement of Single-Photon Test Array

The results from optical measurements of the single-photon LEKID test array are presented.

Chapter 8: Summary & Future Work

The work in this thesis is summarised and areas for further study are identified.

1.2 Scientific Motivation for Energy-Resolving Detectors

The ultimate sensitivity of a light detector is reaching the ability to resolve the energy of incident photons. Energy-resolving detectors (ERDs) fall under the category of single-photon detectors (SPDs). Note that not all SPDs are energy-resolving; these are referred to as photon counting detectors. Figure 1.1 shows a host of applications for single-photon technology: detection and generation. The quantum information field largely concerns photon counting detectors and photonics predominantly concerns single-photon generation. The remainder of the application areas in Figure 1.1 rely upon a mixture of single-photon technology and can certainly benefit from energy-resolving detectors.

In this section, some of these main applications are discussed. Note that the work in this thesis concerns optical and near-infrared wavelengths, therefore only suitable applications for these wavelengths are included.

1.2.1 Astronomy

There are numerous applications for energy-resolving detectors in astronomy. At the moment, extra-solar planets (exoplanets) are a high priority in astronomy. Several thousand exoplanets have already been discovered [2] but there is a drive to

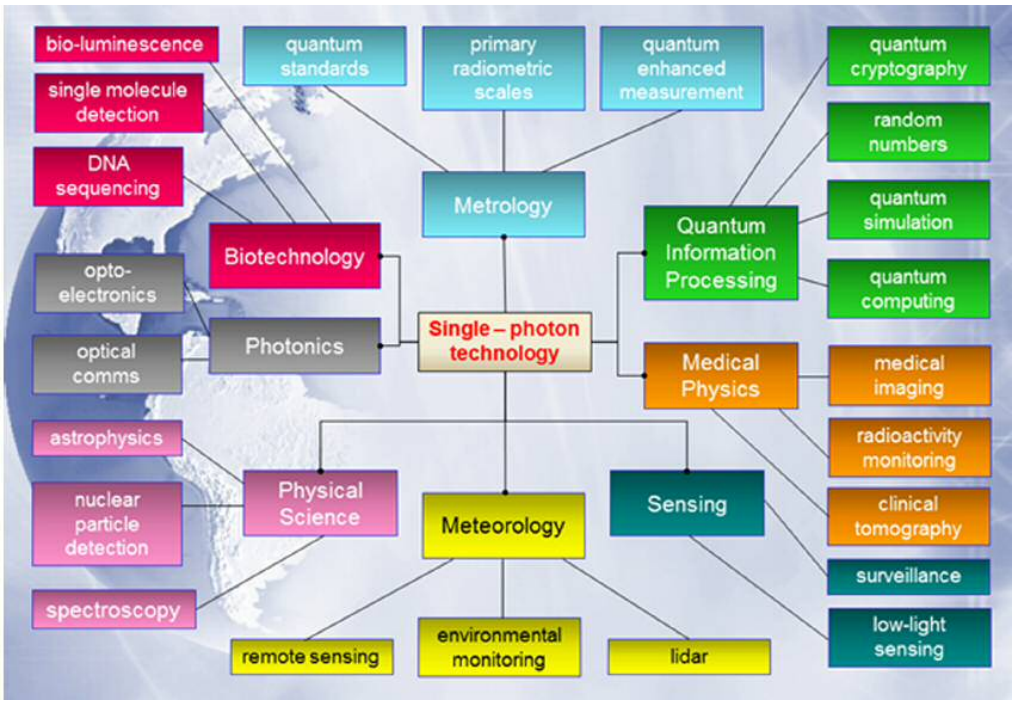

Figure 1.1: Main applications for single-photon detection and generation [1].

further our understanding and broaden the type of exoplanets discovered. There are two primary areas which can improve the exoplanet search: imaging and spectroscopy. Spectroscopy enables identification of the composition of astronomical objects as well as the measurement of redshift. Visible and infra-red spectroscopy can also improve understanding of the composition of interstellar space [3], star formation [4, 5] and galactic structure [6, 7].

1.2.1.1 Imaging

High-contrast imaging

At the time of writing, high contrast imaging is a technique being considered as a means of direct imaging towards exoplanet search and characterisation [8, 9]. Here, the characterisation means spectral analysis i.e. characerisation beyond geometric and physical properties. The vast majority of known exoplanets have been

discovered by indirect methods. For example, radial velocity measurements of a host star can be filtered and mathematical techniques can be applied towards isolating periodic changes due to the infuluence of an orbiting exoplanet. Or transit photometry, where a host star's luminosity is dimmed by the transit of an exoplanet between the star and the observer. Such methods can usually only provide information of the radial size and mass of an exoplanet. These methods also limit the type of exoplanets that can be discovered. The majority of discovered exoplanets are hot Jupiter-type planets: luminous orbiting bodies with large mass. Direct imaging could reveal spectroscopic, photometric and astrometric information and could broaden the typical star-planet separations, and thus exoplanet type.

A major problem with high contrast imaging is the requirement of extreme adaptive optics (EAO): complex optics systems to correct distortions of the incoming light [10]. Current and proposed ground-based instruments also use coronagraphs in conjunction with EAO to add additional correction capabilities [11]. Energy-resolving detectors would likely minimise the EAO requirements and therefore simplify the next-generation instruments.

Lucky imaging

Lucky imaging is a speckle imaging technique which requires a high speed camera with short exposure times to minimise the effects of changes in the Earth's atmosphere. A significant number of images are taken of the same object. These undergo a selection process where the images with the best quality are chosen. The images are then overlaid, placing the brightest pixel of each image in the same reference position. The resulting image depends on the selection process. A 1% selection (where 1% of the best quality images are chosen) can improve the angular resolution by up to 5 times [12]. An example of this is shown in Figure 1.2. Energy-resolving detectors could be more reliable in locating the brightest pixel and would be able to

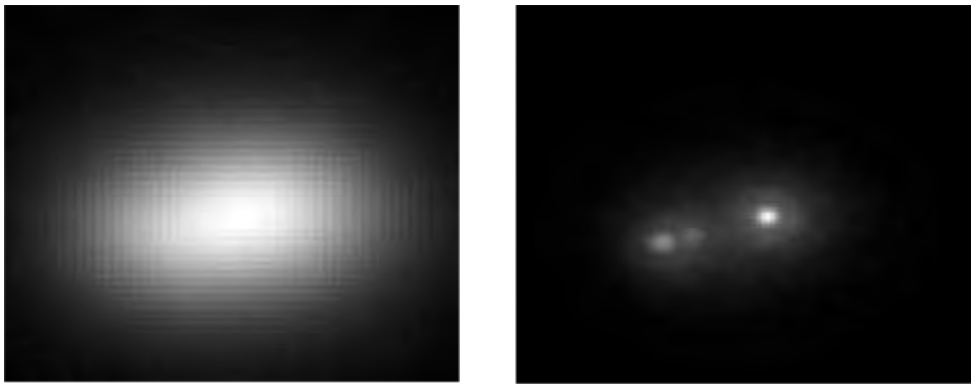

(a) (b)

Figure 1.2: Representation of the lucky imaging selection process. a) Sum of 50,000 z-band (near-infrared) images, each with 25 ms exposure time and b) example of 1% selection: 500 best images averaged [13].

image fainter objects.

1.2.1.2 Spectroscopy

Redshift measurements

The measurement of well-known spectral features can enable measurement of the redshift of very distant objects. One of the most distant objects identified in this way was confirmed using the Hubble Space Telescope (HST) Wide Field Camera 3 (WFC3) [14]. The WFC3 uses charge-coupled devices (CCDs) as the detecting element of the camera. CCDs are essentially photon counting detectors: an absorbed photon will generate an electron, regardless of the photon energy. However, their resolution is limited by the readout electronics which tends to have readout noise of few photons. The WFC3 requires a combination of prisms and grisms - or grating prisms - to perform spectroscopy. An ERD of the same photon energy regime would enable imaging and spectrocopy without the need of prisms and grisms, or combination thereof.

Exoplanets

Only a handful have been spectrally analysed [15]; these tend to be relatively nearby hot Jupiter-type planets which have relatively pronounced transit light curves. At present, there are a number of proposed exoplanet missions [16, 17] which aim to carry out spectroscopy on very low intensity light and shallow light curves; which would characterise the temperature and composition of exoplanet atmospheres. This type of characerisation could reveal markers for extra-terrestial life [18].

1.2.2 Particle Physics

There are a number of particle detection experiments which require more sensitive detectors to improve the experiments' overall sensitivity [19, 20]. The inclusion of energy-resolving detectors could improve the constraints on a number of experiments e.g. neutrinoless double-beta decay [21], neutron detection [22] and neutrino mass [23].

1.2.3 Biotechnology & Medical Physics

1.2.3.1 Medical imaging

At visible and near-infrared wavelengths, the main imaging process is optical coherence tomography (OCT) [24]. The technique uses interferometry and can generate high-resolution images of biological tissue at the micron scale. Use of ERDs could improve the resolution and allow imaging of smaller biological structures.

1.2.3.2 Fluorescent tagging

Fluorescent tagging is another imaging method which tracks biological molecules. With technological advances, research is moving beyond identification of biological molecules and is now attempting to understand what they do, how do they

behave and where they go [25]. Fluorescent tagging makes use of biological molecules which have inherent fluorescence. These can be attached to other molecules of interest. However, their brightness can diminish or their emission can become unstable. Some fluorescent tags and methods can have poor signal-to-noise ratios (SNRs), limiting their application to particular molecules of interest. ERDs could aid the tracking of molecules with poor SNR and thus enhance current understanding of biological molecules of interest.

1.2.4 Remote Sensing

The sensitivity of a detector puts a limit of how distant an object it can detect. Use of ERDs in remote sensing – which includes surveillance and Earth observation (EO) – would improve the distance of detectable objects. They would also improve resolution in low level light conditions. This could mean better quality security imaging and broaden the placement of EO satellites.

1.3 Single-Photon Detectors

SPDs are a well-established technology; there are now SPDs – either photon counting or energy-resolving – for high-energy X-rays [26] down to the significantly lower energies at far-infrared wavelengths [27].

1.3.1 Characteristics

The defining characteristics of single-photon detectors are described below. For a particular detector technology, only a subset of these characteristics apply [1, 28].

1.3.1.1 Photon energy/number resolution

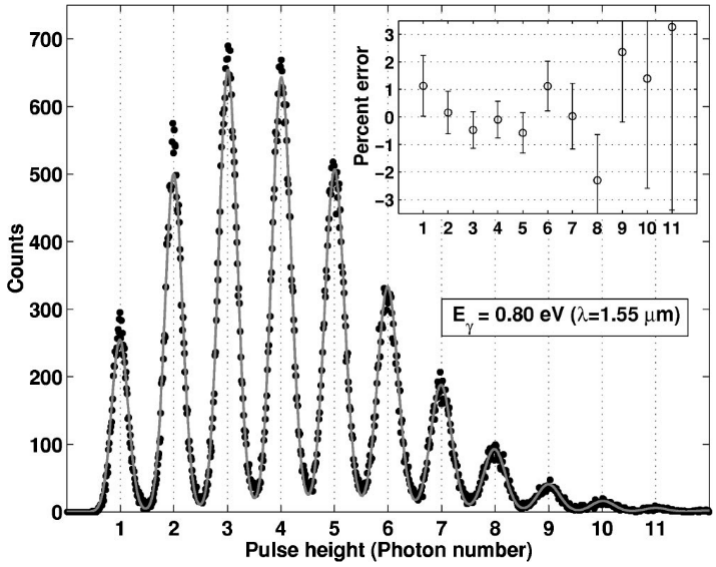

Figure 1.3: example of measured pulse-height distribution of a pulsed laser source (λ = 1550 nm) using a transition edge sensor calorimetric photon counter; with energy resolution 0.120 eV [29].

The primary characteristic of any SPD is its resolution. For a photon counting detector, it is the photon number resolution i.e. the minimum number of photons it can detect for a certain wavelength. For energy-resolving detectors, it is the energy resolution: the minimum photon energy it can detect for a certain wavelength. Figure 1.3 shows an example of a transition edge sensor capable of resolving 1550 nm single-photons. Notice that any energy-resolving detector is also capable of photon counting.

1.3.1.2 Efficiency

All SPDs are dependent on its efficiency. There are two types: detection efficiency and quantum efficiency.

Detection efficiency

Detection efficiency is regarded as the probability that an incident photon will generate a measurable response. For example, a detection efficiency of 0.9 is a limit on the detector such that only 90% of incident photons are detected. Thus an ideal detector would have a detection efficiency of 1, in which all incident photons register a response. This characteristic may also be referred to as optical efficiency and is largely material and fabrication dependent.

Quantum efficiency

Quantum efficiency is defined as the probability that an incident photon will generate an electron-hole pair (for semi-conductor detectors) or break a Cooper pair (for superconducting detectors). For a detector with quantum efficiency of unity, every incident photon will break a pair. Note that this does not mean that the detector will also have a detection efficiency of unity.

1.3.1.3 Dark counts or response

Dark counts (for photon counting detectors) and dark responses (for energy-resolving detectors) are measured detector responses in the absence of incident photons. An ideal SPD would have zero dark counts or response.

1.3.1.4 Timing jitter

Timing jitter is an important characteristic for any SPD which aims to measure the photon arrival time. In practice, there will be a time interval between the absorption of a photon and the corresponding output signal of the detector. Timing jitter is defined as the degree of variation in this time interval. For an ideal SPD, the time interval should be stable and thus have a small timing jitter. The value quoted for timing jitter is taken to be the full-width-at-half-maximum (FWHM) of the histogram of the recorded delay times.

1.3.1.5 Dead time

Dead time is defined as the time at which a detector is unable to register a response of incident photons. This could be due to the readout (i.e. memory buffering) or the detector (e.g. superconducting detector driven normal by incident photons). This characteristic is more associated with photon counting detectors. An ideal SPD would have no dead time.

1.3.1.6 Recovery time

Recovery time is defined as the shortest time duration, after a photon absorption event, for the detection efficiency to return to its steady-state value. This characteristic may not apply to all SPDs. An ideal SPD would have a consistent detection efficiency and thus no recovery time.

1.3.1.7 Response linearity

A detector with response linearity would have an unchanged response regardless of the number of incident photons. This characteristic may not apply to all SPDs.

1.3.1.8 Maximum exposure level

The maximum exposure level is considered to be the photon flux above which the detector undergoes a temporary or permanent change in any of its characteristics. It is likely all SPDs have a maximum exposure level.

1.3.1.9 Noise equivalent power

Noise equivalent power (NEP) is a measure of the equivalent signal power required to achieve a signal-to-noise ratio (SNR) of unity within a 0.5 second integration

time. This characteristic is a conventional measure of a detector's sensitivity. For a generic SPD, the NEP can be defined as [28]

$$NEP = \frac{hc}{\lambda \eta_q} \sqrt{2N_D}, \tag{1.1}$$

where h is Planck's constant, c is the speed of light, λ is the photon wavelength, η_q is the quantum efficiency of the detector and N_D is the dark count rate (for photon counting) or the dark response rate (for energy-resolving).

1.3.2 Energy-Resolving SPDs

To date, there are a host of good SPD technologies, a sample of which can be seen in Table 1.1. The highly sensitive of these are superconducting single-photon detectors (SSPDs). For the applications outlined in Section 1.2, SSPDs are the primary detector choice. With superconducting materials, there are significantly lower dark counts or responses, faster recovery times and improved sensitivities enabling single-photon detection at optical to mid-infrared wavelengths [30].

At the time of writing, the dominant SSPDs are superconducting nanowire single-photon detectors (SNSPDs) and transition edge sensors (TESs). SNSPDs have high detection efficiency, can have low dark counts and are incredibly fast [31, 32]. They are predominantly used as photon-counting detectors but have shown energy-resolving capability; see Table 1.1. TESs are well-established as energy-resolving SPDs and have the best energy resolutions to-date; with 0.120 eV at 1550 nm [29] and 0.15 eV at optical wavelengths [33]. TESs have also been shown to have very high detection efficiencies of up to 95% at near-infrared wavelengths [34].

TESs have been – and continue to be – considered as an ideal SPD for a vast range of applications: quantum information and quantum key distribution [35],

particle detection [36] and numerous astronomy applications and instruments [37, 38, 39].

Table 1.1: Comparison of proven energy-resolving SPDs. T_{op} - operating temperature, λs - EM regime, R - resolving power, λ_R - wavelength at which resolving power is measured.

	T_{op} (K)	λs	R	λ_R (nm)	Ref
SNSPD	6	NIR-UV	2	1000	[40]
TES	0.1	NIR-UV	2.76	1556	[34]
	0.1		15	480	[33]
STJ	0.4	vis-UV	5	200	[41]
KID	0.04	NIR-vis	3.6	1550	[42]
	0.1		10	400	[43]

1.4 Introduction to Kinetic Inductance Detectors

Kinetic inductance detectors (KIDs) are thin-film, superconducting microwave microresonators essentially comprising a simple resistor-inductor-capacitor (RLC) circuit with resonant frequency $\omega_0 = 1/\sqrt{LC}$. The superconducting film is made up of two populations of charge carriers: unpaired electrons (quasiparticles) and Cooper pairs. Cooper pairs are bound pairs of electrons and are the superconducting charge carriers. The inertia of Cooper pairs generates a kinetic inductance within the superconductor, which adds to the geometrical inductance of the circuit. The resonant frequency of a KID is therefore partially governed by its kinetic inductance. Excitations in the film lead to changes in the Cooper pair population, thereby changing the kinetic inductance.

Changes in the kinetic inductance will change the total internal inductance

which, in turn, alters the surface impedance of the device. The surface impedance of a micro-resonator dictates its resonant frequency f_0 and quality factor Q. Therefore any changes in the device's surface impedance will register as a change in both f_0 and Q. This can be seen in Figure 1.4, where incident photons alter the inductance of the resonator circuit. The result is a shift in resonant frequency δf_0 and a reduction in Q, which manifests as a broadening of the resonance dip.

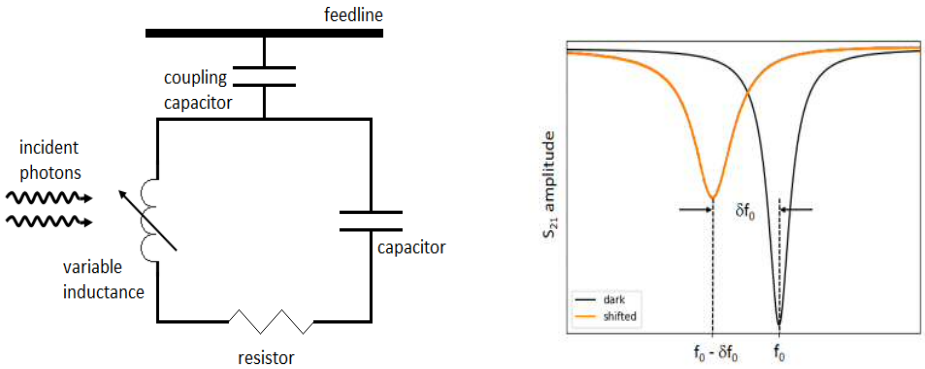

(a) (b)

Figure 1.4: a) Circuit schematic representation of a LEKID and b) response due to absorbed radiation.

Incident photons absorbed by a KID break Cooper pairs and the number of broken pairs is proportional to the photon energy. The resulting change in the Cooper pair population leads to a proportional response of the KID, such that $\delta f_0 \propto dN_{qp}$ where dN_{qp} is the change in quasiparticle population (equivalent to the change in Cooper pair population). This makes KIDs capable of resolving the energy of absorbed photons.

Due to the nature of a superconductor, only photons with energies $h\nu > 2\Delta$ can break Cooper pairs; where 2Δ is the binding energy of a Cooper pair. This sets a lower limit on detectable radiation. Δ is material-dependent thus the lower limit of detection can be tuned to some degree. At the time of writing, the dominant materials for KIDs are aluminium (Al) and titanium nitride (TiN). Al has a

typical superconductor energy gap of $\Delta \sim 90$ GHz which gives a lower limit of photons with wavelength $\lambda \sim 3$ mm. TiN is an interesting material as its Δ can be tuned according the amount of nitrogen content incorporated into the film during growth. An approximate upper limit of $\Delta \sim 160$ GHz [44] returns a lower limit of $\lambda \sim 1$ mm. There is no real upper limit to the photon energy that can be absorbed, making KIDs versatile photon detectors.

The response in KIDs is monitored by measuring the forward transmission S_{21} of a microwave probe (shown in Figure 1.4b) set to the resonant frequency, which passes along a feedline to which the resonator is coupled. Note that a KID's response can only be measured at frequencies close to f_0. Therefore it is possible to readout multiple KIDs from a single feedline by varying the resonant frequency of each resonator; as depicted in Figure 1.5.

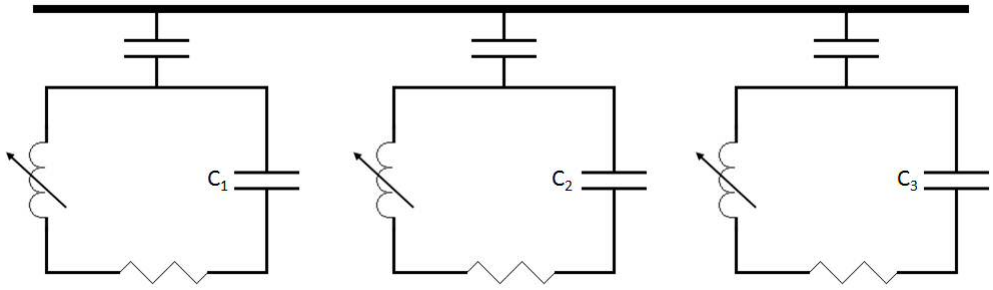

Figure 1.5: Circuit schematic representation of multiplexed KIDs along a single feedline. In this instance, the resonant frequencies of the resonators are tuned by the capacitance.

To date, there are two main types of KIDs: distributed KIDs and lumped element (LE) KIDs. The detector response will vary depending on the current density in the location of the pair-breaking event. Distributed KIDs require the use of antennas and feedlines to direct incident light to regions of high current density. Whereas with LEKIDs, the detecting element is part of the resonant structure which has uniform current density. Thus the response does not depend on the

location of the pair-breaking events. In reality, this is not quite true and will be explored later. The work detailed in this thesis is focussed on LEKIDs, therefore only LEKIDs are discussed further.

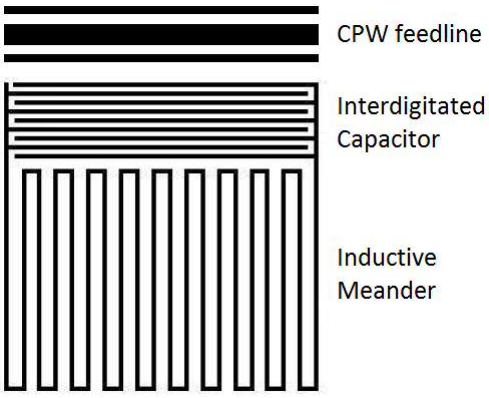

Figure 1.6: Schematic of the physical structure of a LEKID.

A standard LEKID is formed of a micro-resonator circuit – an inter-digitated capacitor (IDC) and inductive meander – coupled to a co-planar wave (CPW) transmission line; also referred to as the feedline. The detecting element of the resonator is the inductive meander. The physical structure is shown in Figure 1.6.

LEKIDs are a viable and competitive candidate as an energy-resolving SPD. The remainder of this work aims to further support established demonstrations of single-photon detection in KIDs and show the underlying physics which determine a LEKID's ultimate energy-resolution.

Chapter 2

Fundamental Physics of Kinetic Inductance Detectors

2.1 Superconductivity

Kinetic inductance detectors (KIDs) are pair-breaking detectors which rely on the phenomena of superconductivity. In this section, the foundations of superconductivity relevant to the operation of KIDs are described.

2.1.1 Microscopic Theory of Superconductivity

The foundation of current understanding of superconductivity is the description of the microscopic behaviour of a superconductor: Bardeen-Cooper-Schrieffer (BCS) theory. It postulates there exists an energy gap between the normal free electrons of a metal and the superconducting charge carriers [45]. It also postulates the phenomena of superconductivity are a result of these superconducting charge carriers; bound pairs of electrons known as "Cooper pairs" [46].

Electrons can be bound due to a weak attractive force known as the electron-phonon interaction: interactions between electrons and lattice vibrations. The presence of an electron can cause deformations in the surrounding lattice due to the electrostatic force between the negative electron and the positive ions. The lattice deformations lead to a local positive charge density which, in turn, attract other electrons. Hence, in effect, an attractive interaction can exist between two electrons. In the static case, an attracted electron will succumb to the repulsive Coulomb force as the original electron will become too close. The same holds for a slow moving electron. However, in the dynamic case where an electron has kinetic energy close to the Fermi energy, the picture is different. As the electron moves through the lattice, the lattice acquires the same local positive charge density as the electron attracts positive ions along its journey. However ions move slower than electrons so the region does not become locally positive instantaneously. By the time the local positive region forms, the electron has already passed through. In this way, there is a "trail" left by the passing electron as shown in Figure 2.1a. The local positively charged trail in the lattice allows a lower energy state for surrounding electrons to follow. And since the electron has already passed, the distance between the electrons is far enough to overcome the repulsive electrostatic force. If the second electron remains on the same path, it must have the same or exactly opposite wave vector $\mathbf{k}$ of the first electron. It has been shown that strength of the attractive interaction between electrons is at its maximum when the two electrons have opposite wave vectors and spin [47]. Cooper pair formation can also be viewed as the constant emission and absorption of "virtual" phonons; as seen in Figure 2.1b. Energy conservation is not violated as long as a phonon with energy $h\nu$ exists for a short time; due to the Heisenberg uncertainty principle. Therefore it must be absorbed quickly by another electron. The interaction between paired

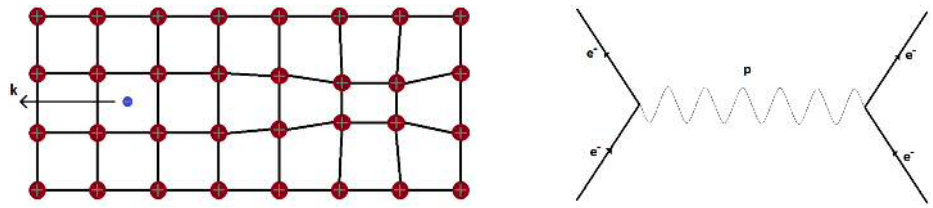

(a) (b)

Figure 2.1: a) Local deformation of the lattice as an election with energy $\sim E_F$ travels through lattice. b) Depiction of Cooper pair formation via virtual phonon $\mathbf{p}$ emission and absorption.

electrons through these virtual processes can be thought of as a continual scattering between the two electrons without their overall momentum changing.

The exchange of virtual phonons and the formation of Cooper pairs can only occur for electrons close to the Fermi level. All other electrons are bound by the Fermi-Dirac distribution whereby all other reachable states are already occupied, and thus cannot scatter. Note that since Cooper pairs are the pairing of two fermions of equal and opposite spin, Cooper pairs behave like bosons – with integer-spin – and follow Bose-Einstein statistics. Thus arises a condensation of Cooper pairs into a common ground state; also known as the superconducting ground state. This becomes the new ground state of the system and is associated with an energy gain.

Consider a normal metal at zero temperature. All energy levels up to E_F are filled and there are no occupied states above. This can be seen in Figure 2.2; note, Cooper pairs are not shown as they exist in a many-body state with a single total energy for all bound electrons. Whereas in the superconducting ground state of a superconductor, all electrons close the Fermi level are bound in Cooper pairs and have gained an additional average energy Δ per electron. This creates a gap of energy 2Δ around E_F due to electrons just below E_F having been removed to form Cooper pairs. So then above E_F, the lowest possible energy for a single electron is Δ; which agrees with Cooper pair binding energy 2Δ. This makes the minimum

excitation energy of an unpaired electron 2Δ so that when a Cooper pair is broken, two single electrons are produced in the lowest possible energy state just above the gap: $E_F + \Delta$.

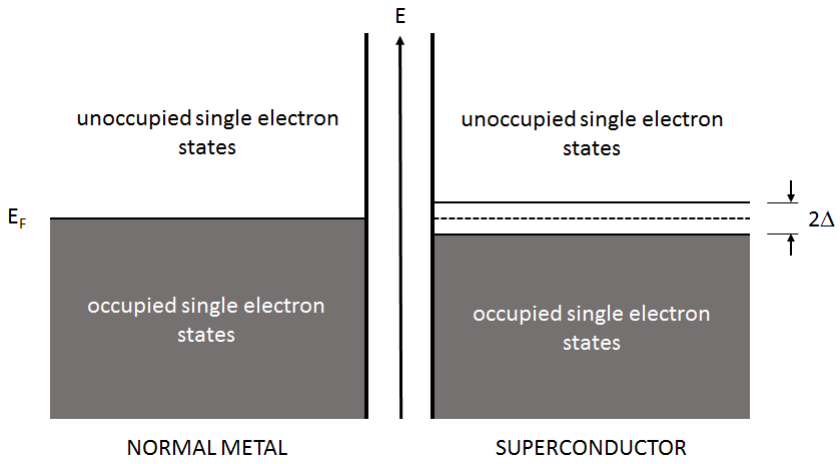

Figure 2.2: Occupation of single-electron states in a normal metal and superconductor at $T = 0K$.

Figure 2.2 depicts the single-electron states at zero temperature. Due to the co-operative nature of the Cooper pair condensate, the energy gained by a single electron, upon forming a Cooper pair and condensing into the common ground state, changes [48]. Note the Cooper pair condensate is a key element in the behaviour of superconductors. Thermal excitations will break pairs rather than raise the kinetic energy of a Cooper pair. Therefore, at finite temperatures, there exists a population of unpaired electrons. The 2Δ binding energy of a Cooper pair depends on the number of Cooper pairs already existing in the condensate and thus Δ becomes temperature-dependent. The temperature dependence of the gap energy is described by [49]

$$\frac{1}{N_0 V} = \int_{-\hbar\omega_D}^{\hbar\omega_D} \frac{tanh\{[\epsilon^2 + \Delta(T)^2]^{1/2}/2k_B T\}}{2[\epsilon^2 + \Delta(T)^2]^{1/2}} d\epsilon, \tag{2.1}$$

where $N_0 = N(\epsilon = 0)$ is the single-spin density of states at the Fermi surface, V

is the volume of the system, ω_D is the Debye frequency and ϵ is the relative energy of a Bloch state as measured in reference to the Fermi energy. By setting Δ to zero at the critical temperature T_c, the material-dependent value $1/N_0V$ can be found, such that

$$\frac{1}{N_0V} = \int_0^{\hbar\omega_D} \frac{tanh\{\epsilon/2k_BT\}}{\epsilon} d\epsilon. \tag{2.2}$$

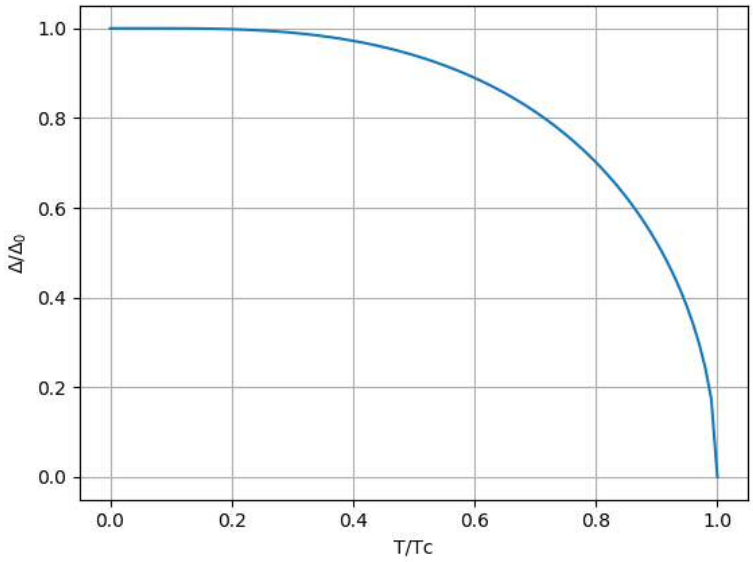

Figure 2.3: Temperature dependence of the energy gap of aluminium.

The temperature dependence of the energy gap of aluminium is shown in Figure 2.3. There is very little variation in the value for Δ at low temperatures $T < 0.4T_c$. A superconductor at $T = 0$ K should have no unpaired electrons. All available electrons will have formed Cooper pairs and exist in the condensed ground state; hence Δ is at its largest value $\Delta_0 = \Delta(T = 0) \cong (7/4)k_BT_c$ [49]. For $T > 0$ K, Cooper pairs are broken and unpaired electrons are able to exist in an excited state above $E_F + \Delta$. Therefore Δ reduces, falling to zero at T_c (above which there are only quasiparticles and the material is no longer in its superconducting state); as

shown in Figure 2.3. As such, any superconductor at finite temperature will have two sets of charge carriers.

2.1.2 Two-Fluid Model

The two-fluid model considers the two electronic paths of a superconductor, treating the two populations of charge carriers as different fluids [50, 51]. Figure 2.4 shows a simple circuit diagram representing a unit volume superconductor; with $\vec{J}_s$ as the current carried by Cooper pairs and $\vec{J}_n$ as the current carried by unpaired electrons. The unpaired electrons – also referred to as quasiparticles – exist as free fermionic particles. As such, they behave as they would in a normal metal; they scatter and exhibit loss. Therefore the quasiparticle current is represented by a resistive path in parallel with an inductive path. The superconducting current is represented by an inductive path with zero loss.

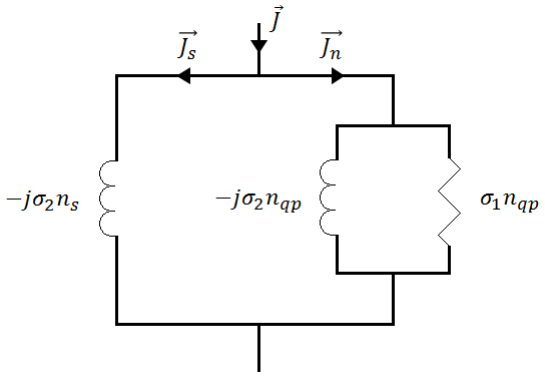

Figure 2.4: Circuit representation of the two-fluid model of a unit volume superconductor.

The effect of the two-fluid model can be better understood by applying the Drude model to the two electron populations. The conductivity of a normal metal

can be described by using the Drude model,

$$\sigma_n = \frac{n_n e^2 \tau}{m(1 + j\omega\tau)} = \frac{\sigma_0}{(1 + j\omega\tau)}, \tag{2.3}$$

where n_n is the number density of normal electrons, τ is the average scattering time and e and m are the charge and effective mass of the electron, respectively. By splitting the real and imaginary parts, (2.3) becomes

$$\sigma_n = \frac{n_n e^2 \tau}{m(1 + j\omega^2\tau^2)} - j\frac{n_n e^2 \omega\tau^2}{m(1 + j\omega^2\tau^2)}. \tag{2.4}$$

This can be re-written as

$$\sigma_n = \sigma_{1n} - j\sigma_{2n}. \tag{2.5}$$

The imaginary part arises from a current lag after a field is applied. For example, in an applied field the electrons will accelerate during time τ before scattering. If the field were reversed, the electrons must lose their momentum before accelerating in the opposite direction and thus arises a lag. At microwave frequencies, $\tau \gg \omega\tau^2$ making the imaginary term in (2.5) several orders of magnitude smaller than the real term. Hence σ_{2n} is small for scattering electrons and so is often ignored for normal metals. This is not the case for non-scattering electrons.

The superconducting charge carriers – Cooper pairs – do not scatter as they exist in the same energy state and hence do not exhibit loss. This phenomenon physically manifests as the zero DC resistance of a superconductor. Therefore the conductivity of the superconducting fluid can be found by setting $\tau = \infty$ in (2.4), such that

$$\sigma_s = -j\frac{n_s e^2}{m\omega}, \tag{2.6}$$

where n_s is the number density of superconducting electrons.

Applying the two-fluid model and Ohm's law, the total current density can be written as

$$\vec{J} = \vec{J_n} + \vec{J_s} = (\sigma_1 - j\sigma_2)\vec{E}, \tag{2.7}$$

where $\vec{E}$ is of the form $\vec{E} = \vec{E_0}e^{j\omega\tau}$. Then the conductivity of the superconductor takes a complex form where

$$\sigma_1 = \frac{n_n e^2 \tau}{m(1 + j\omega^2\tau^2)} \text{ and } \sigma_2 = \frac{n_s e^2}{m\omega} + \frac{n_n e^2 \omega\tau^2}{m(1 + j\omega^2\tau^2)}. \tag{2.8}$$

Now it is clear the real part of the conductivity involves only the normal fluid, while the imaginary part involves both the normal and superconducting fluids. Notice σ_2 is the sum of magnitude of σ_s from (2.6) (which can be denoted as σ_{2s}) and σ_{2n} from (2.5).

2.1.3 London Model

The two-fluid model provides a good overview of the electrodynamics of a superconductor but it does not describe its magnetic properties. The London model [52] applies electromagnetic equations to describe the zero DC resistance and complete diamagnetism (known as the Meissner effect) observed in bulk superconductors.

The London model assumes the observed phenomena of superconductors are due to a non-scattering, electron density n_s. The first London equation describes this by

$$\frac{d\vec{J}}{dt} = \frac{n_s e^2}{m}\vec{E}; \tag{2.9}$$

where $\vec{J}$ is the supercurrent density and $\vec{E} = \vec{E_0}e^{j\omega t}$ is the applied field in which the electrons will accelerate. In an AC circuit, the current density takes the form

$\vec{J} = \vec{J}_0 e^{j\omega t}$. Applying this to (2.9) gives

$$\vec{J} = -j\frac{n_s e^2}{\omega m}\vec{E}. \tag{2.10}$$

Using Ohm's law, the conductivity of the non-scattering electron density can be given by

$$\sigma_s = -j\frac{n_s e^2}{\omega m}. \tag{2.11}$$

Notice (2.11) takes the same form as (2.6); describing the zero DC resistance of a superconductor.

The second London equation can be given by [53]

$$\vec{B} = B_0 \exp\left(\frac{-\vec{x}}{\sqrt{m/\mu_0 n_s e^2}}\right), \tag{2.12}$$

where B_0 is the magnitude of magnetic flux at the surface and $\vec{x}$ is the distance from the surface. The distance at which the magnetic field falls to e^{-1} of the value at the surface is known as the London penetration depth, such that

$$\lambda_L = \sqrt{\frac{m}{\mu_0 n_s e^2}}. \tag{2.13}$$

(2.12) describes the exponential decay of the magnetic field within a superconductor and is an important result for thin-film superconductors which tend to have thickness $t < \lambda_L$. Using, (2.8), the penetration depth can be re-written in terms of the superconducting conductivity, such that

$$\lambda_L = \sqrt{\frac{1}{\mu_0 \omega \sigma_{2s}}}. \tag{2.14}$$

2.1.4 Mattis-Bardeen Conductivity

Another shortcoming of the two-fluid model is that it assumes the superconducting fluid is made up of superconducting electrons rather than bound pairs of electrons and does not take into account the finite size of a Cooper pair. The two-fluid model also does not take into account the band gap of the superconductor. Mattis and Bardeen provide an analytical model to describe the complex conductivity which satisfies BCS theory [54]:

$$\begin{aligned}\frac{\sigma_1}{\sigma_n} =& \frac{2}{\hbar\omega}\int_{\Delta}^{\infty}[f(E)-f(E+\hbar\omega)]g(E)dE \\ &+\frac{1}{\hbar\omega}\int_{\Delta-\hbar\omega}^{-\Delta}[1-f(E+\hbar\omega)]g(E)dE\end{aligned} \tag{2.15}$$

and

$$\frac{\sigma_2}{\sigma_n} = \frac{1}{\hbar\omega}\int_{\Delta-\hbar\omega,-\Delta}^{\Delta}\frac{[1-2f(E+\hbar\omega)][E^2+\Delta^2+\hbar\omega E]}{\sqrt{\Delta^2-E^2}\sqrt{(E+\hbar\omega)^2-\Delta^2}}dE, \tag{2.16}$$

where f is the Fermi-Dirac distribution function

$$f(\eta) = \frac{1}{1+e^{\eta/k_BT}}, \tag{2.17}$$

and $g(E)$ is given by

$$g(E) = \frac{E^2+\Delta^2+\hbar\omega E}{\sqrt{\Delta^2-E^2}\sqrt{(E+\hbar\omega)^2-\Delta^2}}. \tag{2.18}$$

(2.15) and (2.16) are known as the Mattis-Bardeen integrals. Note that the first integral of (2.15) represents the effect of thermally excited quasiparticles while the second integral represents the effects of photon-excited quasiparticles. Therefore the second integral of σ_1 is zero for $\hbar\omega < 2\Delta$.

In the limits $k_BT, \hbar\omega \ll \Delta_0$, the Mattis-Bardeen integrals can be approximated by [53, 55]

$$\frac{\sigma_1}{\sigma_n} \approx \frac{4\Delta(T)}{\hbar\omega}\exp\left(\frac{-\Delta_0}{k_BT}\right) K_0(\zeta)\sinh(\zeta), \tag{2.19}$$

$$\frac{\sigma_2}{\sigma_n} \approx \frac{\pi\Delta(T)}{\hbar\omega}[1 - 2\exp\left(\frac{-\Delta_0}{k_BT}\right)\exp(-\zeta)I_0(\zeta)]. \tag{2.20}$$

where $\zeta = \hbar\omega/2k_BT$ and I_0 and K_0 are modified Bessel functions of the first and second kind, respectively. For the measurements of Al LEKIDs, at typical operating temperatures of $\sim$ 100 mK and at frequencies $\sim$ 3 GHz, these approximations remain valid.

2.1.5 Internal Inductance of a Superconductor Strip

The internal inductance of a superconductor is made up of a kinetic inductance L_k and a magnetic inductance L_m. The kinetic inductance arises from the kinetic energy of the superconducting fluid (Cooper pairs). The magnetic inductance is due to the magnetic field energy density of the superconductor. The field energy is generated by the supercurrent $\vec{J_s} = -n_s e\vec{v_s}$ where $\vec{v_s}$ is the velocity of the superconducting electrons.

The kinetic inductance per unit volume can be calculated by calculating the kinetic energy of the electrons contributing to the supercurrent. This can be given by

$$KE = \frac{1}{2}n_s m {v_s}^2 = \frac{1}{2}\frac{m}{n_s e^2}{J_s}^2 = \frac{1}{2}\mu_0{\lambda_L}^2{J_s}^2; \tag{2.21}$$

using (2.13).

The kinetic inductance is then given by

$$U_k = \frac{1}{2}L_k I^2 = \frac{1}{2}\mu_0 {\lambda_L}^2 \oint {\vec{J}_s}^2 d\vec{s}, \tag{2.22}$$

where U_k is the kinetic energy per unit length and I is the total current. Note the current density in a superconductor is restricted to a depth λ_L; the cross-sectional area of a superconductor strip, for two film thicknesses is illustrated in Figure 2.5.

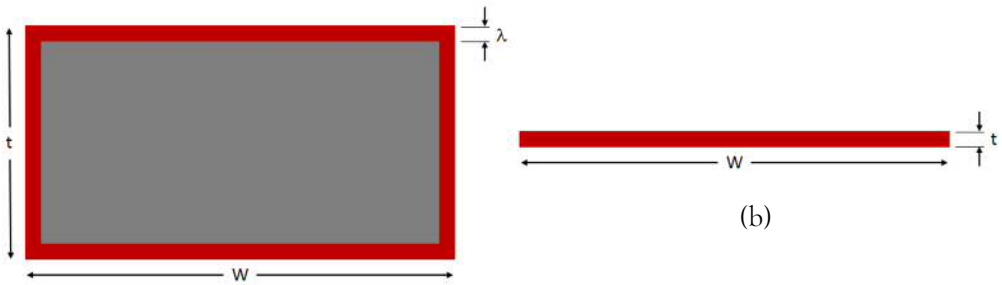

Figure 2.5: Representation of current density (red area) within a) a thick superconducting film and b) a thin superconducting film.

For the case where $W \gg t \gg \lambda_L$, the effective cross-sectional area is $2W\lambda_L$; neglecting the comparatively small current density $2t\lambda_L$ at the edges. This gives $J_s = I/2W\lambda_L$ so that the kinetic inductance is given by

$$\frac{1}{2}L_k I^2 = \frac{\mu_0 {\lambda_L}^2 I^2}{8W^2 {\lambda_L}^2} 2W\lambda_L \rightarrow L_k = \frac{\mu_0 \lambda_L}{2W}. \tag{2.23}$$

For the case where $W \gg \lambda_L \gg t$, the effective cross-sectional area becomes Wt. Thus the kinetic inductance can be given by

$$\frac{1}{2}L_k I^2 = \frac{\mu_0 {\lambda_L}^2 I^2}{2W^2 t^2} Wt \rightarrow L_k = \frac{\mu_0 {\lambda_L}^2}{Wt}. \tag{2.24}$$

In reality, KIDs are fabricated with film thickness in between the two cases

above. Thus (2.22) must be performed across the entire cross-sectional area of the film. Variations in current density must also be taken into account. A full treatment of the derivation can be found in [53], resulting in

$$L_k = \frac{\mu_0 \lambda_L}{4W}\left[\coth\left(\frac{t}{2\lambda_L}\right) + \left(\frac{t}{2\lambda_L}\right)\mathrm{cosec}^2\left(\frac{t}{2\lambda_L}\right)\right] \tag{2.25}$$

and

$$L_m = \frac{\mu_0 \lambda_L}{4W}\left[\coth\left(\frac{t}{2\lambda_L}\right) - \left(\frac{t}{2\lambda_L}\right)\mathrm{cosec}^2\left(\frac{t}{2\lambda_L}\right)\right]. \tag{2.26}$$

Note (2.25) and (2.26) are in units if H/unit length, so summing these and multiplying by the superconductor strip width will give the total internal inductance in units of H/square:

$$L_{int} = L_k + L_m = \frac{\mu_0 \lambda_L}{2}\coth\left(\frac{t}{2\lambda_L}\right). \tag{2.27}$$

2.1.6 Surface Impedance of a Superconductor Strip

The surface impedance of a superconducting strip takes the form

$$Z_s = R_s + jX_s, \tag{2.28}$$

where R_s is the surface resistance and $X_s = \omega L_{int}$ is the surface reactance. Following the example in [53], the surface resistance of a superconductor strip can be found from

$$RI^2 = Re\left\{\oint \frac{\vec{J}^2}{\sigma_1 - j\sigma_2} d\vec{s}\right\} = \frac{\sigma_1}{{\sigma_1}^2 + {\sigma_2}^2}\oint \vec{J}^2 d\vec{s}. \tag{2.29}$$

The surface integral can be given in terms of the kinetic inductance from (2.22), such that

$$R = \frac{\sigma_1}{{\sigma_1}^2 + {\sigma_2}^2} \frac{L_k}{\mu_0 {\lambda_L}^2}. \tag{2.30}$$

Using (2.14), this can be further simplfied to

$$R = \omega L_k \frac{\sigma_1 \sigma_2}{{\sigma_1}^2 + {\sigma_2}^2}. \tag{2.31}$$

A full expression for the surface impedance of a superconductor strip can then be given by

$$Z_s = \omega L_k \frac{\sigma_1 \sigma_2}{{\sigma_1}^2 + {\sigma_2}^2} + j\sqrt{\frac{\mu_0 \omega}{4\sigma_2}} \coth\left(\frac{t\sqrt{\mu_0 \omega \sigma_2}}{2}\right). \tag{2.32}$$

2.2 Quasiparticle Dynamics

2.2.1 Thermal Excitations

Given that the total number density n of the system is fixed, at $T = 0$ K, $n \simeq n_s$ such that all available electrons are paired up in Cooper pairs. At finite temperatures, lattice vibrations (i.e. phonons) break Cooper pairs to create thermal quasiparticles. The quasiparticle population tends to continuously fluctuate about some mean value. The statistical mean number density of quasiparticles is given by [56]

$$n_{qp} = 4N_0 \int_0^\infty N_s(E) f(E) dE \approx 2N_0 \sqrt{2\pi k_B T \Delta} e^{-\Delta/k_B T}, \tag{2.33}$$

where $N_s(E) = Re\{E/\sqrt{E^2 + \Delta^2}\}$ is the normalised quasiparticle density of states. Note the approximation is only valid for a thermal quasiparticle distribution and for $k_B T \ll \Delta$. The number of quasiparticles in the system is then given by

$N_{qp} = n_{qp}V$ where V is the volume.

When Cooper pairs are broken in the superconductor's steady state, the quasiparticles will re-combine back into the superconducting ground state as Cooper pairs. This occurs over an average timescale τ_{qp}: the quasiparticle lifetime. The quasiparticle lifetime can be given by [57]

$$\frac{1}{\tau_{qp}} = \frac{\tau_0}{\sqrt{\pi}} \left(\frac{k_B T_c}{2\Delta} \right)^{5/2} \sqrt{\frac{T_c}{T}} e^{\Delta / k_B T}, \tag{2.34}$$

where τ_0 is the electron-phonon interaction time and is a material-dependent quantity. Using (2.33) the quasiparticle lifetime can be written in terms of the quasiparticle density, such that

$$\tau_{qp} = \frac{\tau_0}{n_{qp}} \frac{N_0 (k_B T_c)^3}{2\Delta^2}. \tag{2.35}$$

2.2.2 Photon Absorption

There are two mechanisms by which a photon, with energy $h\nu$, can be absorbed in a superconductor. The first is by a transition of a quasiparticle with energy E to an excited state $E + h\nu$. At low temperatures $T \ll T_c$, the likelihood of this is very low as it depends on the number of available quasiparticles and the number of available energy states. The other, more likely, mechanism is where an absorbed photon breaks a Cooper pair. However, the photon must have an energy $h\nu \geq 2\Delta$.

It is expected, a photon with energy $h\nu \gg 2\Delta$ will break an initial Cooper pair generating two high energy quasiparticles that can then go on to break further Cooper pairs. A quasiparticle cascade can ensue in quick succession until the ultimate quasiparticles generated have insufficient energy to break a Cooper pair. At this point, a quasiparticle is likely to re-combine to the energetically favourable su-

perconducting ground state. During the quasiparticle cascade, the generated quasiparticles relax and re-combine over the same average steady-state timescale τ_{qp}.

Consider a superconductor under load by a continuous flux with photons of energy $E > 2\Delta$. The new loaded equilibrium number of quasiparticles can be estimated by

$$N_{xs} = \frac{\eta P \tau_{qp}}{\Delta}, \tag{2.36}$$

where η is the quasiparticle creation efficiency factor and has historically been taken to be $\eta = 0.57$ [58]. Here, P is the optical power so that P/Δ gives the number of potential pair-breaking events per second. Following this example, it can be expected a single photon will generate (on average)

$$N_{gen} = \frac{\eta h\nu}{\Delta}, \tag{2.37}$$

over the quasiparticle lifetime. Note that it is assumed the detector is in a linear regime, in that the quasiparticle lifetime does not change significantly upon a change in the equilibrium quasiparticle population.

2.3 Resonator Theory

LEKIDs operate on the basis that absorbed photons will alter the superconducting properties of the device: a superconducting microwave resonator. Section 2.1 has shown that changes in the conductivity and kinetic inductance will change the surface impedance of the superconductor. Here, the microwave perspective is considered to show how the impedance of a resonator effects the resonator properties.

LEKIDs are formed of a series RLC microwave resonator where the inductor and capacitor are formed of discrete components. The resistance accounts for the

quasiparticles in the inductive meander (see Figure 1.6). Figure 2.6 shows the equivalent circuit diagram of a LEKID coupled to a feedline.

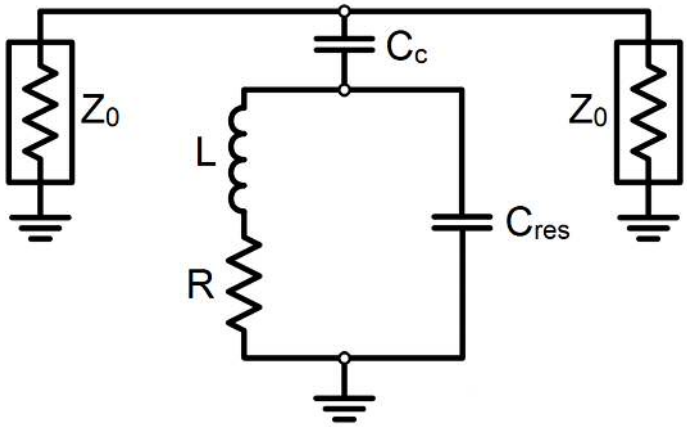

Figure 2.6: Circuit diagram of a series RLC resonator capacitively-coupled to a feedline.

The average energy stored in the inductor W_m and capacitor W_e are given by [59]

$$W_m = \frac{1}{4}|I|^2 L \text{ and } W_e = \frac{1}{4}|V_C|^2 C_{res} = \frac{1}{4}|I|^2 \frac{1}{\omega^2 C_{res}}, \tag{2.38}$$

where L is the inductance, I is the current, C_{res} is the capacitance of the resonator and V_C is the voltage across the capacitor. At resonance, the stored energies are equal such that $W_m = W_e$, therefore the resonant frequency is defined as [59]

$$\omega_0 = \frac{1}{\sqrt{LC_{res}}}. \tag{2.39}$$

2.3.1 Quality Factor

The performance of microwave resonators can be described by their quality factor Q; whereby low-Q resonators indicate a high rate of energy loss while a higher Q indicates a smaller energy loss rate. The Q-factor is defined as the average energy

stored divided by the average energy lost per cycle. It is given by [59]

$$Q = \omega \times \frac{\text{average energy stored}}{\text{average energy loss rate}} = \frac{\omega_0 E_S}{P_{diss}}. \tag{2.40}$$

On resonance, the energy stored in the capacitor is equal to that stored in the inductor. Therefore, the total stored energy in the resonator can be given by $E_S = 2W_m = 2W_e$ from (2.38). Using (2.40) with $P_{diss} = |I|^2 R/2 = |V|^2/2R$ gives

$$Q_i = \frac{\omega_0 L}{R} = \omega_0 C_{res} R. \tag{2.41}$$

(2.41) describes the intrinsic (or unloaded) Q-factor of a LEKID which is defined by the properties of the resonator circuit components. Figure 2.6 shows a LEKID that is capacitively-coupled to a feedline. This coupling has an associated coupling Q-factor Q_c. Any current leaking out of the resonator circuit is limited by the coupling capacitance C_C so that

$$P_{diss} = \frac{1}{2}|I_{loss}|^2 R = \frac{1}{4}|V_C|^2 {\omega_0}^2 Z_0, \tag{2.42}$$

where $I_{loss} = |V_C|/Z_{Cc}$ with $Z_{Cc} = 1/j\omega C_C$ and $R = Z_0/2$ due to the two ports of the feedline shown in Figure 2.6. Following the same argument as for the derivation of Q_i : $E_S = 2W_e$ from (2.38) gives

$$Q_c = \frac{2C_{res}}{\omega_0 {C_C}^2 Z_0}. \tag{2.43}$$

The overall Q-factor of a coupled device (also referred to as the loaded Q) is then a combination of Q_i and Q_c, such that

$$\frac{1}{Q_{tot}} = \frac{1}{Q_i} + \frac{1}{Q_c}. \tag{2.44}$$

2.3.2 Impedance

Assuming the inductor and capacitor are pure and lossless, with the resistance R forming the only loss in the circuit, the impedance due to the capacitive path Z_C and inductive path Z_L can be written as

$$Z_C = \frac{1}{j\omega C_{res}} \text{ and } Z_L = j\omega L + R, \tag{2.45}$$

where ω is the probing frequency. Then the total impedance of the resonator Z_{res} is given by

$$\frac{1}{Z_{res}} = j\omega C_{res} + \frac{1}{j\omega L + R} = j\omega C_{res} + \frac{R - j\omega L}{R^2 + \omega^2 L^2}. \tag{2.46}$$

At microwave frequencies, $\omega^2 L^2 \gg R^2$ so that (2.46) can be simplified to

$$\frac{1}{Z_{res}} = j\omega C_{res} + \frac{R}{\omega^2 L^2} + \frac{1}{j\omega L}. \tag{2.47}$$

In the process of measuring a LEKID, the resonator is probed near the resonant frequency such that $\omega = \omega_0 + \Delta\omega$, where $\Delta\omega \ll \omega_0$. To evaluate (2.47), the Taylor expansion $1/(1+x) \simeq 1 - x$ if $x \ll 1$ is used; with $x = \Delta\omega/\omega_0$, such that

$$\frac{1}{Z_{res}} = j\Delta\omega C_{res} + \frac{R}{(\omega_0 + \Delta\omega)^2 L^2}. \tag{2.48}$$

Making use of (2.39) and since $\Delta\omega \ll \omega_0$, (2.48) can be simplified further so that the resonator impedance can be given by

$$Z_{res} = \frac{{\omega_0}^2 L^2}{2j\Delta\omega L + R}. \tag{2.49}$$

The impedance of the coupled resonator must take into account the coupling capacitor which is in series with the resonator circuit: $Z_{in} = Z_{Cc} + Z_{res}$. Therefore,

$$Z_{in} = \frac{{\omega_0}^2 L^2}{2j\Delta\omega L + R} - \frac{-j}{\omega C_C}. \tag{2.50}$$

2.3.3 Transmission

As previously mentioned, the response in LEKIDs is monitored by measuring the forward transmission S_{21}. S_{21} is the ratio of voltage measured on the output port, to the voltage applied to the input port of the microwave network. It is be given by [59]

$$S_{21}(\omega) = \frac{2}{2 + Z_0/Z_{in}}, \tag{2.51}$$

where Z_0 is the impedance of the feedline and is nominally set to 50Ω. The analytical expression for Z_0/Z_{in} of the series RLC circuit contains many terms that cannot be simplfied. However, the result from the equivalent parallel RLC circuit with an equivalent resistance $1/R$ provides the analytical solution that describes the series case [60]

$$S_{21}(\omega) = \frac{Q_{tot}/Q_i + 2Q_{tot}x_{res}}{1 + 2Q_{tot}x_{res}} = 1 - \frac{Q_{tot}}{Q_c}\frac{1}{1 + 2jQ_{tot}x_{res}}; \tag{2.52}$$

where Q_{tot}, Q_i and Q_c are the same as those defined in Section 2.3.1 and $x_{res} = (\omega - \omega_{res})/\omega_{res}$ is the fractional frequency shift of the resonator. Note ω_{res} is the resonant frequency of the coupled resonator (i.e. taking into account the coupling to the feedline).

Chapter 3

Optical Response in LEKIDs

Drawing upon the theory described in the previous chapter, a baseline responsivity model has been developed which demonstrates the measureable effect of single-photon absorption. In this chapter, the theory is brought together to show the typical response of LEKIDs and the limiting factors on a LEKIDs responsivity and sensitivity; in the context of single-photon detection.

3.1 Principle of Detection

The LEKID response to photon absorption can be understood by considering the effect a single quasiparticle has on the superconducting resonator. The responsivity of a LEKID takes the basic form

$$R = \frac{df_0}{dN_{qp}}, \tag{3.1}$$

where df_0 is the change in resonant frequency and dN_{qp} is the change in quasiparticle population. (3.1) can be expanded by using the well-established model

outlined in [53], such that

$$\frac{df_0}{dN_{qp}} = \frac{df_0}{dL_{tot}}\frac{dL_{tot}}{d\sigma_2}\frac{d\sigma_2}{dT}\frac{dT}{dN_{qp}}. \tag{3.2}$$

Here it is important to note the response to pair-breaking due to thermal excitations has been found to be equivalent to that under optical illumination [61]. Therefore (3.2) can apply for both the response due to thermal excitations and photon absorption. Each term is given by the following equations; for brevity $\mu_0\omega_0\sigma_2 = \gamma$ and $\hbar\omega/2k_BT = \zeta$:

$$\frac{df_0}{dL_{tot}} = -\frac{f_0}{2L_{tot}} \tag{3.3}$$

$$\frac{dL_{tot}}{d\sigma_2} = \frac{-\mu_0\sqrt{2}}{8}\left[\frac{2\sqrt{\gamma}\coth\left(\frac{t\sqrt{\gamma}}{2}\right) - \gamma t + \gamma\coth^2\left(\frac{t\sqrt{\gamma}}{2}\right)}{\sqrt{\mu_0\omega\sigma_2}\sqrt{\gamma}}\right] \tag{3.4}$$

$$\frac{d\sigma_2}{dT} = \frac{-\pi\sigma_n\Delta(T)}{\hbar\omega k_BT^2}\exp\left(-\frac{2\Delta_0+\hbar\omega}{2k_BT}\right)\left[2\Delta_0 I_0(\zeta) + \hbar\omega_0 I_0(\zeta) - \hbar\omega_0 I_1(\zeta)\right] \tag{3.5}$$

$$\frac{dT}{dN_{qp}} = \left[\frac{N_0\Delta_0\sqrt{2\pi}}{T}\frac{k_BT + 2\Delta_0}{\sqrt{k_BT\Delta_0}}\exp\left(\frac{-\Delta_0}{k_BT}\right)V\right]^{-1}; \tag{3.6}$$

where t is the film thickness, I_0 and I_1 are the modified Bessel functions of the first and second kind, respectively, and V is the volume of the inductive meander [53]. Many of the variables in the above equations are material dependent. As this work focusses on aluminium, the primary variables that can be modified to improve responsivity are the geometric parameters: thickness and volume. From (3.4), it can be seen thinner films will increase the term $dL_{tot}/d\sigma_2$ since $\coth(x), \coth^2(x) \to \infty$ as $x \to 0$. Likewise, in (3.6) a smaller volume will increase the term dT/dN_{qp}.

This model is based on the fundamental equations described in the previous chapter and thus assumes the device is in its steady state.

3.2 Noise

3.2.1 Detector Bandwidth

The response of a LEKID is limited by its bandwidth, which is set by the fundamental time-constants: the quasiparticle lifetime and the resonator ring-down time. The resonator ring-down time is the characteristic time it takes for the resonator to relax back to its unperturbed state; it is given by [53]

$$\tau_{res} = \frac{Q_{tot}}{\pi f_0}. \tag{3.7}$$

For aluminium, the typical quasiparticle lifetime is temperature-dependent and of order $10^2 - 10^3 \mu$s. A typical LEKID is designed to have $Q_{tot} \sim 10^5$ and $f_0 \sim 3$ GHz, which gives $\tau_{res} \sim 10\mu$s. In general, LEKIDs are designed to ensure $\tau_{qp} > \tau_{res}$ to ensure the detector time-constant is dictated by material parameters.

3.2.2 Generation-Recombination Noise

The sensitivity of a LEKID is fundamentally limited by generation-recombination (GR) noise. As hinted when describing the equilibrium state of a superconductor, the quasiparticle density is taken as an average. At finite temperatures, random fluctuations in the quasiparticle population occur continuously: thermal excitations cause pair-breaking events as quasiparticles relax down to re-combine. These small changes in the quasiparticle density lead to small changes in the superconductor properties and thus generates responses in the device.

The associated noise equivalent power (NEP) due to GR noise is given by [62]

$$NEP_{GR} = 2\Delta\sqrt{\frac{N_{qp}}{\tau_{qp}}}, \tag{3.8}$$

where N_{qp} is the quasiparticle population. NEP is defined as the pair-breaking power required to produce a signal-to-noise ratio (SNR) of unity in a 1 Hz bandwidth (or 0.5 s integration time).

Both Δ and τ_{qp} are material-dependent but N_{qp} depends on temperature and device volume. Therefore GR noise contributions can be decreased by using small volume devices, operated at low temperatures. Theory dictates $N_{qp}, NEP_{GR} \to 0$ as $T \to 0$ however there is some non-zero saturation level at very low temperatures [63]. This can be seen in Figure 3.1, where the quasiparticle population (and hence NEP_{GR}) diverge from theory at approximately 170 mK. It is thought the saturation temperature is material and fabrication dependent. Thus, this saturation temperature may be the limiting factor of a LEKID's sensitivity.

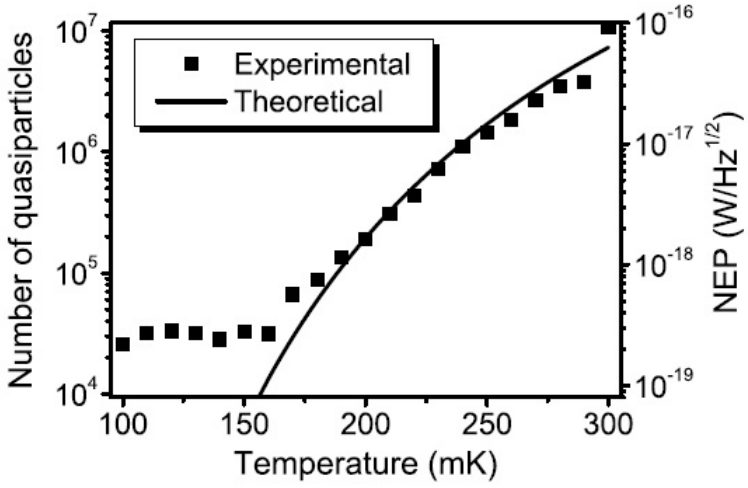

Figure 3.1: The measured number of quasiparticles and corresponding NEP due to GR noise as a function of temperature [63].

3.2.3 Amplifier Noise

Amplifier noise is intrinsic to the electronic readout set-up. It is given by Johnson noise, such that

$$\sigma_{amp} = \sqrt{4k_B T_{amp} R_{feed}}, \tag{3.9}$$

where T_{amp} is the amplifier temperature and R_{feed} is the impedance of the feedline which is nominally set to 50Ω. Although unavoidable, this is typically minimised by using a cryogenic low noise amplifier at temperatures $T_{amp} \leq 6$ K. Amplifier noise is characteristically flat and treated as background noise.

3.3 Modelling Single-Photon Detection

3.3.1 A Single Absorption Event

From (3.2) it can be seen that LEKID responsivity is dependent on temperature. Therefore, it is possible to model photon absorption based on the thermal response of the device df_0/dT. An example of a simulated device is shown in Figure 3.2. The S_{21} amplitude is plotted, with f_0 being the frequency at which the S_{21} amplitude is a minimum.

For single-photon detection, the response due to a single quasiparticle is required. Following (3.2), $df_0/dN_{qp} = df_0/dT \times dT/dN_{qp}$. The result is shown in Figure 3.3. There is a linear relationship between f_0 and N_{qp}, thus a linear fit can be useed to extract df_0/dN_{qp}.

For some single-photon of known energy $h\nu$, the number of quasiparticles generated in the detector volume can be estimated using: $N_{gen} = \eta h\nu/\Delta$. Here, it is assumed the increased number of quasiparticles are distributed uniformly across the detector. As a first order estimate, the maximum frequency shift of the detector

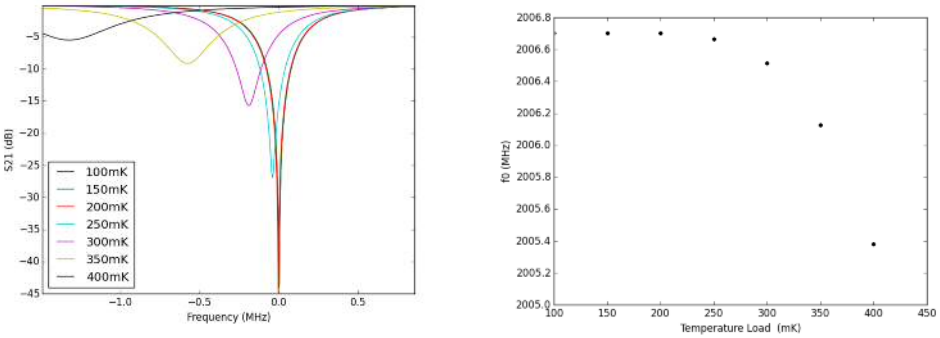

(a) (b)

Figure 3.2: a) S_{21} response normalised about the resonant frequency as measured at base temperature (100 mK): $f_0 = 2$ GHz. S_{21} is plotted for a range of different bath temperatures. b) Plot of resonant frequency as a function of bath temperature.

can be given by

$$df_{max} = N_{gen}\frac{df_0}{dN_{qp}}. \tag{3.10}$$

The expected response to single-photon absorption is a pulse with an exponential decay of the resonance frequency shift df_0. The decay time is governed by the dominant time-constant of the detector. This is assumed to be the quasiparticle lifetime τ_{qp}, such that

$$df_0(t) = df_{max}e^{-t/\tau_{qp}}. \tag{3.11}$$

For our testing, LEKIDs are measured using a single pixel homodyne detection scheme, which enables real-time tracking of the detector response. In any instrument a mutliplex (MUX) readout (also using homodyne detection) would be used to measure an array i.e. reading all resonators - or as many pixels which lie within the given bandwidth - simultaneously. Note homodyne detection will be described in more detail in the following chapter. The measurement outputs are time-streams $I(t)$ and $Q(t)$; where I and Q are the real and imaginary parts of S_{21}, respectively. For small shifts in f_0 these raw time-streams can be converted to obtain $df_0(t)$

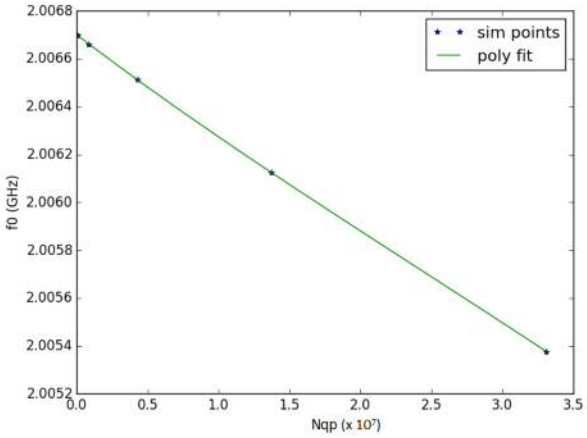

Figure 3.3: Plot of resonant frequency as a function of quasiparticle population. A linear polynomial (green) is fitted to the simulated data points to estimate df_0/dN_{qp}.

which is calculated using [64]:

$$df_0(t) = \frac{I(t)\frac{dI}{df} + Q(t)\frac{dQ}{df}}{\left(\frac{dI}{df}\right)^2 + \left(\frac{dQ}{df}\right)^2}, \tag{3.12}$$

where dI/df and dQ/df are the maximum response of the detector in I and Q, respectively. These are also described in more detail in the following chapter. Note (3.12) is sensitive to the sign of I and Q. As shown in Figure 3.2, the resonant frequency of a LEKID will decrease with an increase in temperature (i.e. increase in equilibrium quasiparticles). This will translate as a negative response in dI/df and dQ/df. However, for the purpose of the making $df_0(t)$ intuitively readable, the sign is ignored and the magnitude is taken in this work.

The detector output can be simulated with artificial white noise based on the fundamental noise of the detector and the limits of the data acquisition (DAQ) unit. The magnitude of the GR noise spectrum is given by $4N_{qp}\tau_{qp}$. This is multiplied by the DAQ bandwidth and the device responsivity as the signal input in a Gaussian noise generator. A typical measurement is taken in a 1 second interval,

at a sampling rate of 200 kHz. Figure 3.4 shows an example simulation of an Al LEKID response to a 700 nm photon absorption event. Recalling Figure 3.1, the LEKID is simulated at a saturation temperature of $\sim$ 170 mK. The LEKID has $df_{max} \sim 130$ Hz and $\tau_{qp} \sim 2$ ms following theory for a 25 nm Al film. The volume of the simulated LEKID is $V \sim 1100\mu\text{m}^3$.

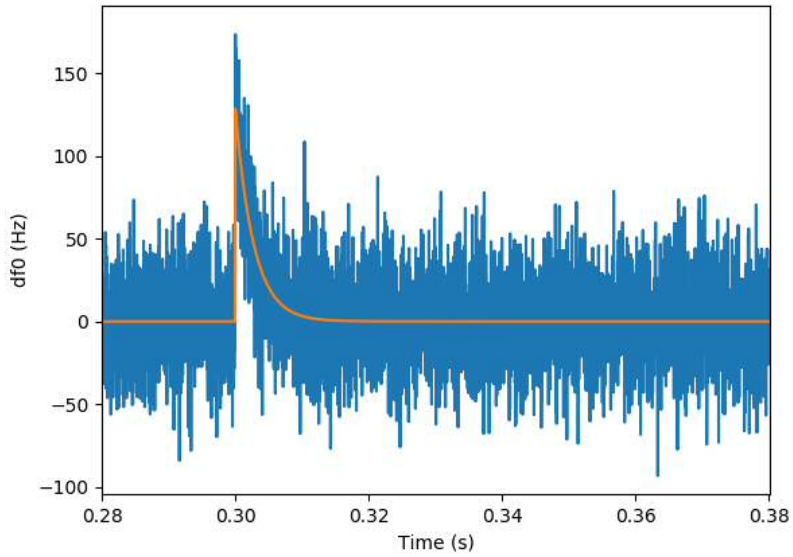

Figure 3.4: Snapshot of a 1 second time-stream of LEKID response to a single-photon ($\lambda = 700$ nm) absorption event at $t = 300$ ms, at a sample rate of 200 kHz. The orange line shows the expected noiseless signal.

3.3.2 Multiple Random Absorption

In reality, there are likely to be multiple single-photon absorption events, including many-photon absorption events, due to the random nature of light. This can also be simulated using the same methods detailed above, by injecting multiple photons with random arrival times. An example of this is shown in Figure 3.5, for the same detector and data acquisition (DAQ) sampling rate.

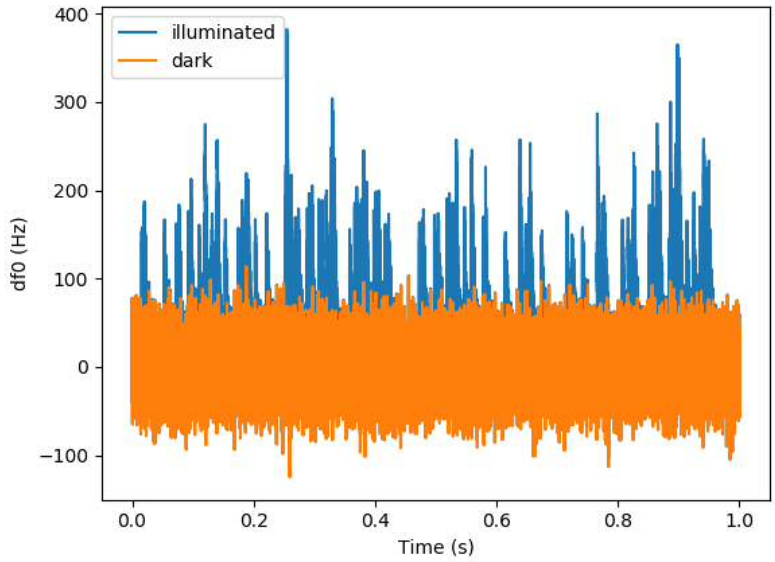

Figure 3.5: Example 1-second timestream with no incident photons (orange) and multiple random absorption events (blue); with 100 photons of $\lambda = 700$ nm.

Figure 3.5 shows a stark variation in the peak heights for the simulated absorption events. This will be due to the fluctuation in noise but also due to overlapping (or double and triple) absorption events and the DAQ sampling rate. The result of overlapping events can be seen in Figure 3.6, where there appears to be a single absorption event followed immediately by another single event.

Figure 3.7 shows the difference between the theoretical df_{max} and the simulated peak height of an absorption event; for each event simulated for Figure 3.6. There is an average difference of 7.5 Hz. This difference arises from the random timing of the DAQ. The DAQ is unlikely to sample at the exact time an absorption event registers a response. This is a limiting artefact of the equipment used. The difference is inversely proportional to the sampling rate. So an increase in sampling rate should reduce this variation.

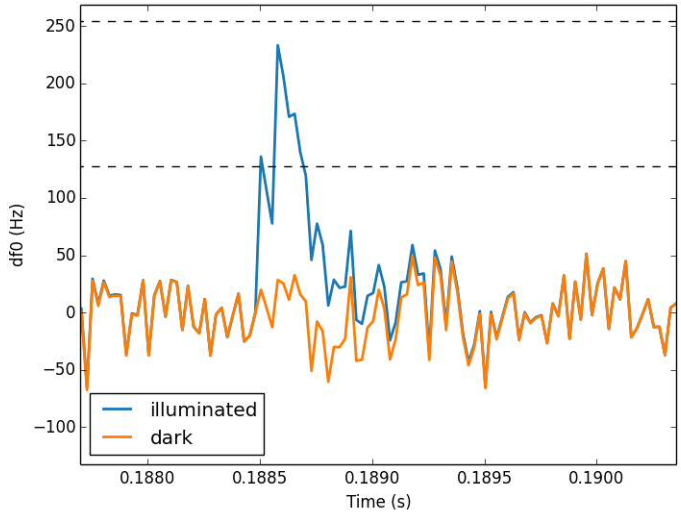

Figure 3.6: Example of overlapping absorption events. The black dashed line indicates quanta of df_{max}. Note the quasiparticle lifetime was reduced to 200 μs to increase the chance of overlapping events - within the simulation - without saturating the response. 250 absorptions events were simulated within a 1-second timestream.

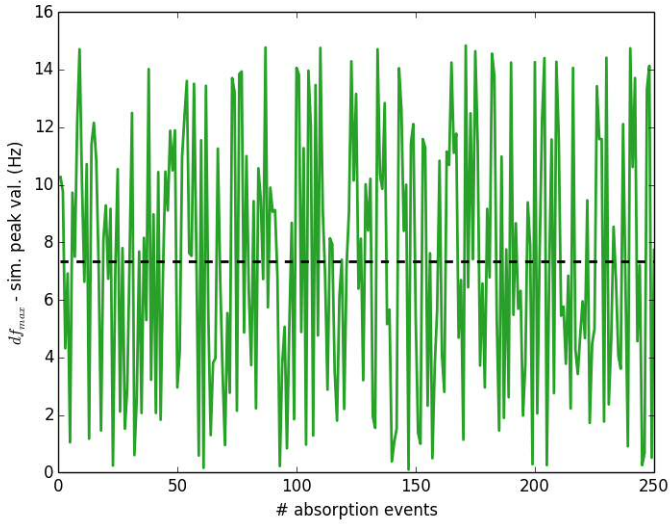

Figure 3.7: Plot of $df_{max}-$ peak value of simulated responses. The dashed black line indicates the average difference.

3.4 Energy Resolution

The performance of a single-photon detector is determined by its energy resolution:

$$\Delta E = h\nu \times \frac{\text{noise}}{\text{signal}}, \tag{3.13}$$

where $h\nu$ is the photon energy. As described in Section 3.2, the NEP for a given detector volume and temperature is fundamentally limited by the random fluctuation in the quasiparticle population: GR noise. For the energy resolution associated with GR noise, the NEP can be converted to a noise equivalent energy (NEE) by multiplying (3.8) by the detector time-constant τ_{qp}, such that

$$NEE_{GR} = 2\Delta\sqrt{N_{qp}\tau_{qp}}; \tag{3.14}$$

which gives the energy resolution in 0.5 s of integration time. For single-photon events, the response is measured over the detector time-constant and is dependent on the number of quasiparticles generated. Therefore, taking into consideration the quasiparticle generation efficiency, the GR noise-limited energy resolution is approximated by

$$\sigma_{GR} = \frac{\Delta}{\eta}\sqrt{2N_{qp}}. \tag{3.15}$$

The fundamental noise for a detector capable of single-photon detection must also be considered. For pair-breaking detectors this is governed by Fano noise. The number of quasiparticles an incident photon can create depends solely upon its energy. However, the resultant number of quasiparticles created during a pair-breaking event will not solely depend on the incident photon. During the same time, existing phonons within the resonator will also interact with (both newly created and already existing) quasiparticles, thus decreasing the total amount of energy available to create further quasiparticles in the cascade. Fano noise takes into account this correlation between the phonons and quasiparticles such that the Fano limit is given by

$$\sigma_{photon} = \sqrt{\frac{h\nu F\Delta}{\eta}}, \tag{3.16}$$

where $F = 0.2$ is the Fano factor [65].

The limit on the energy resolution of a single-photon LEKID can then be given as a combination of the two fundamental limits from (3.15) and (3.16). The convention is to quote the full-width-at-half-maximum (FWHM) energy resolution, where FWHM $= 2.355\sigma$ so that

$$\Delta E_{lim} = 2.355\sqrt{\frac{\Delta^2}{\eta^2}2N_{qp} + \frac{h\nu F\Delta}{\eta}}. \tag{3.17}$$

3.5 Quasiparticle Generation Efficiency

(3.17) shows the ultimate sensitivity of a LEKID, whether it is in the photon noise limit or in the GR noise limit, is dependent on η: the quasiparticle generation efficiency. Consider the initial interaction between an absorbed photon and a Cooper pair. A photon with energy $2\Delta < h\nu < 4\Delta$ can only ever create 2 quasiparticles; the rest of the photon energy is lost to electron-phonon scattering and therefore the quasiparticle generation efficiency must be $\eta < 1$. This means η is not an efficiency in that photons are lost but rather a limit on the detector responsivity. The quasiparticle efficiency factor is generally taken to be $\eta = 0.57$. However, in recent years, it has been found η is dependent on a number of factors.

The quasiparticle generation efficiency of thin-film superconductors (in the context of KIDs) has been modelled as a function of film thickness [66, 67] which has found thicker films of order $\geq$ 100 nm follow the conventional $\eta = 0.57$. However, thinner films of order $\leq$ 30 nm can have $\eta < 0.4$. This is thought to be due to a higher likelihood of phonons escaping into the substrate which are then unable to contribute to the quasiparticle cascade from an incident photon. The likelihood is dependent on the phonon escape time τ_l such that if the phonon escape

time is shorter than that of the average phonon lifetime, phonons are more likely to be lost in substrate. The phonon escape time is dependent on device geometry whereby a thinner film will have a shorter phonon escape time. Note that the phonon escape time is also material dependent. The relationship between η and the phonon escape time is shown in Figure 3.8. Here, ${\tau_0}^{\phi}$ is the characteristic phonon lifetime such that $\tau_l/{\tau_0}^{\phi}$ is the likelihood that a phonon will escape (also referred to as the phonon trapping factor). This value is close to, or less than, unity for thin films and large for thick films. Note ${\tau_0}^{\phi}$ is material dependent.

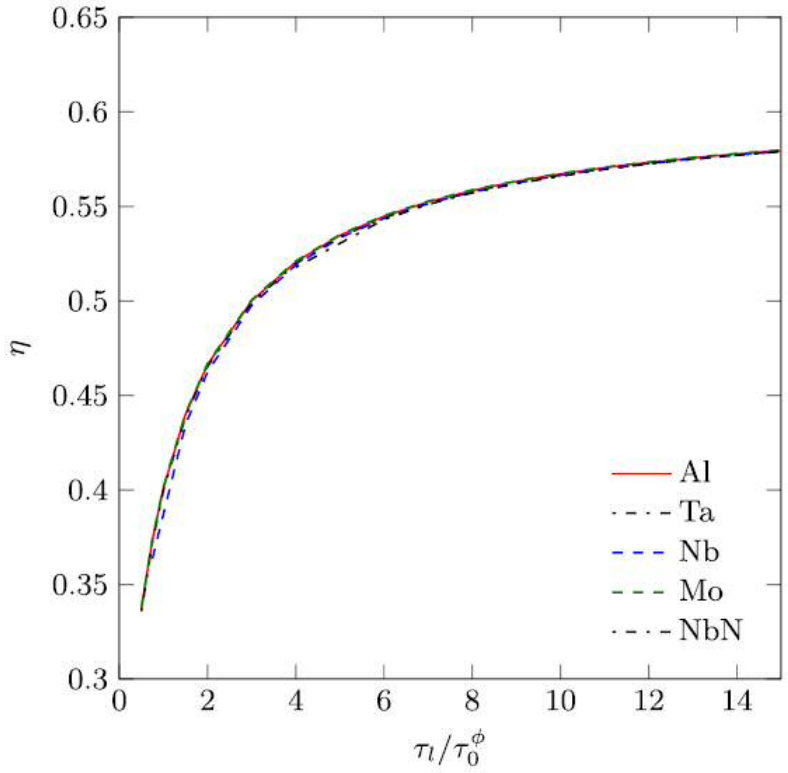

Figure 3.8: Quasiparticle generation efficiency η for materials studied as a function of phonon escape time $\tau_l/{\tau_0}^{\phi}$. Calculations have been made with $T = 0.1T_c$ and $h\nu = 10\Delta$ [67].

η has also been modelled as a function of incident photon energy. This is shown in Figure 3.9. The model assumes unity at photon energies 2Δ since all of the photon energy is used in breaking a single pair. As mentioned, above, until photons

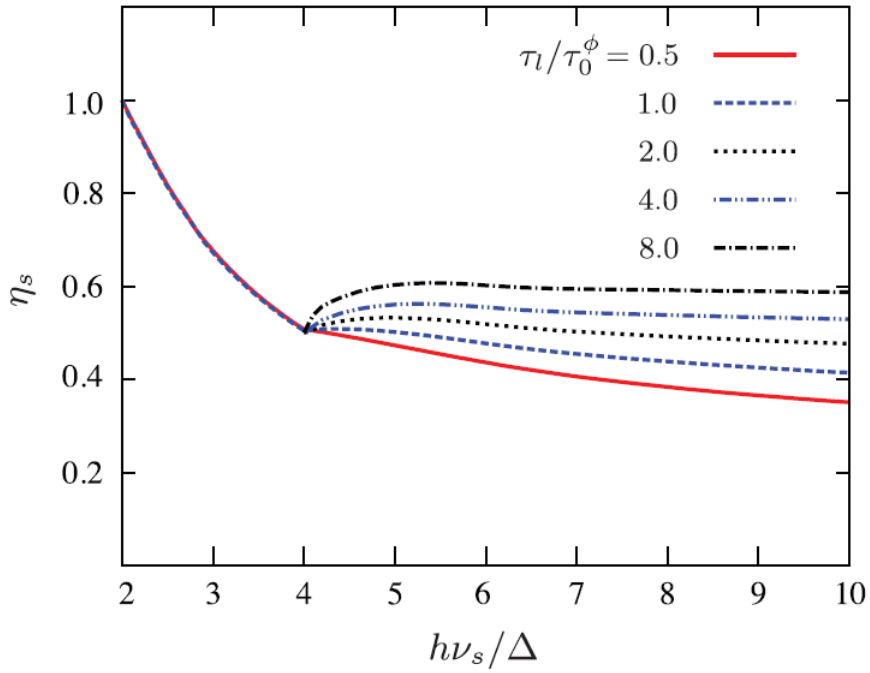

Figure 3.9: Quasiparticle generation efficiency as function of photon energy in units of Δ for different values of $\tau_l/{\tau_0}^\phi$ [67]. Note $\tau_l/{\tau_0}^\phi = 0.5$ corresponds to a film thickness of 30 nm and $\tau_l/{\tau_0}^\phi = 8$ corresponds to 500 nm.

have energies exceeding 4Δ, much of the photon energy will be lost. Thus there is a local minimum at 4Δ. Above, 4Δ it is apparent film thickness plays a heavy role in the efficiency factor. Thicker films appear to rise above the local 4Δ minimum and the settle at $\eta \sim 0.6$; matching the conventional value. Whereas, thinner films appear to settle at lower values or continue to decrease as photon energy increases. At the time of writing, there has not been any work exploring η with photon energies $h\nu \gg 10\Delta$. However, there has been some work attempting to identify differences in the ratio $\tau_l/{\tau_0}^\phi$) via the material dependence of ${\tau_0}^\phi$ [68]. For example, tantalum (Ta) has ${\tau_0}^\phi = 2.27 \times 10^{-11}$ s [68] while Al has ${\tau_0}^\phi = 2.42 \times 10^{-10}$ s [57]. In which case, for the same device geometry, the Ta version could have a value of $\tau_l/{\tau_0}^\phi$ up to (dependeing on material dependence of τ_l) an order of magnitude larger than that of Al and thus will have a larger value for η.

Note that Figures 3.8 and 3.9 are valid for photon energies up to 10Δ whereas optical and near-infrared photons have energies $h\nu \gg 10\Delta$. However, these figures demonstrate the need to further our understanding on the direct effect of photon absorption on the material properties.

Chapter 4

Proof of Concept

In this chapter, single-photon detection in aluminium (Al) LEKIDs is proven. An un-optimised aluminium test array is used to understand and demonstrate single-photon detection. The un-optimised device yielded poor SNR measurements leading to the development of a method to extract detections from noisy data. The work in this chapter has been published [69]. The work and results of the paper are described here in detail. Unless stated, the work discussed here is my own.

4.1 Experimental Set-up

4.1.1 Microwave Readout Electronics

Measurements are made with a Rohde & Schwarz ZNB vector network analyser (VNA) – to sweep across all resonators on the test chip – or a homodyne readout set-up [70], shown in Figure 4.1 – to read a single pixel and measure noise. Figure 4.2 and Figure 4.3 show the schematics of the homodyne set-up and cold electronics, respectively. The cryostat uses a miniature-dilution refrigerator with a base

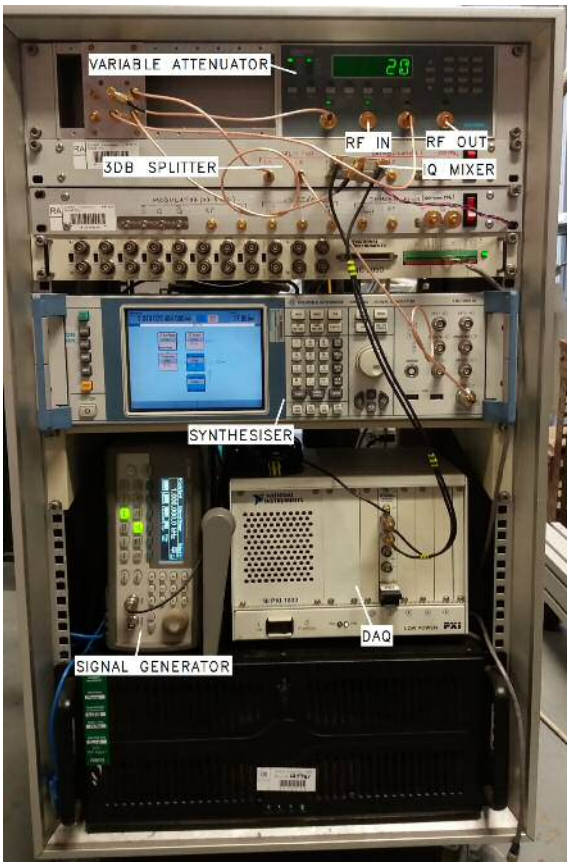

Figure 4.1: Image of the homodyne readout rack. [69].

temperature of 80 mK and a hold time of $\sim$ 10 hrs. Measurements are typically made at 100 mK, the temperature is held stable with a PID system.

A Rohde & Schwarz SMA100A synthesiser provides a tone which is split by a 3 dB splitter, such that half the power is directed to the cryostat and the other half is directly transmitted to the local oscillator (LO) port of a MITEQ IRM0218LC1Q IQ (in-phase/quadrature) mixer. The input to the mixer LO port requires +10 dBm. The synthesiser power is set to apply the recommended input power after accounting for the splitter attenuation and cable losses.

The tone passes through a Aeroflex Weinschel 8310 programmable (variable) attenuator before entering the cryostat. This enables swift readout of different resonators by fine-tuning the appropriate readout power. There are also AtlanTe-

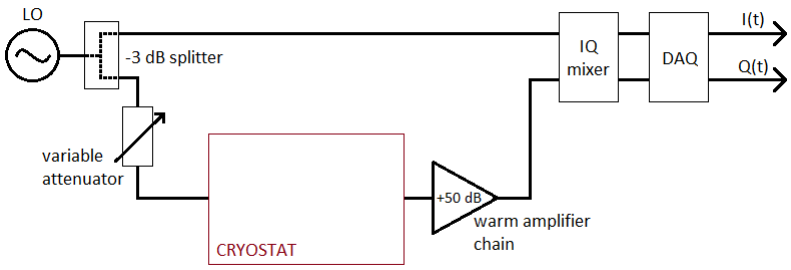

Figure 4.2: Homodyne readout schematic.

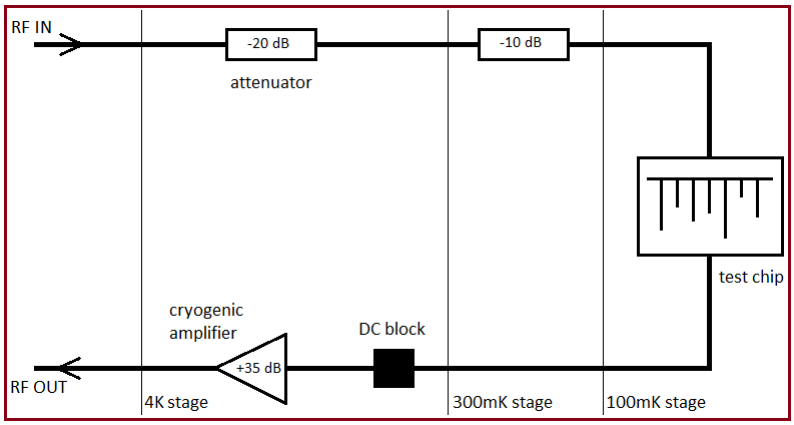

Figure 4.3: Schematic of the cold electronics inside the cryostat.

cRF fixed attenuators at the 4 K and 300 mK stage which reduces thermal power and thermal noise propagating along the RF (radio frequency) cables to the device; which can create undesired pair-breaking events. Once through the device, a DC block is used as a thermal break in the cable; further reducing thermal power propagation though the cables. After probing the device, the tone is then amplified by a custom cryogenic low noise amplifier mounted at the 4 K stage. At room temperature the tone is amplified by a Mini-Circuits ZVA-183WX-S+ warm amplifier chain to boost the signal to the operating level of the IQ mixer and remaining electronics. Note, cold amplification is used to amplify the signal with a low temperature noise so that at room temperature, further noise added by the use of warm amplifiers will be negligible.

At the mixer, the tone from the cryostat is mixed with its original, unprocessed

copy (from the synthesiser). The mixer outputs the real (I) and imaginary (Q) parts of S_{21} as voltages. These signals are then digitised and processed via a National Instruments PXI-1033 data acquisition (DAQ) unit and custom PC software. All electronic components are connected via SMA co-axial cables.

4.1.2 Optical Set-up

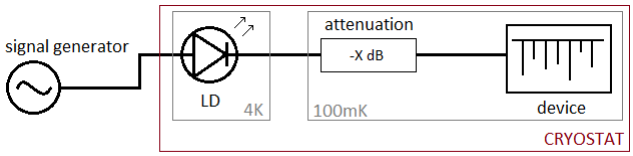

Figure 4.4: Schematic of the optical set-up.

The optical set-up is controlled in tandem with the readout electronics; the schematic is shown in Figure 4.5. A 1550 nm laser diode (LD) is mounted on the 4 K stage. The diode is contained in an aluminium housing which has a standard FC/PC fibre optic bulkhead mounted so that the LD sits in line with the bulkhead's centre. The LD housing is designed so that any light is internally reflected between the diode and the bulkhead therefore ensuring the majority of the diode output power is transmitted to the single-mode fibre optic cable. A signal generator is used to control the LD source; using square-wave, sine-wave or DC power modes. The diode output is carried via by a 9 μm core fibre optic cable which is run up through to the ultra-cold (UC) 100 mK plate; thermalised at the 1 K and 300 mK stages along the way. Before entering the device, the LD output is attenuated. A modified plate, shown in Figure 4.5, ensures roughly half of the pixels are directly illuminated.

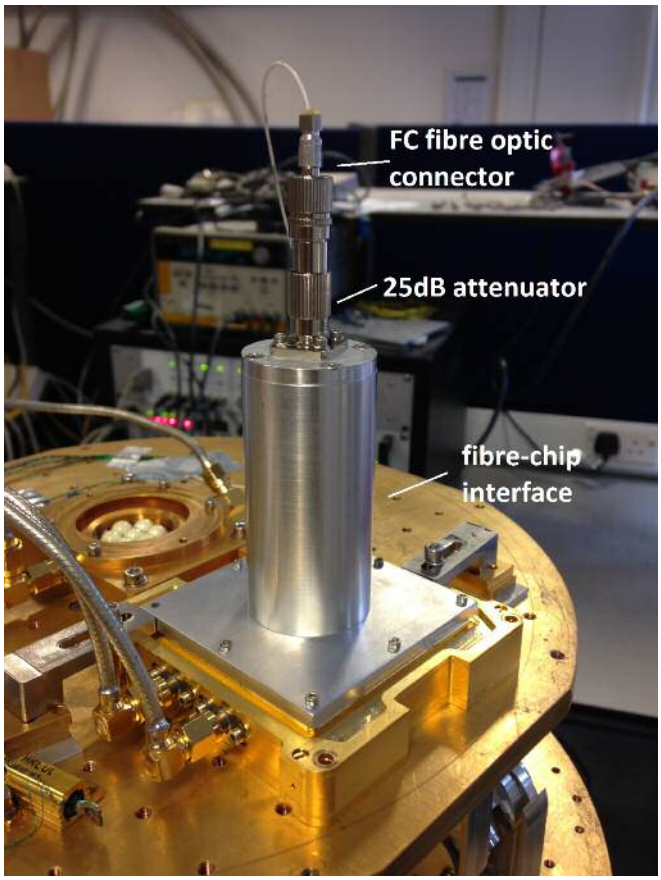

Figure 4.5: Image of the fibre-chip interface [69].

4.1.3 Test Array

To prove the concept of single-photon detection in Al LEKIDs, a rigorously tested device proven to have good sensitivity was used. A 624 pixel LEKID array developed for part of the SpaceKIDs project [71] was therefore chosen; originally optimised as a 350 GHz narrowband Earth observation demonstrator. The array is formed of a 30 nm Al film ($T_c = 1.3$ K) on a 320 μm silicon (Si) substrate. There is an additional low T_c titanium aluminium (TiAl) bi-layer on the backside of the substrate; designed as a phonon absorbing layer to limit the effects of cosmic ray events in the array. The pixel design follows standard LEKID architecture [53] with the inductive meander patterned into a 3rd order Hilbert fractal, shown in Figure

4.6. The array is mounted in a gold-plated copper box which is bolted to the UC stage. The box is designed to ensure the entire chip is fully thermalised with the cold plate.

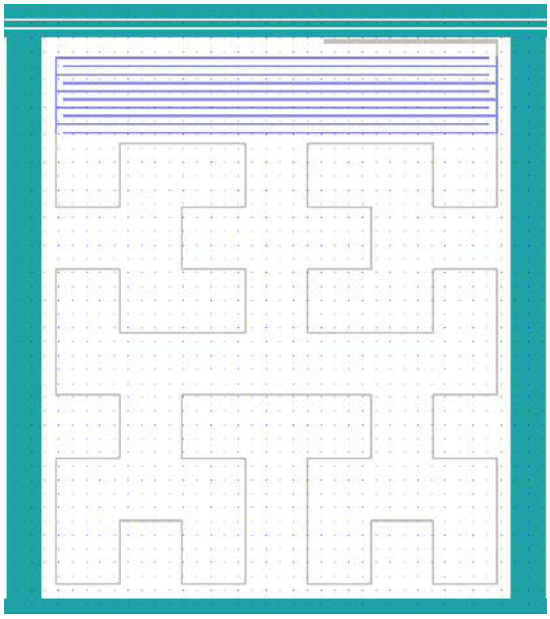

Figure 4.6: Schematic of a SpaceKID pixel.

4.2 Measurements

In this section, the numerous measurements made towards proving single-photon detection is possible with this device are described in detail. Initial measurements are made to ensure the readout equipment is operating correctly. The detectors are swept and noise measurements are taken. These measurements are made dark, unless otherwise stated, for a range of bath temperatures. Values for material properties are also extracted from the measurements before testing the device optically.

4.2.1 Test System Check

Initial measurements are taken with the VNA to check the system throughput of the RF chain; which comprise hardware and cables that pass and process the probing microwave signal. The VNA set-up and RF chain is shown in Figure 4.7.

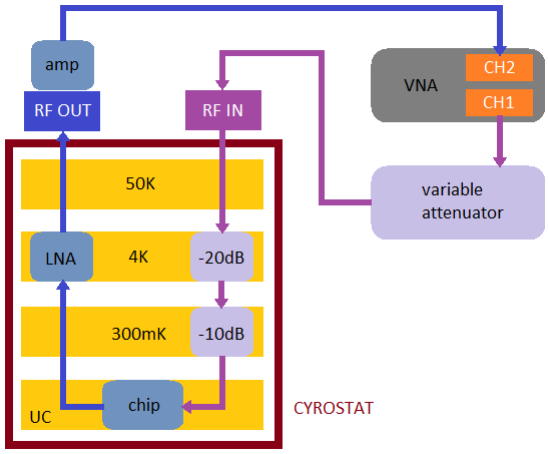

Figure 4.7: RF chain schematic of the test system connected to a VNA.

To check components in the RF chain are operating as expected, the RF signal and noise is modelled to compare with measurements. The signal is computed from resonator sweep simulations – to extract the S_{21} voltage output from the resonator – and the VNA drive power while taking into account attenuation and gain.

The noise computations take into account the component thermal noise at each temperature stage. The noise of an attenuator is given by

$$V_{N,att} = \sqrt{4k_B T R B(1 - 10^{att/10})}, \tag{4.1}$$

where T is the stage temperature, R is the resistance, B is the operating bandwidth and att is the attenuation in decibels (dB). The microwave network is made of a 50Ω transmission line so $R = Z_0 = 50\Omega$. For the amplifiers, which by definition

are thermally black, the voltage noise is given by

$$V_{N,amp} = \sqrt{4k_B TRB}. \tag{4.2}$$

Then the attenuated or amplified noise can be written as

$$V_{N,X} = V_N \sqrt{10^{X/10}}, \tag{4.3}$$

where X is the attenuation or the amplifier gain (in dB). Note the sign must be included such that X is negative for an attenuation or positive for a gain.

For each step in the RF chain (shown in Figure 4.7); starting at the warm (300 K) variable attenuator and ending at the warm amplifier, the input and output noise is computed after each component and added in quadrature. The ultimate noise computation is added to the signal and converted to dB to generate an expected VNA output of S_{21}.

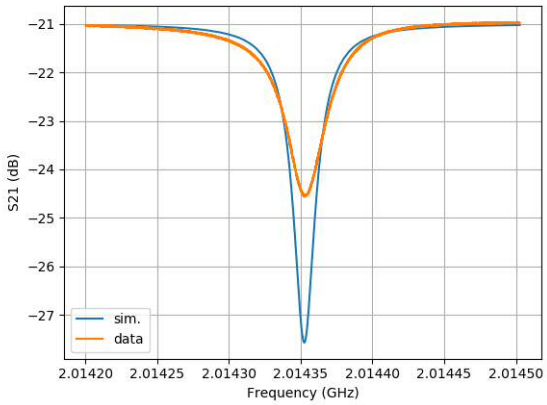

Figure 4.8: Comparison of simulated VNA output (blue) and measured VNA sweep (orange) of a resonator from the test array.

The simulated noise and signal of the RF chain serves as a way of verifying that all electronic components are operating correctly. Large deviations from the model

will indicate some additional noise contribution which could be due to a loose connection, faulty component, etc. Figure 4.8 shows an example of the comparison made between a simulated and measured resonator. The primary check is the S_{21} level; if all the amplifiers are operating correctly and all attenuations are accounted for, the S_{21} level of both the simulated and measured resonator should be equal. In this case, there is a very small difference of <1 dB. This can be attributed to unaccounted cable loss. In general, $\sim \pm 5$ dB difference is acceptable and can be associated with cable loss or slight variations in amplifier performance. Variations between the shape of the simulated and measured resonance dip are purely driven by design and material.

4.2.2 Resonator Sweeps and Time-streams

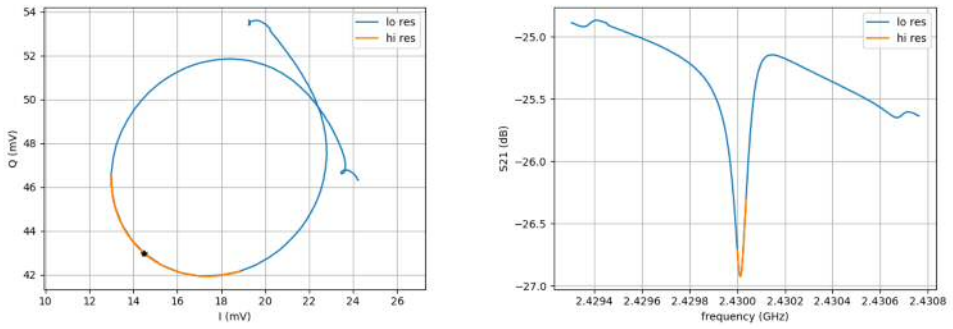

(a) (b)

Figure 4.9: a) Example of a resonance sweep. The star depicts the location of the resonant frequency. b) Example of the equivalent S_{21} amplitude calculated from the sweep. Low (blue) and high (orange) resolution measurements are shown.

The resonator sweep, or IQ circle, is a measure of $I(f)$ and $Q(f)$ as the synthesiser sweeps over a specified frequency range; in equal frequency steps. This range is set by the user of custom-built measurement software in LabVIEW. The sweep is set so that the resonant frequency of the resonator occurs roughly in the

centre of the sweep. An example resonance sweep is shown in Figure 4.9 along with the equivalent S_{21} amplitude, where $S_{21} = \sqrt{I^2 + Q^2}$. A higher resolution sweep is also included to fully resolve the resonance frequency. Once swept, the software finds f_0 from the raw detector response by searching for the frequency at which the value $\sqrt{(dI/df)^2 + (dQ/df)^2}$ is a maximum. Figure 4.10 shows the data points of the resonator sweep and the equivalent response plot. Close to f_0 the detector response increases, hence the distance between data points increases. The resonant frequency is set to the frequency at which the response is at its maximum.

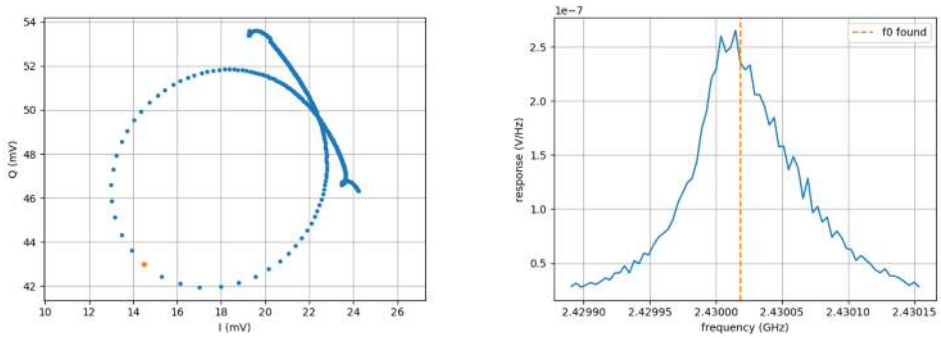

(a) (b)

Figure 4.10: a) Plot of low resolution resonance sweep; orange star depicts location of resonant frequency. b) Example of equivalent detector response as a function of frequency.

Once the resonator is swept, the measurement software is able to use the resonant frequency for continuous wave (CW) measurements. The synthesiser is set to f_0 and $I(t)$ and $Q(t)$ are recorded. The user is able to define the sampling time and sampling rate. The DAQ has a maximum sample rate of 200 kHz.

Using (3.12) from the previous chapter, the raw time-streams $I(t)$ and $Q(t)$ can be converted to $df_0(t)$. Values for the maximum response in I and Q are found from the resonator sweeps. An example is shown in Figure 4.11. Recall, the magnitudes of dI/df and dQ/df are taken to produce a $df_0(t)$ time-stream with positive pulses.

Another method for measuring the detector response is to measure the phase.

Here, the phase is defined as

$$\phi = \arctan \frac{Q(t)}{I(t)}; \tag{4.4}$$

is the angular displacement in the complex IQ plane. To apply this method it is necessary to centre and rotate the IQ circle so that the centre lies at the origin and the resonant frequency lies on the positive x-axis. A full description of this method can be found in [72, 60]. Generally, this method is considered more accurate as it takes into account the decrease in the response moving away from f_0. However, it also tends to generate more noise due to this sensitivity. Whereas the frequency shift method (using (3.12)) assumes a constant response and thus underestimates the noise level. Both methods are in close agreement when the frequency is set close to f_0. Therefore, it has been considered sufficient to employ the frequency shift method in this thesis since it is possible to make measurements close to f_0.

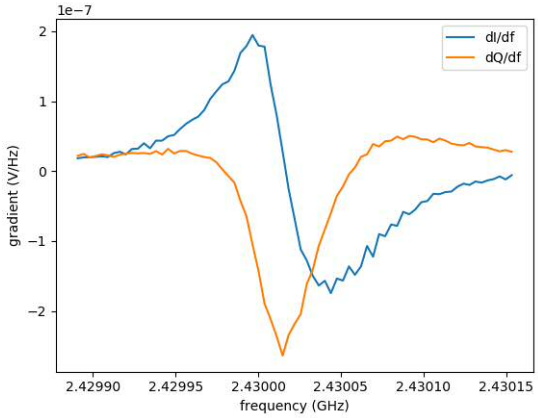

Figure 4.11: Example of I (blue) and Q (orange) gradients from resonator sweep.

4.2.3 Test Array Characteriation

The test array characterisation consists of finding the material properties of the film and the detector responsivity in order to compute the expected photon response for each detector. These measurements are made dark - as in there is no optical stimulus.

4.2.3.1 Quasiparticle Lifetime

Lorentzian Roll-off

The power spectrum density (PSD) is taken of $df_0(t)$. The df_0 PSD can be used to measure the dominant time-constant of the detector: the quasiparticle lifetime. The noise of the detector (on resonance) and system (off resonance) is measured; as shown in Figure 4.12a. The two spectra are subtracted to give the true detector noise and following the example from [63], a Lorentzian can be fitted to the roll-off of the noise spectrum. In the PSD, the Lorentzian takes the form

$$S_N(f) = \frac{4N_{qp}\tau qp}{1 + (2\pi f\tau_{qp})^2} = \frac{p[0]}{1 + (2\pi f p[1])^2}, \tag{4.5}$$

where $p[0]$ and $p[1]$ are the fitting parameters, shown in Figure 4.12b. The fit gives $\tau_{qp} = 43\mu s$ at a bath temperature of 300 mK.

Square-wave Decay

The quasiparticle lifetime can also be measured from illuminating the device with a square-wave signal. A signal generator is used to power the LD with the maximum voltage amplitude at a frequency of 10 Hz. The maximum voltage amplitude is required to ensure the best SNR possible. The detector time-stream is sampled at 200 kHz for 1 second and converted to $df_0(t)$. The measurement is repeated

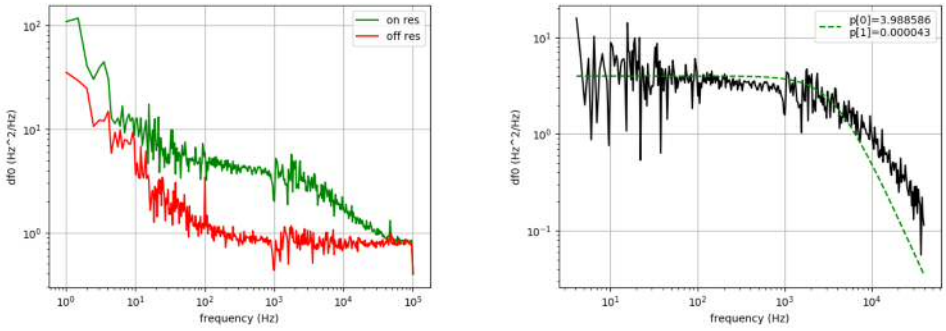

(a) (b)

Figure 4.12: a) PSD from on (green) and off (red) resonance measurements. b) Subtracted PSD (on - off) with Lorentzian (green) fitted to roll-off: $\tau_{qp} = 43 \pm 4 \mu s$; reduced $\chi^2 = 1.66$. Detector measured at 300 mK.

multiple times.

The square-pulses are stacked to increase the SNR. The time-constant of the decay can then be fitted. Note it is important to fit to the correct region. The square pulse decay was fitted at two regions: 0-3 ms and 3-6 ms after the LEKID shows a response to the LD switching off; this is seen in Figure 4.13a. Figure 4.13b shows the difference between extracted values for τ_{qp}. It is thought fitting to the tail will give the true detector time-constant. At this point, most of the quasiparticles will have re-combined putting the system closer to its steady state. This is corroborated by the results described later in this chapter. Fitting to the response too soon after the LD switches off is likely to give a time-constant that is a combination of the detector time-constant and the time-constant of the optics: the signal generator and diode switching off time.

The two methods for extracting τ_{qp} can be combined to produce a full picture of the quasiparticle lifetime saturation. This can be seen in Figure 4.14 which suggests a quasiparticle lifetime saturation temperature of $\sim$ 190 mK. Ideally, both methods would be used for all bath temperatures, however, at temperatures above 200 mK the SNR became too low to fit to the stacked optical square-pulses and below 200

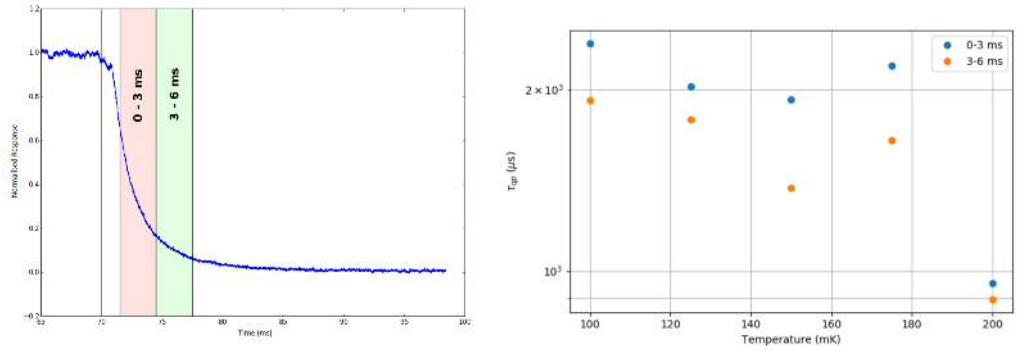

(a) (b)

Figure 4.13: a) Normalised stacked square-pulse response showing the different fitting regions. b) Extracted time-constants from the different fits.

mK the resonator had significant $1/f$ noise making it too difficult to reliably fit to the noise roll-off. Kaplan theory - i.e. using (2.34) - for the quasiparticle lifetime has been fitted to $\tau_{qp}(T > 200\text{mK})$: for this test array $\tau_0 = 191$ ns.

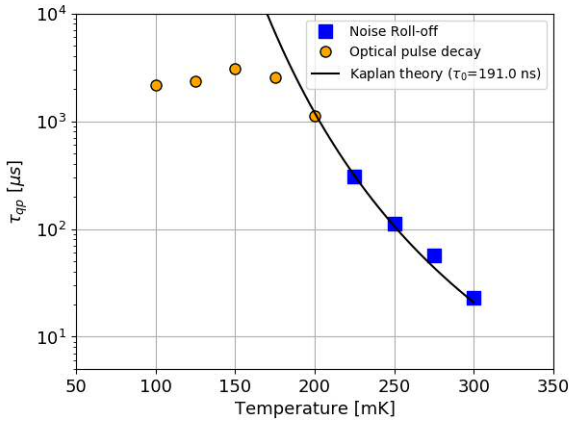

Figure 4.14: Quasiparticle lifetime as a function of bath temperature using the two methods; showing a lifetime saturation temperature of $\sim$ 190 mK for the test array. Kaplan theory is fitted to noise roll-off data (blue) [69]. Error bars have not been included as the relative errors of each data point are $< 1\%$ which will not show on the log-scaled plot.

4.2.3.2 Detector Responsivity

As discussed in the previous chapter, the optical response of a LEKID can be deduced from its thermal response. The resonator is swept at various bath temperatures to measure f_0 as a function of temperature. The VNA is used to sweep across a resonator as it is faster than a synthesizer for high resolution sweeps. Figure 4.15 shows the resonance dip as the bath temperature is increased.

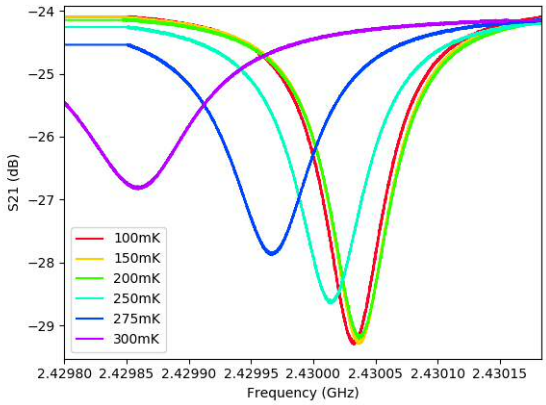

Figure 4.15: VNA sweeps of a resonator as a function of bath temperature.

Notice that at very low temperatures, the resonant frequency increases as the bath temperature is increased. This effect is known as "back bending" and has been attributed to two level system fluctuation (TLF) in the substrate or an oxide layer in the film [73, 53]. This is where the dielectric constant of the substrate or oxide layer changes as a function of temperature. At very low temperatures, this change can dominate over the change in kinetic inductance of the detector and therefore registers as an increase in resonant frequency. Back bending is not expected to be an issue under optical illumination as the substrate and oxide layer remains at the same temperature. Figure 4.16a shows back bending more clearly. At temperatures < 200 mK, the effects of TLF dominate over the effects of change in kinetic inductance causing an increased resonant frequency not predicted by

superconductor theory. As the temperature increases further, the change in kinetic inductance dominates and thus behaviour in line with superconductor theory is observed.

The detector responsivity is taken to be the change in f_0 as a function of quasiparticle population df_0/dN_{qp}. The quasiparticle population is temperature-dependent, so for each measured bath temperature, N_{qp} is computed using (2.33) and plotted against the detector response. This is shown in Figure 4.16b. Since there is a linear relationship between f_0 and N_{qp}, the detector responsivity can be found from the gradient of a linear fit. To avoid skewing from back-bending and the quasiparticle saturation, only the high temperature data points are fitted.

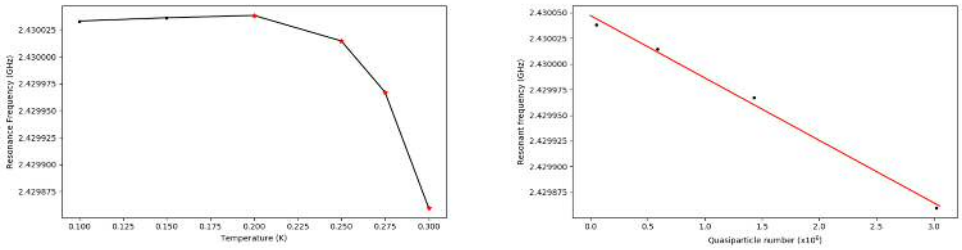

(a) (b)

Figure 4.16: a) Resonant frequency as a function of bath temperature. Data points in red are used for further analysis to avoid the effect of back bending. b) Detector response: f_0 as a function of quasiparticle population. A linear line (red) is fitted to the data to give $df_0/dN_{qp} = 0.06$ Hz/quasiparticle.

4.2.3.3 Expected Single-Photon Response

With the detector responsivity and test array properties characterised, the expected photon response can be simulated. Following the single-photon detection model described in Chapter 3, the response to single and multiple absorption events is simulated and shown in Figure 4.17. For the detector chosen, the expected maximum pulse height for a 1550 nm single-photon absorption event is 119 Hz. Here,

it is important to note a quasiparticle creation efficiency $\eta = 0.4$ has been used for the model. This is an estimate based on the material and film thickness [66, 67].

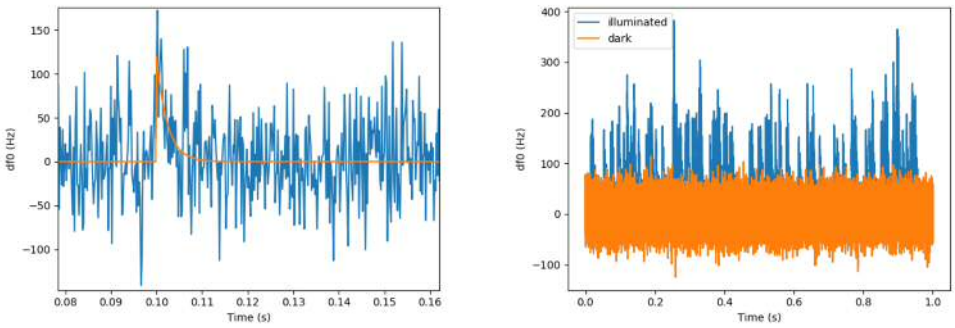

(a) (b)

Figure 4.17: a) Simulated expected detector response df_0 to single-photon absorption incident at 100 ms. Noiseless signal is shown in orange. b) Simulated df_0 time-stream with (blue) and without (orange) multiple photons: $n = 100, \lambda = 1550$ nm. Here photons are injected at random time intervals and variation in pulse height can be a result of the maximum response falling between DAQ sampling intervals.

4.2.4 Optical Measurements

As there is no way to measure the optical power incident on the array in this test set-up, preliminary measurements are made to find detectors which show a clear optical response. In such a case, the LD is set to a high voltage so that the df_0 level of the df_0 time-stream rises significantly. This rise is due to an increased equilibrium quasiparticle population that fluctuates as a result of the photon shot noise: $NEP_{shot} = \sqrt{2Ph\nu/\eta}$ [74]. In this scenario, the detector is saturated with incident photons (events overlap and are indistinguishable). To be able to detect single-photons, the detector should remain at the same df_0 level as it is when it is dark. Therefore, low LD power is required. Figure 4.18 shows an example of the method employed to find the optimum LD power level. Figure 4.19 shows an example of a tuned optical measurement. The LD was set to 4 V and 3 mA. Once

the LD power is tuned, a set of dark measurements are taken: resonance sweep and time-stream. The LD is then switched on and another time-stream is taken. This set of measurements are repeated several times to generate better statistics once analysed.

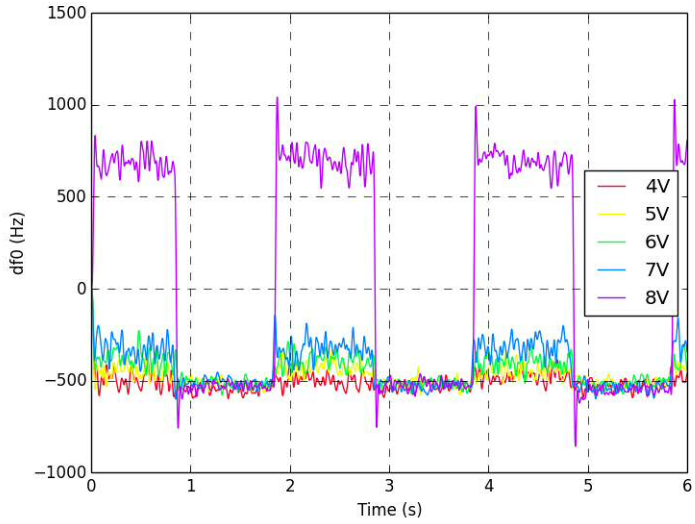

Figure 4.18: Measured detector response to LD square wave signal set at varying voltages. $\lambda = 1550$ nm.

Figure 4.19 shows a definite difference between the illuminated and dark response of the detector. Note the response does not lie exactly about zero (which corresponds to f_0). This is likely due to a slight mis-match in the value of f_0 identified by the measurement software. The offset towards the negative indicates the resonant frequency of the device is slightly higher than has been identified by the software. Since the offset is small and there is a clear response it can be assumed the synthesiser has been set to an appropriate frequency.

It may be possible the peaks above the dark noise level are due to the LD voltage being slightly too high. In this case, rather than saturating the detector with too many photons, the chip may be absorbing enough photons to marginally raise the temperature of the device. The result being a broader noise level. It is expected

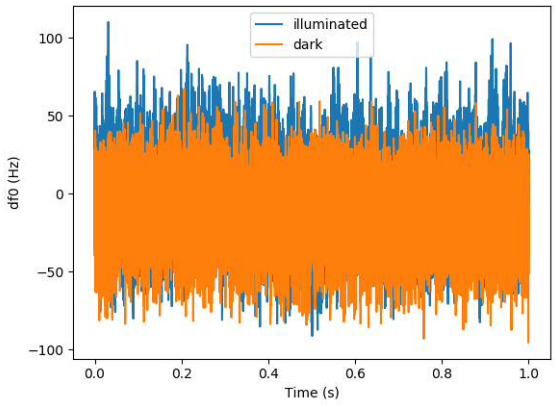

Figure 4.19: Measured detector response with LD on (blue) and off (orange). $\lambda = 1550$ nm.

only a few photons per second are absorbed within the detector volume at this low power level. When compared to the simulated response (shown in Figure 17b), this can be seen more clearly. There are 100 absorbed photons per second in the simulation. This leads to many occurances of double - or even triple - absorption events and many more overlapping events. The difference between the simulation and measurement may also be due to a higher simulated value of $\tau_{qp} \sim 2.6$ ms based on Kaplan theory at the saturation temperature 190 mK. A longer lifetime means the DAQ is able to sample more of the pulse decay. There is also an apparent broader noise in the simulated dark time-stream. This may be due to a slight overestimation of the detector volume since $\sigma_{GR} \propto \sqrt{N_{qp}} \propto \sqrt{n_{qp}V}$.

Notice also that there are very few data points above 100 Hz in Figure 4.19. As previously mentioned, measurements were repeated to generate good statistics.

4.3 Detection Extraction

4.3.1 Method

From Figure 4.19, it is clear the detector has a poor signal-to-noise ratio (SNR). The measurements qualitatively compare reasonably well with simulations, but a quantitative analysis is required to evaluate the performance of the detector. To do this, single-photon absorption events must be identified and their responses measured. Following the example from [42], the illuminated and dark detector time-streams were Weiner filtered, with a bandwidth of 2 kHz, and potential absorption events were identified by a matched filter. Here, it should be stated this detection extraction work was carried out by a co-author from [69]. The remaining analysis on the extracted detections was carried out by myself.

The extracted detections were stacked and averaged. This can be seen in Figure 4.20 where an exponential was fitted to find the decay time-constant. It was found to match the measured quasiparticle lifetime from the square-wave measurements made at 100 mK, suggesting the extracted detections are due to absorption events. Note, the negative tail of the pulse is an artefact of the extraction method employed.

4.3.2 Analysis

Figure 4.21a shows the resulting detection counts from the extraction method applied to both the dark and illuminated detector. The dark detections are subtracted from the illuminated detection (using a coefficient of 1) to produce an assumed photon absorption event distribution, shown in Figure 4.21b. Note that data below 50 Hz is not shown in the right plot; the data is noisy and detracts from the

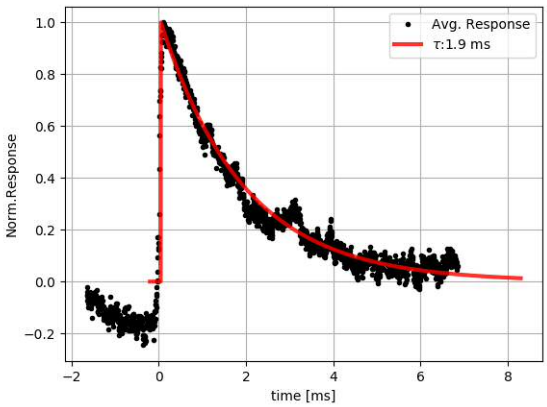

Figure 4.20: Stacked (of order 10^4) and averaged detections extracted from the illuminated detector time-stream. An exponential decay (red) is fitted to the data: $\tau = 1.9$ ms.

remaining distribution.

The dark counts are taken to be false detections due to the limitations of the detection extraction method. The illuminated counts will then be a combination of false and true detections. There is a very clear excess of counts in the illuminated detector with amplitude > 200 Hz. These are attributed to true photon absorption events. True detections with amplitudes < 200 Hz are much harder to discern from the false events. These limitations are depicted by the error bars, though there still appears to be a peak at $\sim$ 120 Hz in the absorption distribution. This matches the expected maximum pulse height of a single-photon absorption event for this detector; shown in Figure 4.17a. There may also be a secondary peak at ~ 240 Hz with very small error bars; indicative of 2-photon absorption events.

Following (3.13), an estimate for the energy resolution of the detector can be made. The noise can be given by the FWHM of the absorption distribution and the signal can be given by the peak value; thus $\Delta E_{meas} = 662 \pm 9$ meV.

Recall (3.17), N_{qp} is dependent on both detector volume and bath temperature while Δ depends on bath temperature. This can be seen more clearly in Figure 4.22.

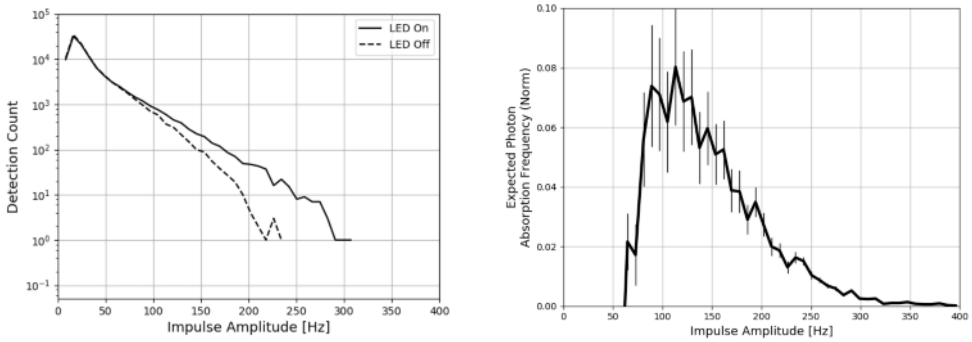

(a) (b)

Figure 4.21: a) Impulse detection counts as a function of impulse amplitude; detection counts shown for both dark (LED off) and illuminated (LED on) detector. b) Normalised expected photon absorption event distribution [69].

Therefore, to ensure a reliable comparison between measurement and theory, the expected energy resolution has been calculated to take into account the saturation temperature and is specific to the detector under examination; such that $\Delta E_{lim} = 668$ meV. Note that this value also takies into account the fact the Weiner filtering process reduces the integration time to $\sim \tau_{qp}/4$ which leads to a $\sqrt{4}$ increase in GR noise contributions.

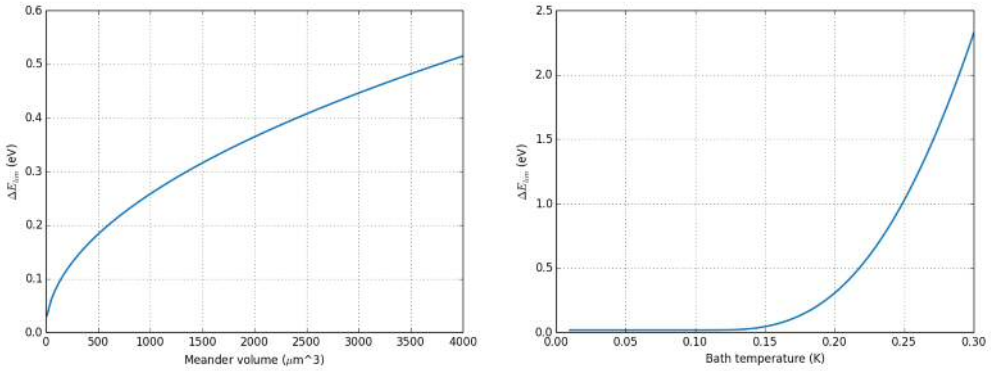

(a) (b)

Figure 4.22: a) ΔE_{lim} as a function of detector volume; with bath temperature set to $T = 200$ K. b) ΔE_{lim} as a function of bath temperature; with detector volume set to $V = 1400 \mu m^3$.

4.3.3 Discussion

Here it should be reinforced that this test device was not optimised for single-photon detection. The detectors have a reasonably large volume, $V \sim 1400\mu\text{m}^3$, and aluminium is a poor choice of material for single-photon detection with its high reflectivity at optical and near-infrared wavelengths ad relatively low kinetic inductance. This is evident from the poor SNR. The single-photon response is too low. Still, the extracted detections corroborate the measured value for τ_{qp} and analysis on the absorption distribution matches expectations: ~ 120 Hz peak and $\Delta E_{meas} = 662$ meV.

The expected maximum response to a single 1550 nm photon was $df_{0,max} = 119$ Hz, for this detector. The apparent peak in Figure 4.21b at ~ 120 Hz is very close to $df_{0,max}$. This suggests the detection model described in the previous chapter provides a good representation of a LEKID response to single-photon absorption events. While the proximity between ΔE_{lim} and ΔE_{meas} suggests a decent understanding of the limiting factors of a LEKID's sensitivity.

Since the device has poor SNR, the absorption distribution does not form a well-defined Gaussian; as would be expected. This means neither the peak nor the FWHM can be well-defined. It is possible there is a peak at ~ 240 Hz which may be skewing the Gaussian. Thus the FWHM may well be an overestimate.

4.4 Conclusions

The results presented in this chapter shows the first known measurement of single-photon detection in aluminium LEKIDs. At the time of writing, this is also the first known work to make use of a value for the quasiparticle efficiency factor different from the traditional $\eta = 0.57$. The reasonable match in both the peak value and

energy resolution, from the absorption distribution, asserts the use of $\eta = 0.4$ is valid for this device. Had $\eta = 0.57$ been used, this would have yielded $df_{0,max} \sim 170$ Hz and $\Delta E_{lim} \sim 470$ meV. This is a significant and measurable difference which has not been observed.

This work also shows the saturation temperature of a material cannot be ignored as it is a limiting component in a LEKID's response and sensitivity.

Given the use of aluminium and the poor SNR, better statistics and higher energy photons are required to fully confirm the single-photon detection model. Thus an optimised single-photon LEKID array has been developed to further probe understanding of LEKID response to single-photon absorption. The design process is discussed in the following chapter.

Chapter 5

Single-Photon LEKID Design Evolution

5.1 Design Considerations

5.1.1 LEKID Architecture

There now exist various LEKID designs, some examples of which can be found in [9, 74, 75]. All are variations on the standard LEKID architecture outlined in [53] which has been chosen as the foundation for the optimised LEKID design. Figure 5.1 shows the basic elements and structure of a LEKID. Its simple design provides a smaller margin of error with regards to fabrication and the aim of exploring the limitations of single-photon detection in LEKIDs.

Figure 5.1 shows a resonator that is capacitively coupled to the feedline. It is possible to inductively couple the same resonator by rotating the resonator 180°. Some designs may have a coupling preference in that the resonator may be more

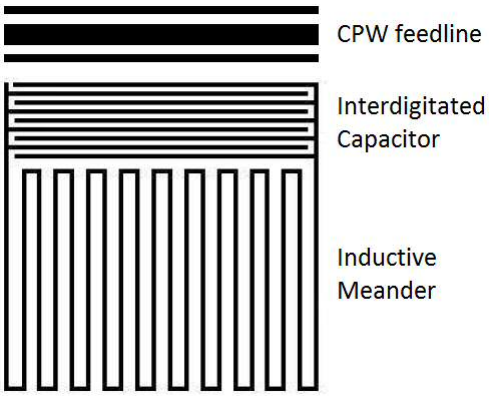

Figure 5.1: Schematic of a basic LEKID design.

strongly coupled via inductance or capacitance. All resonators described in this thesis are capacitively-coupled devices as they tend to be more easily tuned for resonance frequency and Q-factor.

5.1.2 Readout Frequency

To maximise the signal-to-noise ratio (SNR), the resonators are designed with resonant frequencies that are well within range of the readout hardware. The hard frequency limits are governed by the performance of the amplifiers used in the readout chain.

5.1.3 Cross-talk

LEKID arrays with closely-packed resonators – in both the physical and frequency domains – experience significant cross-talk. This is where resonators couple with each other as well as the feedline, leading to altered resonant frequencies and Q-factors. The effects are more severe when pixels with similar resonant frequencies are physically nearby [76]. This can be minimised by staggering pixels in the frequency domain [77] and including a ground shield (or ground plane) around the

pixel [78], as can be seen in Figure 5.2. The ultimate arrangement of pixels tends to depend on the physical size of the array, the number of pixels and the frequency bandwidth.

5.1.4 Quality Factor

For capacitively coupled resonators, the overall coupling is determined by the capacitance between the coupling capacitor and the co-planar waveguide (CPW) feedline. This can be manipulated by changing the distance between the resonator and the feedline, as well as the general geometry of the interdigitated capacitor (IDC) e.g. capacitor finger length, line width, line separation, etc. It is also possible to include a coupling finger (an example can be seen in Figure 5.2), which can be modified in the same ways as the IDC to acquire the desired Q-factor. Varying the total capacitance of the resonator in this way can also allow a fine-tuning of the resonant frequency.

5.2 Material

The primary material used for single-photon detection with KIDs has been titanium nitride (TiN) [79, 42]. It has high kinetic inductance and tuneable superconducting properties but films suffer from spatial non-uniformities which can generate non-linear response from pixel to pixel. Another material – relatively new for KIDs - is platinum silicide (PtSi) which has shown promising results [80, 81]. The material also has high kinetic inductance, some tunability and has shown better uniformity than TiN. However, TiN has been shown to deviate from conventional superconductivity theory [79] and PtSi has not yet been explored in this respect. As this work concerns finding the ultimate limit on performance guided

by theory, aluminium (Al) has been chosen for this test array. It has already been shown capable of single-photon detection and is a well-understood material in the context of KIDs. Although it has low kinetic inductance and poor optical efficiency at optical frequencies, the results from the previous chapter show it is possible to further explore the physics of energy-resolving detection in LEKIDs.

5.2.1 Bi-layer

Comments made in [42] suggested a broadened energy resolution was the result of partial responses due to absorption events in the IDC. In response to this, it was thought appropriate to also investigate this effect by including resonators with an additional absorbing layer covering the IDC. The desired effect of such an absorber is to minimise any measurable response generated by absorbed photons in this region. This requires a material with a higher critical temperature and shorter quasiparticle lifetime than aluminium.

Niobium (Nb) is a reasonably well-understood type-1 superconductor which has been successfully used as a material for KIDs and fits the above requirements. It has a typical critical temperature of ~ 9 K. High quality Nb films can have lifetimes of up to $\tau_{qp} \sim 600$ μs [62] but standard films have of order $\tau_{qp} \sim 10$s μs [82]; measured at $T/T_c \sim 0.11$. Al has longer lifetimes, up to ~ 3 ms in high quality films [83] while regular films tend to have lifetimes of order $\tau_{qp} \sim 100$s μs; measured at $T/T_c \sim 0.15$. The devices are fabricated in-house in a densely populated clean-room environment. It is not expected the films will be of the highest quality and hence it is expected the Nb film will have a shorter lifetime than the Al film. Thus Al resonators with an additional Nb layer covering the IDC region are included in the test array; these are referred to as hybrid device. There are also Al resonators with a Nb layer covering the entire resonator structure for reference;

these are referred to as NbAl or bi-layer devices. Note, since the layers are composed of thin films, it is expected the regions of bi-layer will proximitise and behave as a single superconducting material which will have material properties that differ from its composite materials. The bi-layer is formed of 125 nm Nb and 25 nm Al.

To summarise, for each resonator design, there are three versions: entirely Al, entirely NbAl bi-layer and a hybrid; with NbAl bi-layer for the coupling and IDC and an Al meander.

5.3 Volume Exploration

Following from (3.6), it can be seen that the response $R \propto 1/V$. Therefore, a smaller volume should increase responsivity of the device. A smaller volume should also improve the energy resolution given (3.17) since $\Delta E \propto \sqrt{N_{qp}} \propto \sqrt{V}$. Therefore, the test array will have a number of different detector (meander) volumes, with the aim of exploring the dependence of detector volume in the detector response.

5.4 Pixel Design

5.4.1 Design A: SpaceKID Reference

Although the SpaceKID design was not optimised for single-photon absorption, it is known to produce reliable, high-sensitivity detectors. Having proven the ability of single-photon detection in Al LEKIDs with this design, these pixel designs were included in the test array as reference guides. The replica design in shown in Figure 5.2. Here, the number of capacitor fingers in the IDC has been increased to reduce the resonant frequency of the device. The capacitor and inductor features have 4μm line width. The IDC fingers have a line separation of 20μm. The coupling

finger has line width 12μm with a varied length to fine-tune the Q of the pixel.

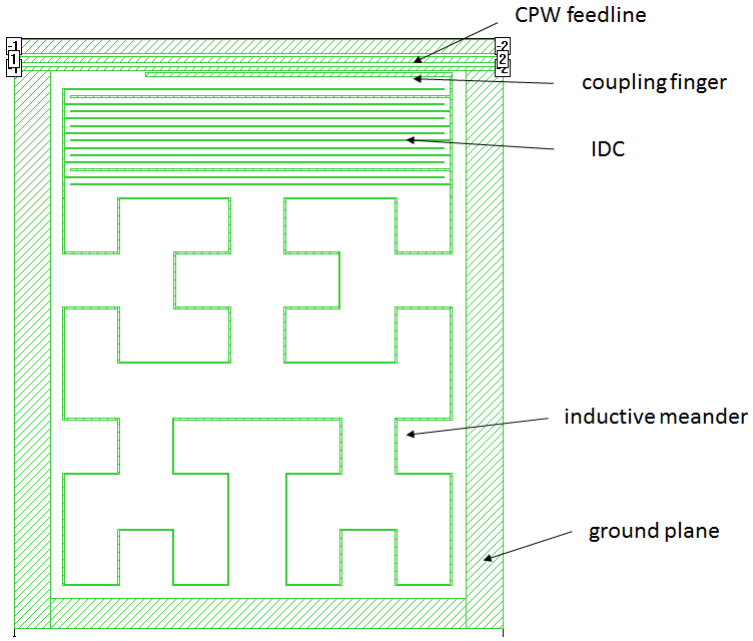

Figure 5.2: Schematic of the SpaceKID replica design.

The pixels have been uniformly scaled down to achieve smaller volumes. There are three versions of the SpaceKID pixel: (full size) 1:1, 1:0.65 and 1:0.5 size ratios.

5.4.2 Design B: Optimised Single-Photon LEKID

Based on the standard architecture of the LEKIDs described in Section 5.1.1, an optimised LEKID has been developed for single-photon absorption. The main driver of the design process was to create resonators with smaller volumes.

Figure 5.3 shows the optimised single-photon LEKID design. Notice the interdigitated capacitor (IDC) is significantly larger than the inductive meander region. This is due to electronic readout constraints which limit the resonant frequency of the pixel to 1 GHz < f_0 < 8 GHz. Recall $\omega_0 = 1/\sqrt{LC}$; a smaller inductive meander leads to a smaller inductance L and thus increases the resonance frequency. To compensate, the capacitance C must be increased; hence the large IDC.

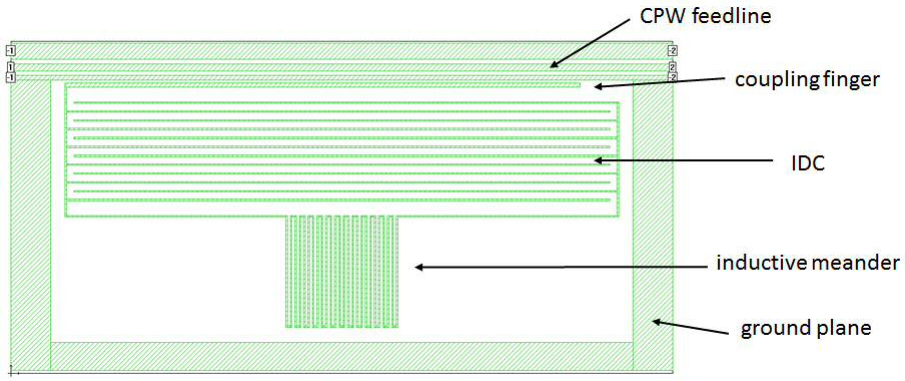

Figure 5.3: Schematic of the optimised single-photon pixel design.

Rather than scaling the entire pixel, the IDC widths are kept unchanged and the meander is scaled in size ($\times 1$, $\times 0.5$ and $\times 0.1$). The pixel, of this design, with the largest meander has approximately $\times 0.75$ the volume (assuming a uniform film thickness across the array) of the largest SpaceKID pixel meander. All pixel features have the same feature dimensions: meander and IDC finger line width is 4μm. The IDC has 20μm line separation and the coupling finger has line width 12μm with a varied length to fine-tune the Q of the pixel. The meander has a line separation of 8μm.

5.5 Test Array Design

This test chip aims to explore the difference between two types of resonator design (A: SpaceKID reference and B: optimised), the volume-dependency of detector responsivity and to investigate how the bi-layer devices affect the resulting energy resolution. Given the number of different resonators, with different properties, it is necessary to ensure the resonators can be easily identifiable. Table 5.1 shows the design properties of each pixel in the test array.

The resonators were designed using SONNET software [84], which evaluates the electromagnetic properties of the resonant structure. The S_{21} transmission is

computed from which the resonance and total Q-factor can be extracted.

Note the pixels have been designed to have roughly the same Q to minimise the number of variables. However, the high frequency pixels have a much stronger coupling to the feedline due to the higher frequency and smaller resonator capacitance; recall $Q_c = 2C_{res}/\omega_0 {C_c}^2 Z_0$. The detector volumes are based on a 25 nm Al layer. The NbAl devices are not intended for optical measurement.

Table 5.1: Resonator design properties.

LEKID	Design set	Design	V (μm^3)	Material	f_0 (GHz)	Q ($\times 10^4$)
1				Al	1.893	2.55
2	I	A	1139.2	hybrid	2.110	2.60
3				NbAl	2.305	2.31
4				Al	2.563	3.12
5	II	B	810.4	hybrid	2.954	3.33
6				NbAl	3.318	2.76
7				Al	3.522	2.07
8	III	A	761.2	hybrid	3.859	1.98
9				NbAl	4.203	1.83
10				Al	4.401	2.13
11	IV	B	388	hybrid	4.916	1.01
12				NbAl	5.436	1.53
13				Al	5.666	1.61
14	V	A	561.4	hybrid	6.166	1.55
15				NbAl	6.662	1.45
16				Al	6.848	0.43
17	VI	B	82.4	hybrid	7.428	0.42
18				NbAl	8.002	1.08

5.5.1 Pixel Distribution

The resonators have been designed to lie in clearly defined triplets: Al, Al-NbAl hybrid and NbAl detectors. Due to the unknown kinetic inductance of the bi-layer, the resonators were designed with $L_k = 1$ pH/sq – the typical kinetic inductance of Al of thickness 25 nm. The Nb layer is expected to have a significantly lower kinetic

inductance than Al due to its significantly higher T_c and larger film thickness.

The bi-layer is formed of 125 nm Nb and 25 nm Al. Since the Nb makes up the larger proportion of the total bi-layer volume, it is expected to behave more like Nb (once proximitised). Therefore, the hybrid and NbAl devices should have a lower kinetic inductance than the Al device and hence will have a higher resonant frequency than that of its Al version design. With this in mind, the sets of triplets were separated far enough so that the true resonant frequency of the NbAl device of the previous set would be at least 200 MHz lower than the resonant frequency of the following Al device. The worst case scenario, with zero kinetic inductance, was simulated to find the maximum possible frequency increase of the NbAl device. The hybrid devices are expected to lie somewhere in between the Al and NbAl devices, therefore the hybrid devices were simulated with $L_k = 0.5$ pH/sq as a very rough estimation. Figure 5.4 shows the expected frequency distribution of the resonators. Note the resonators have been simulated according to the model described in Section 4.2.1 to show the expected frequency distribution of the resonators as measured through the test system.

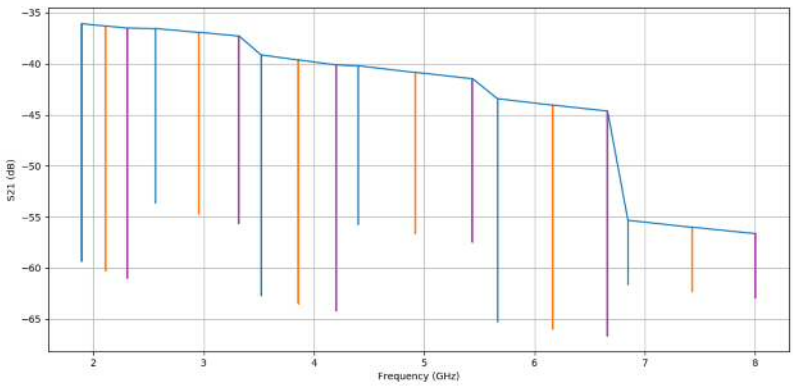

Figure 5.4: Expected frequency distribution of resonators, accounting for a lower Nb kinetic inductance. The entirely Al resonators are shown in blue; the hybrid resonators in orange and the entirely NbAl resonators in purple.

Figure 5.5 shows the physical distribution of the pixels. They have been arranged to minimise cross-talk. The 18 pixels have been drawn directly opposite each other in an attempt to minimise potential differences across the feedline.

5.5.2 Chip Design

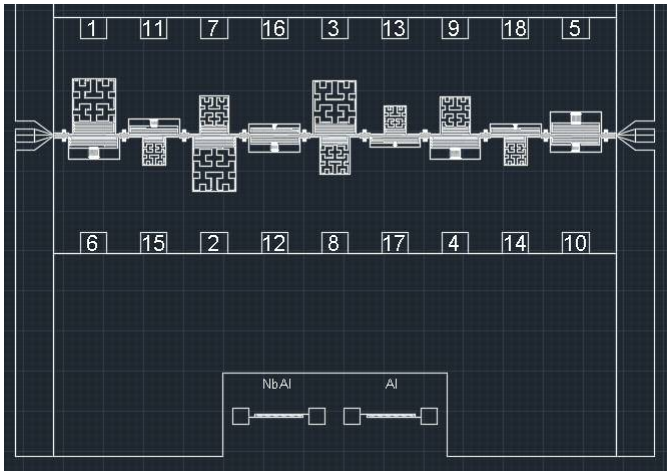

Figure 5.5: Drawing of the chip design showing the physical distribution of pixels across the test array. The number above and below the pixel corresponds to the LEKID design from Table 5.1.

Figure 5.5 shows the DC test structures at the bottom of the array. These have been included for DC measurements of the resistance as a function of bath temperature. These allow measurement of the critical temperature of the film and normal resistance which are included in the modelling of the detectors. There are two test structures: one with Al layer only and another with the NbAl bi-layer; as labelled in the drawing. The NbAl test structure also serves to show how the bi-layer has proximitised i.e more closely with Al or Nb material properties.

5.6 Fabrication

The NbAl bi-layer was sputterd onto a sapphire wafer. The move away from a silicon substrate (used for the device described in Chapter 4) was to enable the use of higher energy photons. The Al layer (25 nm) was deposited first, the Nb layer (125 nm) deposited second. The Nb layer was patterned using standard photo-lithography and then fluorine etched which stops at the Al layer. The Al layer is then pattern, also using standard photo-lithography, and wet etched with a phosphorous + nitric acid + water solution. This solution etches the Al layer only; the remaining sections of Nb/Al layer after the first etch and the sapphire substrate are untouched.

Images of the triplet set of a design A set V from Table 5.1 can be seen in Figure 5.6. The ground plane and CPW feedline are formed of the Al layer.

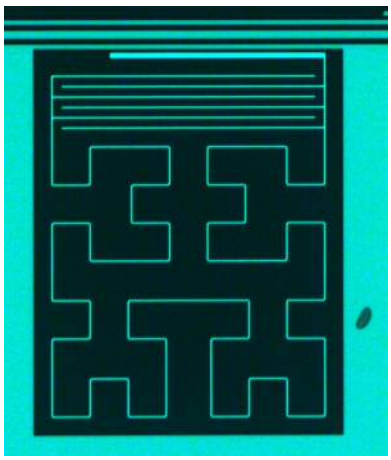

(a)

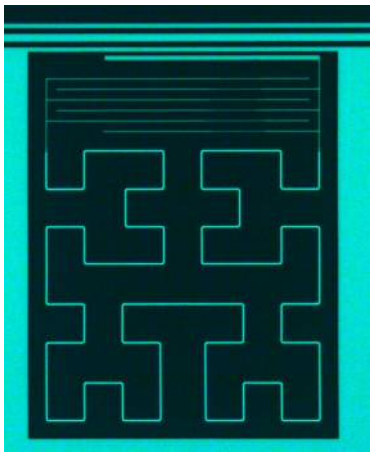

(b)

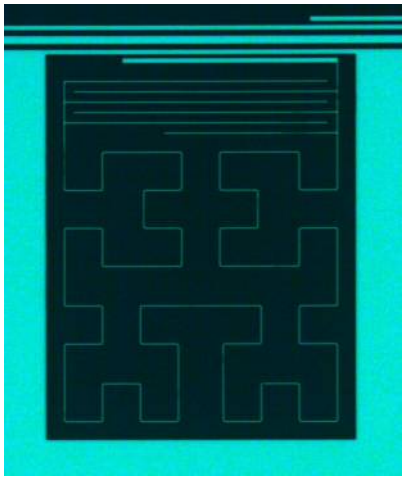

(c)

Figure 5.6: Image of a SpaceKID replica design: a) Al version, b) hybrid version and c) NbAl version.

Chapter 6

Local Response Dependence

As mentioned in Chapter 4, there is a possibility photon absorption in the interdigitated capacitor (IDC) can lead to partial measureable responses which will broaden the absorption distribution – and hence energy resolution. Although not observed in measurements discussed in Chapter 4, it was worth investigating given the breadth of designs contained in the single-photon LEKID test array. Any variation in the response due to the location of an absorption event will be referred to as the local response dependence.

The detecting element of a LEKID is the inductive meander which has high current density and a uniform current distribution. This is shown in Figure 6.1a. Photons incident on the chip can and will be absorbed at any part of the LEKID structure. However, photons absorbed in the meander will generate a significantly higher response than anywhere else due to the high current density. The uniform current distribution means the response generated by photon absorption should be the same regardless of the absorption event location within the meander. However, due to the readout constraints it is not always possible to ensure the inductor and

capacitor function as separate components. Figure 6.1b shows a LEKID with some current leaking into the capacitor region. Here, the capacitor can be considered a kind of hybrid as it also has some inductive element. In such a device, it is possible photon absorption in the capacitor regions with reasonably high current density will generate a partial response (i.e. a diminished response in comparison to an absorption event in the meander). Partial responses will lead to a broadening of the ultimate energy resolution of a device.

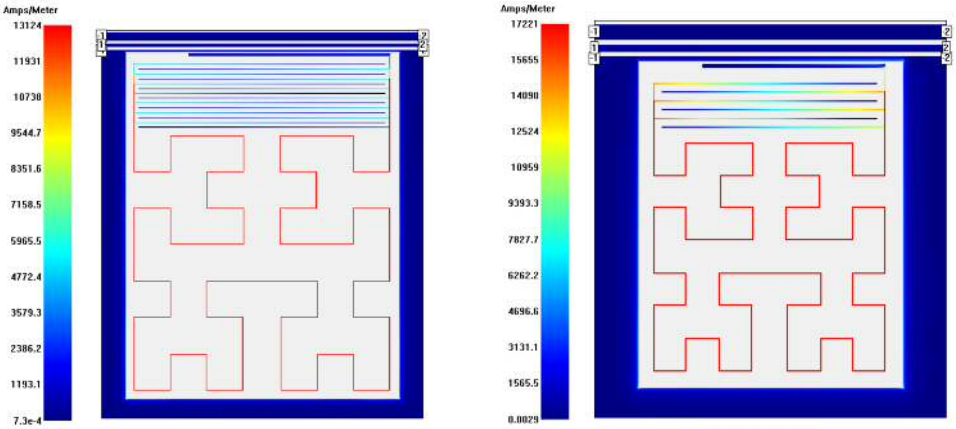

(a) (b)

Figure 6.1: Current distribution in a LEKID on resonance: a) large volume device with uniform current distribution confined to inductive meander and b) small volume device with uniform current distribution in inductive meander but some current leaking into capacitor region.

Partial responses will only occur if the size of the quasiparticle cascade – generated by photon absorption – is smaller than the LEKID geometry. The size of the cascade can be approximated by [58]

$$d = \sqrt{D\tau_{qp}}, \tag{6.1}$$

where D is the diffusion constant of the superconductor. (6.1) gives the average characteristic distance that quasiparticles will diffuse in a time τ_{qp}. For thin-film

Al, with a typical quasiparticle lifetime $\tau_{qp} \sim 200\ \mu$s and $D = 2.25 \times 10^{-3}\ \mathrm{m^2 s^{-1}}$ [85], gives $d \sim 0.7$ mm. (6.1) assumes an unbroken sheet of superconductor, in which the cascade quasiparticles will move randomly in all direction. Therefore the cascade size will be a circle of radius d. In a LEKID, the regions of high current density are meander lines of typical linewidth 4 μm $\ll d$. For the purpose of a first, crude investigation into the position dependence in response, the size of the cascade can be approximated by meander lines of length $2d$. Photon absorption can be crudely simulated in SONNET by creating lines of length $2d \sim 1.4$ mm of higher kinetic inductance than the expected kinetic inductance of the material. An example can be seen in Figure 6.2. The effect of localised photon absorption can then be evaluated by comparing the resonant frequency of the resonator in the two different states: unperturbed and with a local photon hit. The simulations are carried out on the Al resonators.

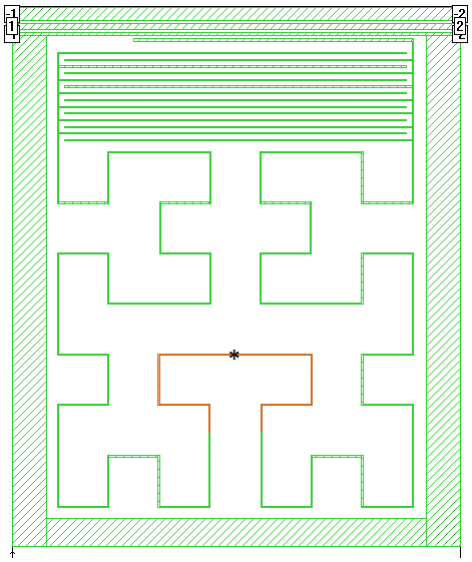

Figure 6.2: SONNET simulation drawing of a LEKID with the quasiparticle cascade region in orange. The location of the photon hit is symbolised by the * symbol.

6.1 Design A: SpaceKID Reference

The largest and smallest volume devices of this design are investigated. The current distribution of the largest volume, $V = 1140\ \mu\text{m}^3$, is shown in Figure 6.1a; the smallest volume, $V = 560\ \mu\text{m}^3$, is shown in Figure 6.1b. A photon absorption event is simulated at different locations along the full meander length: at the centre; roughly mid-distance between the centre and the end; and close to the edge. It is assumed the response is symmetric about the line of symmetry of the meander design. A film thickness of 25 nm is assumed. Table 6.1 shows the relevant location values and Figure 6.3 and Figure 6.5 shows the photon hit location within the meander. Note, to simplify the simulation, quasiparticle diffusion into the capacitor fingers has been ignored. The resonator is simulated with a kinetic inductance $L_k = 1$ pH/sq and the quasiparticle cascade region is simulated with an increased kinetic inductance $L_k = 2$ pH/sq.

Table 6.1: Location of simulated photon absorption events and resulting response; where d_{centre} is the distance from the centre of the meander, $d_{rel} = d_{centre}/l_{tot}$ is the relative distance from the centre, l_{tot} is the total length of the meander, $\Delta f = f_{0,dark} - f_0$ and $f_{0,dark}$ is the resonant frequency under dark conditions.

	$V = 1140\ \mu\text{m}^3$ $l_{tot} = 11392\ \mu\text{m}$ $f_{0,dark} = 1.894$ GHz				$V = 560\ \mu\text{m}^3$ $l_{tot} = 5616\ \mu\text{m}$ $f_{0,dark} = 5.666$ GHz			
	d_{centre} (μm)	d_{rel}	f_0 (GHz)	Δf (GHz)	d_{centre} (μm)	d_{rel}	f_0 (GHz)	Δf (GHz)
centre	0	0	1.867	0.027	0	0	5.496	0.1695
middle	2984	0.262	1.870	0.024	1468	0.261	5.515	0.151
end	5336	0.468	1.876	0.018	2268	0.404	5.550	0.116

6.1.1 Largest Volume

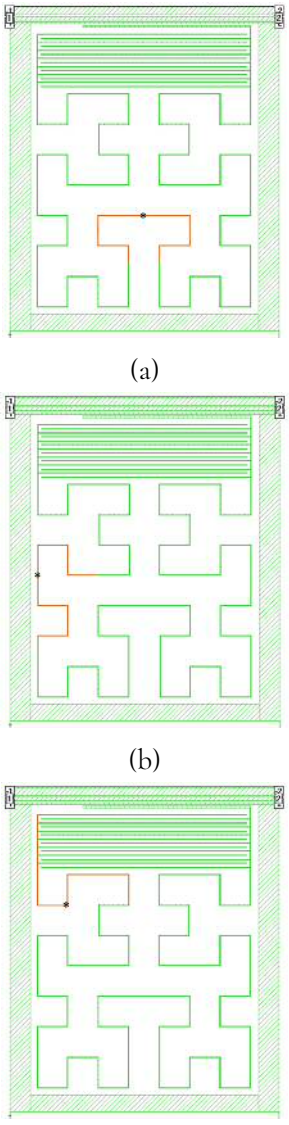

(a)

(b)

(c)

Figure 6.3: SONNET simulation drawing of design A ($V = 1140\mu\text{m}^3$) with different photon absorption locations: a) at the meander centre, b) approximately halfway between the centre and end of the meander and c) close to the end to the meander. The quasiparticle diffusion is shown in orange.

The photon absorption locations that have been simulated for this device can be seen in Figure 6.3. The resulting shift in resonant frequency is shown in Figure 6.4. A very clear dependence on absorption location can be seen. The shift in

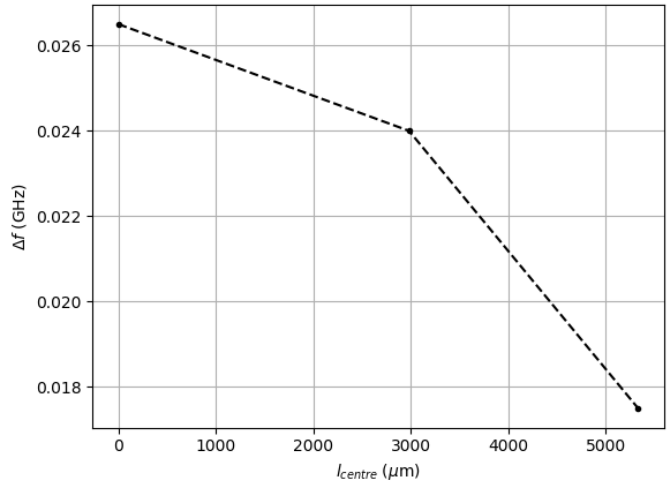

Figure 6.4: Shift in resonant frequency Δf as a function of distance from the meander centre.

resonant frequency is largest when the photon is absorbed at the centre of the meander length, as expected. However, it decreases to $\sim 70\%$ its central value when a photon is absorbed closer to the IDC. This would suggest photons absorbed within the edges of the IDC (where there is some high current density; see Figure 6.1a) are likely to register a measureable response. There is also a chance hits along the capacitor fingers could register a small measurable response., given the size of the cascade.

6.1.2 Smallest Volume

Figure 6.6 also shows a clear local absorption dependence of the detector. Compared to the larger volume detector, a larger response dependence is expected. Looking at Figure 6.1b it is clear the capacitor has some inductive properties with some high current density along the edges and fingers. The response Δf due to the farthest photon hit is $\sim 65\%$ of the central response. This shows a more significant local dependence than the larger volume device. Notice also the farthest

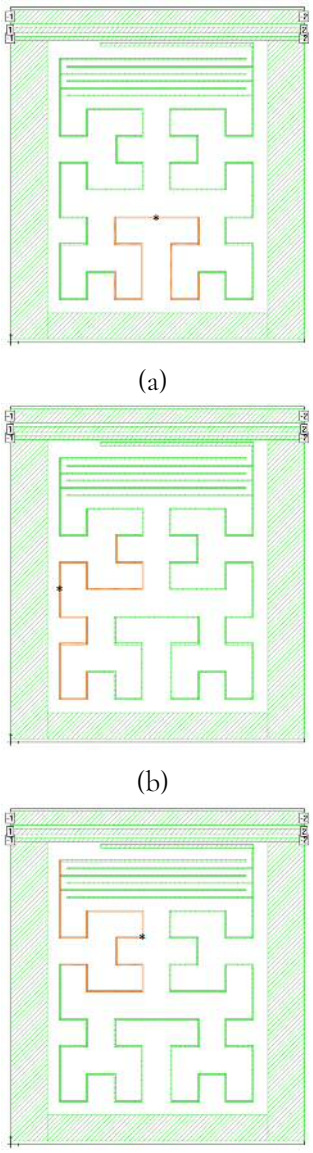

(a)

(b)

(c)

Figure 6.5: SONNET simulation drawing of design A ($V = 560\mu\text{m}^3$) with different photon absorption locations: a) at the meander centre, b) approximately halfway between the centre and end of the meander and c) close to the end to the meander. The quasiparticle diffusion is shown in orange.

photon hit, for this small volume device, is relatively closer to the centre than its counterpart; see Figure 6.5.

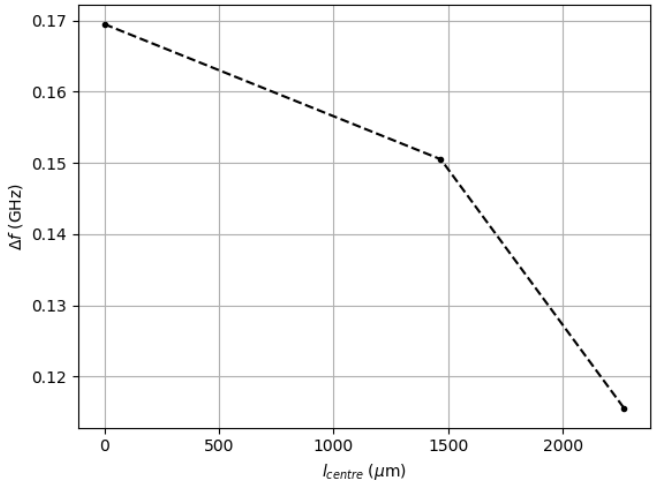

Figure 6.6: Shift in resonant frequency Δf as a function of distance from the meander centre.

6.2 Desgin B: Optimised LEKID

The largest and smallest volume devices of this design are also investigated. The same procedure as for design A has been carried out. Figure 6.7 shows the current distribution in the two devices investigated. The large volume device in Figure 6.7a shows a resonator with reasonably discrete components. However, there are high current density regions along the line features which join the IDC and inductive meander. This may indicate a susceptibility to local dependence. In comparison, the small volume device in Figure 6.7b is definitely expected to have a comparatively large local dependence. There are high current density regions throughout the capacitor.

Table 6.2 shows the relevant location values and Figure 6.8 and Figure 6.10 show the simulated photon absorption locations in the meander.

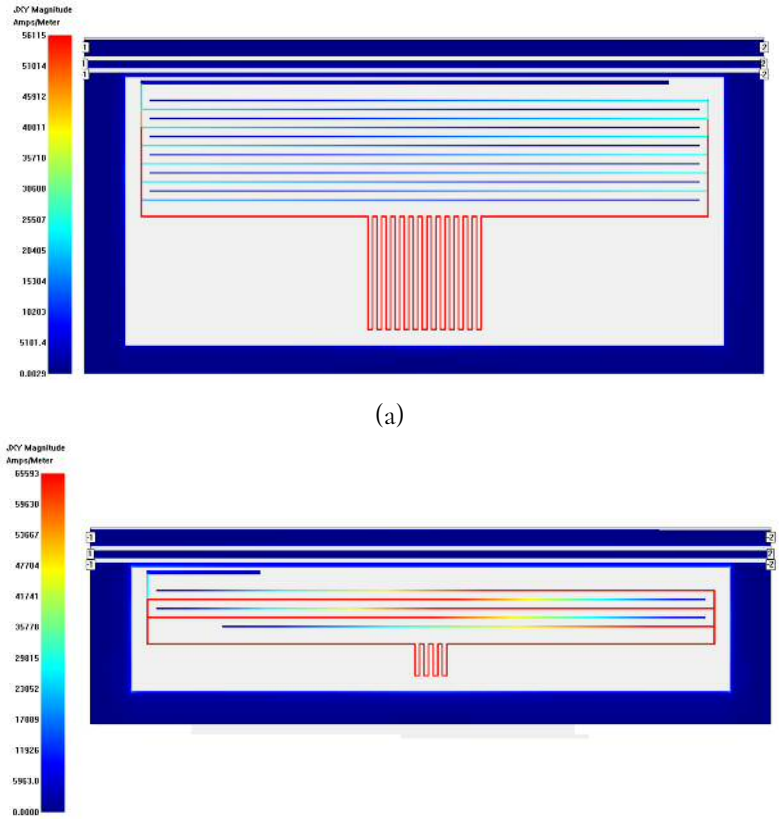

(a)

(b)

Figure 6.7: Current distribution in a LEKID on resonance. a) Large volume design and b) small volume design.

Table 6.2: Location of simulated photon absorption events and resulting response.

	$V = 810\ \mu\text{m}^3$ $l_{tot} = 8104\ \mu\text{m}$ $f_{0,dark} = 2.563$ GHz				$V = 82\ \mu\text{m}^3$ $l_{tot} = 824\ \mu\text{m}$ $f_{0,dark} = 6.848$ GHz			
	d_{centre} (μm)	d_{rel}	f_0 (GHz)	Δf (GHz)	d_{centre} (μm)	d_{rel}	f_0 (GHz)	Δf (GHz)
centre	0	0	2.503	0.060	0	0	6.458	0.3905
middle	3900	0.481	2.506	0.058	388	0.471	6.450	0.398
end	4108	0.507	2.513	0.05	528	0.641	6.482	0.366

6.2.1 Largest Volume

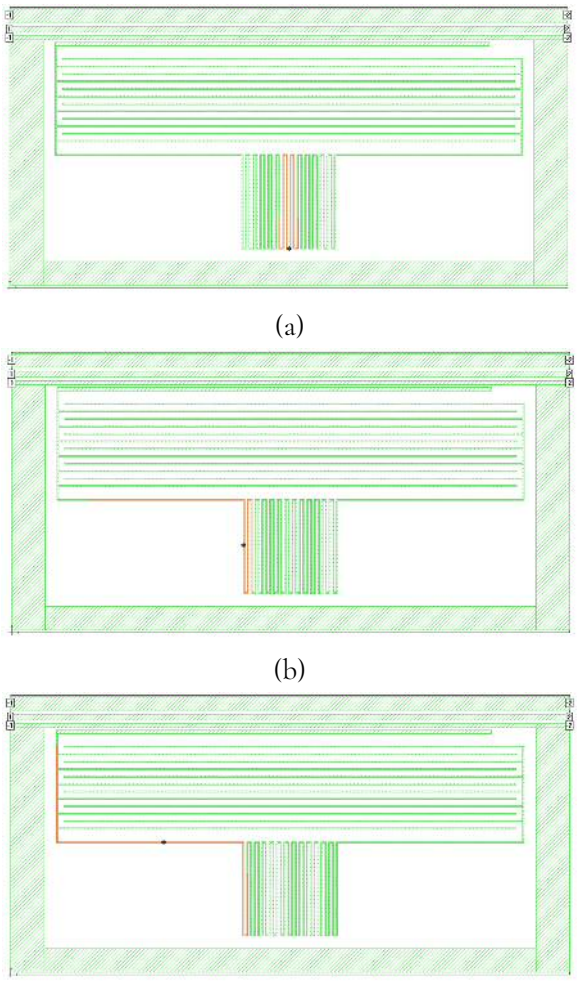

(a)

(b)

(c)

Figure 6.8: SONNET simulation drawing of design A ($V = 810\mu m^3$) with different photon absorption locations: a) at the meander centre, b) approximately halfway between the centre and end of the meander and c) close to the end to the meander. The quasiparticle diffusion is shown in orange.

Figure 6.9 shows some local response dependence. The response to the farthest photon hit is $\sim 85\%$ of the central value. Compared to the largest volume of design A, the local response is less linear. There is, however, a steeper drop in response over a shorter distance: the difference between a hit at the edge of the meander and a hit along the feature line that joins the IDC and meander.

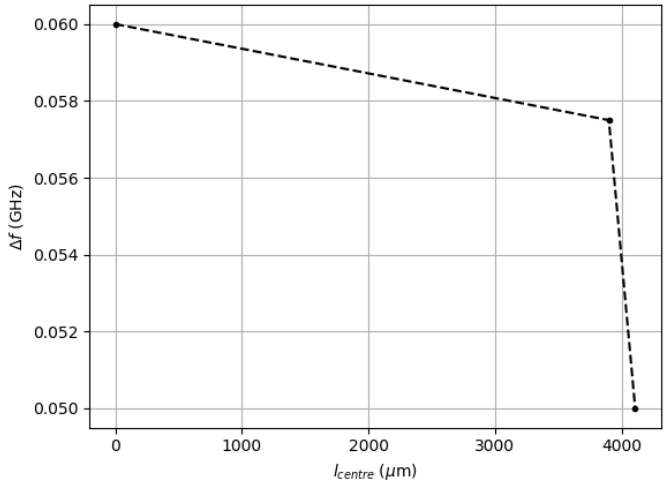

Figure 6.9: Shift in resonant frequency Δf as a function of distance from the meander centre.

Given that a proportionally large response is generated from absorption along the joining line feature, it is possible a hit at the edges of the IDC will also generate a larger than expected response. Though since the trend appears steep, the response could drop off quite rapidly.

6.2.2 Smallest Volume

Figure 6.11 shows a different trend from the other devices investigated. Here, there is a slightly increased response moving further from the centre, before dropping to $\sim 94\%$ of its central response. Looking at Figure 6.10b, the increased response corresponds to photon absorption at the very edge of the meander. The increased response is actually small at $\sim 1\%$ larger than the central response and so may be due to the resolution of the simulation.

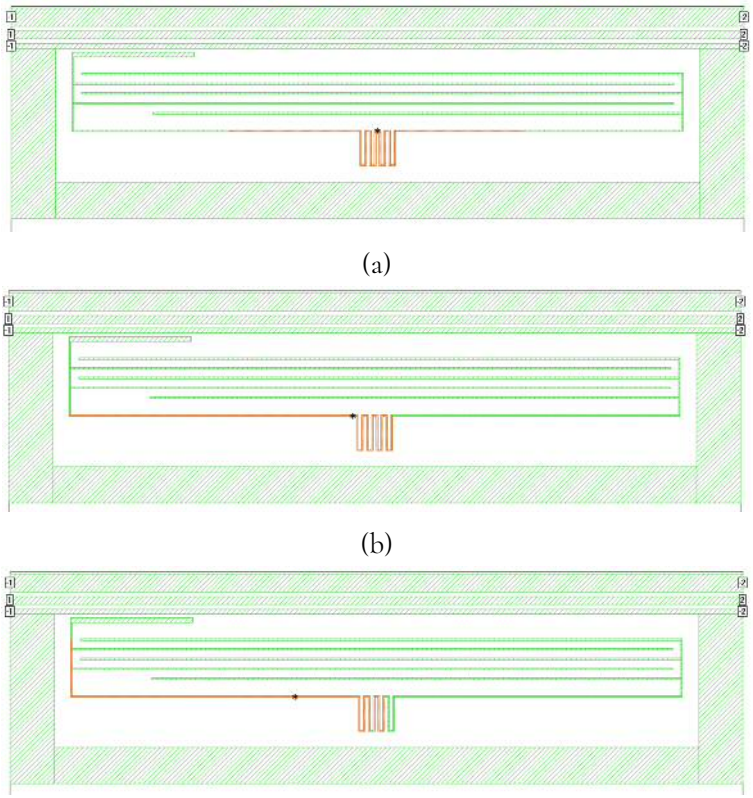

(a)

(b)

(c)

Figure 6.10: SONNET simulation drawing of design A ($V = 82\mu\text{m}^3$) with different photon absorption locations: a) at the meander centre, b) approximately halfway between the centre and end of the meander and c) close to the end to the meander. The quasiparticle diffusion is shown in orange.

6.3 Comparison Between Designs

Figure 6.12 and Figure 6.13 shows the fractional frequency shift of the resonator as a function of the relative distance from the centre of the photon absorption event; where $l_{centre}/l_{tot} = 0$ corresponds to the centre and $l_{centre}/l_{tot} = 0.5$ corresponds to one end of the meander. For data points where $l_{centre}/l_{tot} > 0.5$, the absorption event occurs in the line feature which connects the IDC and meander. This is a consequence of the architecture of design B.

Figure 6.12 shows the difference between the largest volume devices of the two

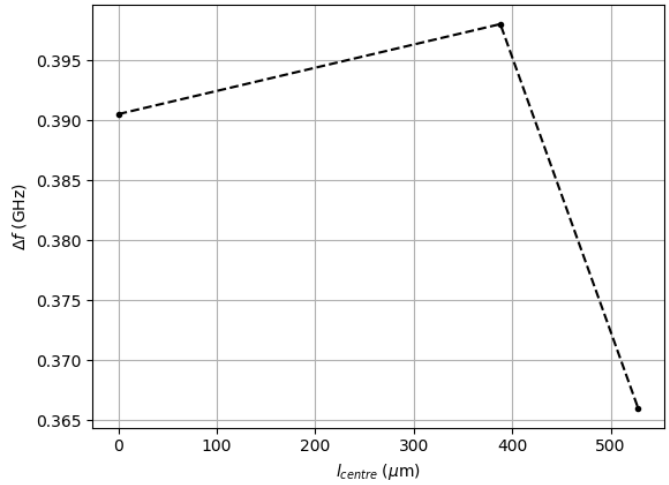

Figure 6.11: Shift in resonant frequency Δf as a function of distance from the meander centre.

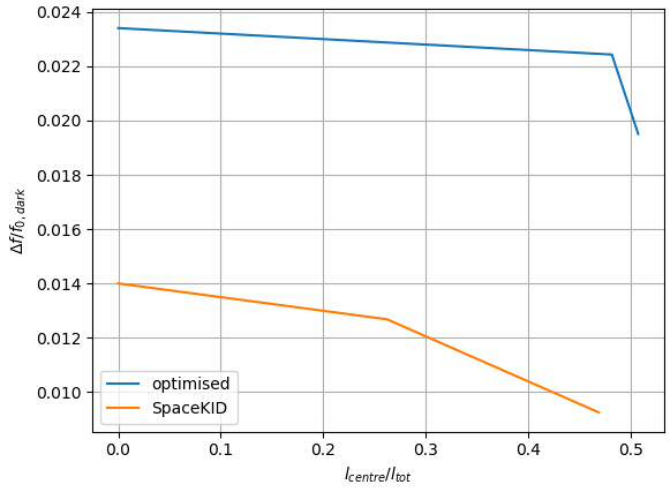

Figure 6.12: Comparison – of the fraction frequency shift $\Delta f / f_{0,dark}$ as a function of relative distance from the meander centre l_{centre}/l_{tot} – between the two large volume designs.

designs. The optimised LEKIDs show a larger response with a higher fractional frequency shift. There is also a smaller variation in the optimised LEKIDs over the same relative distance. This would suggest the optimised LEKIDs have a more uniform current distribution across the meander. However, there is a small but

sharp decrease in response close to the edge of the meander. This is likely due to the joining line feature of the device. The SpaceKID appears to have a nearly linear variation in response, moving away from the centre of the meander; suggesting the current distribution is not uniform. Figure 6.4 shows, more clearly, a nearly 10% drop in response at roughly halfway between the centre and end of the meander. Figure 6.3b shows the cascade is very firmly within the meander boundaries. Towards the end of the meander the response drops by approximately 30%; compared to roughly 15% decrease in response near the meander edge of the design B.

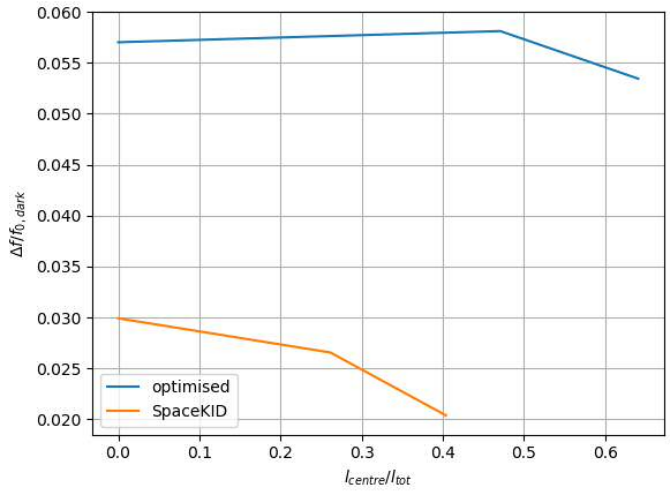

Figure 6.13: Comparison – of the fraction frequency shift $\Delta f/f_{0,dark}$ as a function of relative distance from the meander centre l_{centre}/l_{tot} – between the two small volume designs.

Figure 6.13 shows the difference between the two smallest volume devices of each design type. The optimised LEKID has a higher response with a smaller variation while the SpaceKID has a smaller response with a larger variation. For the SpaceKID device, there is a decrease in response close to the edge of the meander by $\sim 35\%$. This variation is larger than its large volume counterpart. Comparing Figure 6.3c and Figure 6.5c, this larger variation in response is despite the fact the photon absorption event is at a shorter relative distance from the centre. Con-

versely, the optimised design has a smaller variation in the smaller volume device. This will be due to the fact the meander is so small that the cascade diffuses through most of the meander irrespective of the photon hit location.

6.4 Conclusions

Here it is important to remind that the volumes of the devices are not comparable and therefore the magnitude of response is not comparable. It should also be noted that it is unlikely a single photon in the near-infrared or visible range will increase the kinetic inductance of by 1 pH/sq. In fact, a 400 nm photon incident on a typical 25 nm Al film is likely to increase the kinetic inductance by $\sim 10^{-6}$ pH/sq. That said, the value of L_k, and thus the value of the fractional frequency shift, were not important here. This investigation was concerned with the variation in response.

As one would expect, the smallest volume device shows the least variance in response due to the fact the cascade size, estimated by (6.1), is roughly the same size at the meander. However, the variance in these devices come from the line feature which joins the IDC and meander. This is perhaps a design consideration for a future device.

Recall, also, these simulations do not take into account quasiparticle diffusion into the IDC fingers. Since most fingers – in the designs simulated – have low current density, it is likely the response variations would have been larger, if included. Although crude, these simulations have still shown that the current distribution may not be uniform across the entirety of the meander structure. Large variations in response can be expected from all designs in this test array.

Large variations in response will result in a long tail on the lower side of the expected Gaussian absorption distribution. This ultimately broadens the Gaussian

and thus limits the energy resolution. This behaviour is observed in the results presented in the following chapter.

Chapter 7

Measurement of Single-Photon Test Array

In this chapter, the results from optical measurement of the single-photon LEKID test array are presented. The test set-up was modified to accommodate multiple optical sources; this is describe below. The resonator identification process is described in some detail. It was not possible to reliably identify the Al and hybrid resonators however, single-photon detection in many of the resonators is verified.

7.1 Experimental Set-up

7.1.1 Readout Electronics

The resonant frequencies of this test device span a large range: $\sim$ 1 GHz < f_0 < $\sim$ 8 GHz. Therefore, two different IQ mixers were used. For resonators with f_0 < 4.5 GHz, the readout electronics set-up described in Section 4.1.1 remains unchanged. While for resonators with f_0 > 4.5 GHz the IQ mixer is replaced with a Marki

IQ-4509LXP passive mixer which requires a LO input power of +11 dBm.

7.1.2 Optical Set-up

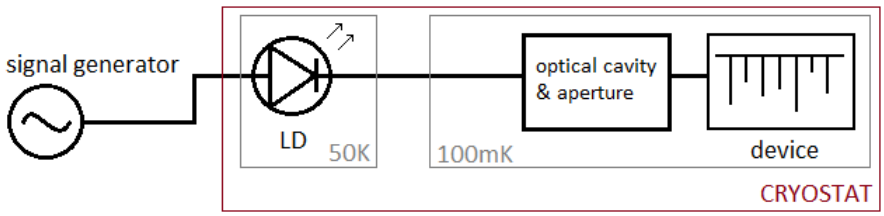

Figure 7.1: Schematic of the optical set-up for each laser diode.

The optical set-up for this set of measurements has been changed from that described in Section 4.1.2. The new set-up is shown in Figure 7.1. There are four laser diodes (LDs) mounted on the 50 K stage spanning through the optical and into the near-infrared regime: 405 nm, 670 nm, 780 nm and 1550 nm. A signal generator is used to control the LD source; using square-wave or DC power modes. Note that only one LD can be powered at any one time. Output from the diodes are carried via single-mode fibre optic cables. Each diode is contained in an aluminium housing – shown in Figure 7.2 and Figure 7.4a – which has a FC/PC fibre optic bulkhead mounted to its front. The housing design ensures the diode sits in line with the bulkhead's centre, and thus fibre head, once it is connected. The housing is also designed so that internal reflections maximises coupling into the fibres. Note that each diode has its own fibre due to constraints of the fibres' operating wavelengths; all fibres have a 125 μm core. The fibres are run through to the ultra-cold (UC) plate, thermalised at each stage of the cryostat, where they are connected to FC/PC bulkheads mounted on the optical cavity. The external fibre insulation has been stripped away to aid thermalisation.

The optical cavity has a central cylindrical cavity of 30 mm diameter and 12

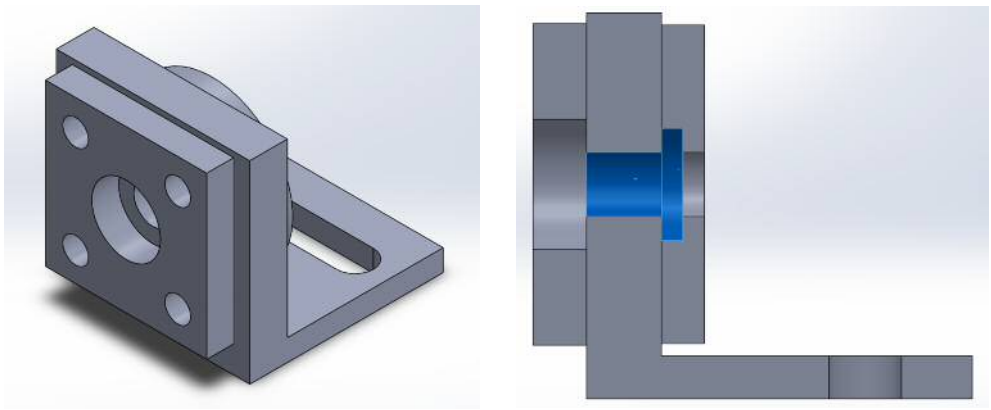

(a) (b)

Figure 7.2: a) CAD drawing of diode housing and b) its cross-section. Highlighted in blue is where the laser diode sits.

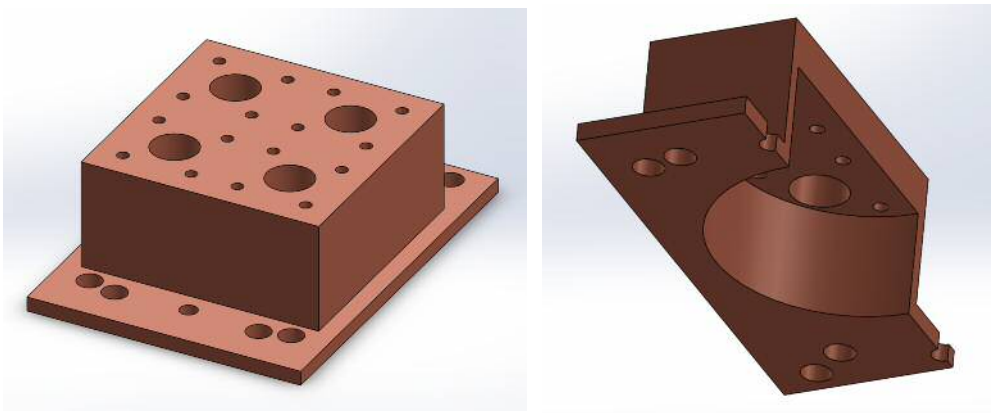

(a) (b)

Figure 7.3: a) CAD drawing of optical cavity and b) its cross-section shown from the underside.

mm depth. It is mounted directly onto the test array with an aperture plate. Light from the four fibres are fed directly to the cavity where it scatters before exiting through a 1 mm diameter aperture at the centre of the plate. The aperture hole lies at the centre of the test array. Note this is not an integrating cavity and thus a uniform optical distribution is not expected. The cavity is used to allow light at all wavelengths to illuminate the chip in the same way. The optical cavity-test array interface can be seen in Figure 7.4b.

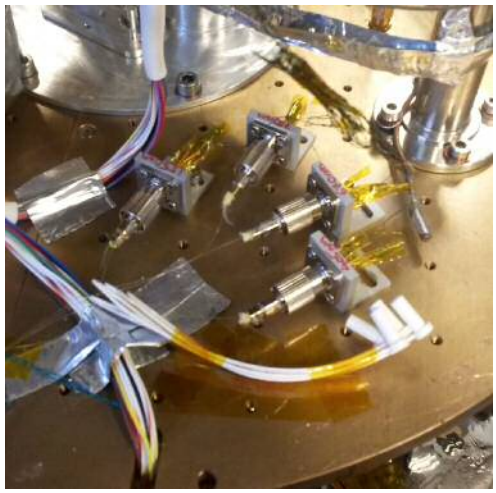

(a)

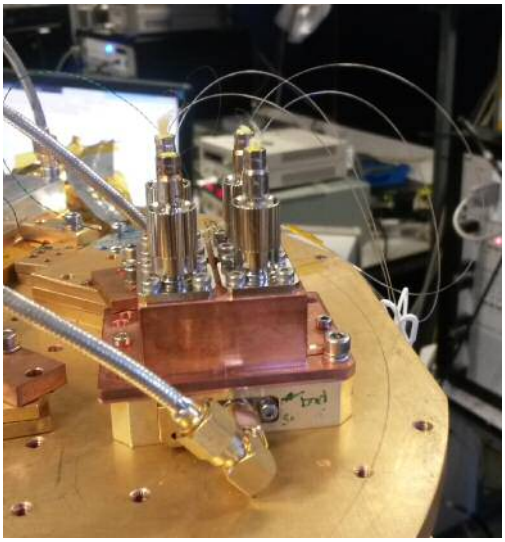

(b)

Figure 7.4: a) Image of diodes at 50 K stage and b) image of the optical cavity and test array interface.

7.2 Resonator Identification

Variations in film properties and thickness, as well as processing errors, typically lead to scatter in the resonant frequencies from that of the designed values. This is observed for the LEKID test array; all 18 resonators had been found but their arrangement did not match expectation. A VNA sweep of the individual tones is

shown in Figure 7.5 and compared with the designed f_0 distribution.

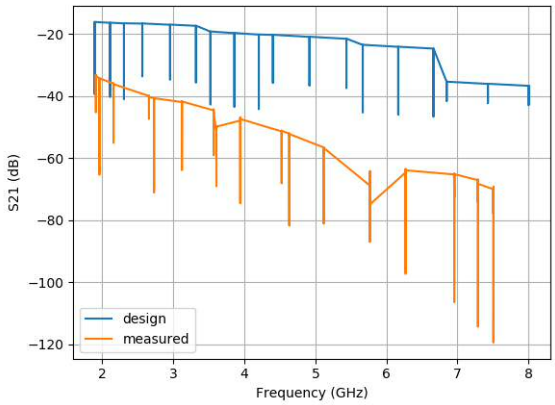

Figure 7.5: Designed (blue) and measured (orange) S_{21} amplitude showing resonator placement in the frequency domain; with -110 dBm microwave power at chip. Note an arbitrary +20 dB offset to the S_{21} level of the designed frequencies has been applied to aid visual comparison.

By visual inspection, it is unclear which resonator is assigned to which design. The frequency range is roughly the same, so there is no reason to expect the set of triplets to appear in a different order. Though there is some unexpected bunching of detectors which suggests some of the sets of triplets are overlapping. It was therefore necessary to identify the resonators though process of elimination.

7.2.1 NbAl Elimination

As previously mentioned, thin-film bi-layers are expected to proximitise. Therefore, the NbAl devices are expected to behave more closely to Nb devices. These can be easily identified as the resonators which remain once the bath temperature rises above the critical temperature of the 25nm Al film: 1.417 K. They can also be identified through increasing microwave power. The Al and hybrid devices should become over-driven – if not driven completely normal – at very high microwave powers. Whereas, the NbAl devices will remain largely unchanged due to

the higher energy required to drive the material normal. As it was not convenient to make measurements at elevated temperatures > 1 K, the NbAl devices were identified by increasing the microwave power incident on the array.

Figure 7.6 shows the NbAl resonators, in red, which remain even when probed with high microwave power. All other resonators are severely over-driven or have been driven normal at -70 dBm.

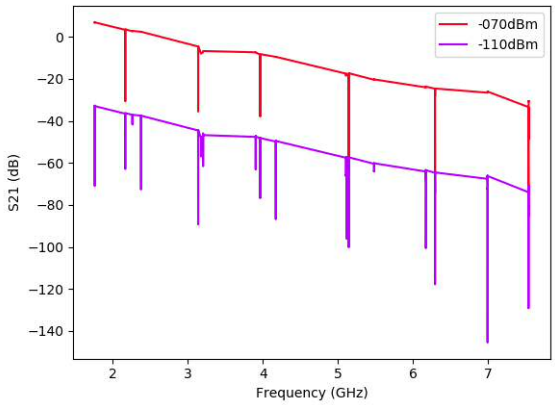

Figure 7.6: VNA sweep of all resonators with different microwave powers.

7.2.2 Al-NbAl Hybrid Elimination

Recall (3.2) which shows that df_0/dT depends on a change in the total internal inductance dL_{tot}. For an Al and hybrid pair, the geometric inductance remains unchanged since the design is the same. Therefore df_0/dT depends on dL_k. Since the hybrid devices are expected to have a lower kinetic inductance than the Al devices, it can be expected that hybrids will have a smaller comparative response to changes in temperature.

The device responsivity can be depicted by its fractional frequency shift as a function of bath temperature. With the NbAl resonators identified and excluded, and assuming the order of the sets of triplets remain unchanged, the responsivity

of the remaining adjacent resonators can be compared.

The measured resonators shown in Figure 7.5 are labelled in order of appearance; with K001 having the lowest f_0 and K018 having the highest. A table showing the resonators and assumed device design can be seen in Table 7.1. The fractional frequency shift comparison of the assumed Al and hybrid pairs are shown in Figure 7.7.

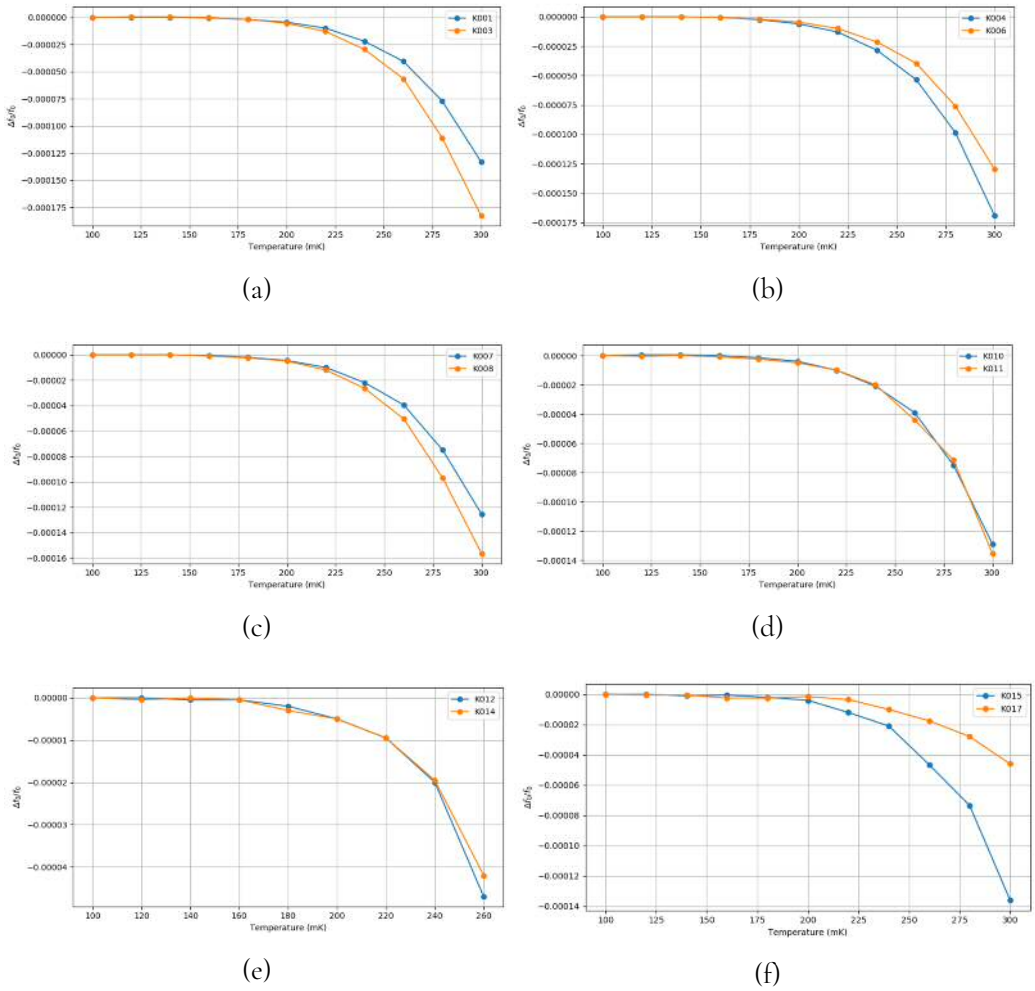

Figure 7.7: Fractional frequency shift comparison between assumed Al and hybrid pairs, as a function of temperature. The lower frequency resonator is shown in blue. Note data in e) goes up to 260 mK due to data corruption at higher temperatures.

In Figure 7.7 plots d) and e) show too little a difference to suggest which mater-

ial each resonator is composed of. These resonator pairs have been left unidentified. The remaining - plots a), b), c) and f) - show some visible difference between the detector responsivity. The hybrid devices are taken to be the resonators with the shallowest response at high temperatures. The resulting identification of the resonators can be seen in Table 7.1 and Figure 7.8.

Table 7.1: Resonator design parameters. The LEKID numbers are labelled in order of resonance frequency to match the dataset labelling system. Details on the design set and type can be found in Chapter 5. Colour-coding of material types matches Figure 7.8. Resonators highlighted in red are unidentified and appear in ascending frequency order.

LEKID	Design set	Design	Material	V (μm^3)	$f_{0,des}$ (GHz)	$f_{0,meas}$ (GHz)
K003			Al		1.893	2.263
K001	I	A	hybrid	1139.2	2.110	1.762
K002			NbAl		2.305	2.170
K004			Al		2.563	2.378
K006	II	B	hybrid	810.4	2.954	3.176
K005			NbAl		3.318	3.139
K008			Al		3.522	3.905
K007	III	A	hybrid	761.2	3.859	3.205
K009			NbAl		4.203	3.965
K010			Al		4.401	4.173
K011	IV	B	hybrid	388	4.916	5.107
K012			NbAl		5.436	5.144
K013			Al		5.666	5.117
K014	V	A	hybrid	561.4	6.166	5.480
K016			NbAl		6.662	6.291
K015			Al		6.848	6.169
K017	VI	B	hybrid	82.4	7.428	6.990
K018			NbAl		8.002	7.536

It can be seen more clearly in Figure 7.8 that the triplet sets have overlapped. The ordering within the triplet sets also appear to be scrambled from set to set. Figure 7.9 shows the disparity between the measured and designed frequencies for the assumed resonator identities. The unidentified resonators are not included. The plot shows a very clear trend for the NbAl resonators. This would suggest the res-

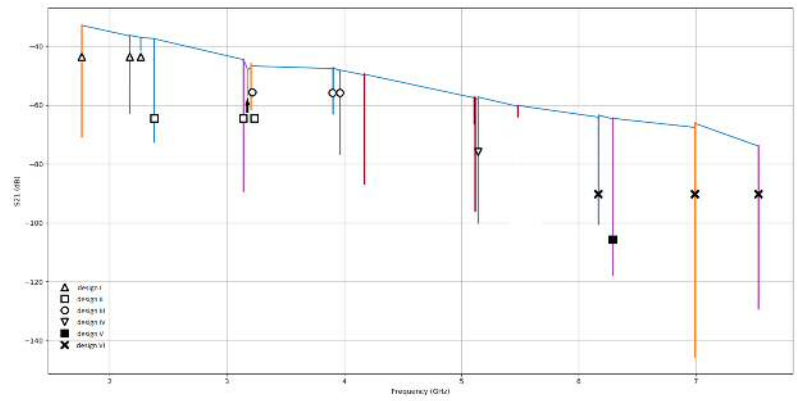

Figure 7.8: Plot showing assumed resonator identity: Al (blue), hybrid (orange) and NbAl (purple) resonator; triplets are identified with a key. The unidentified resonators are shown in red.

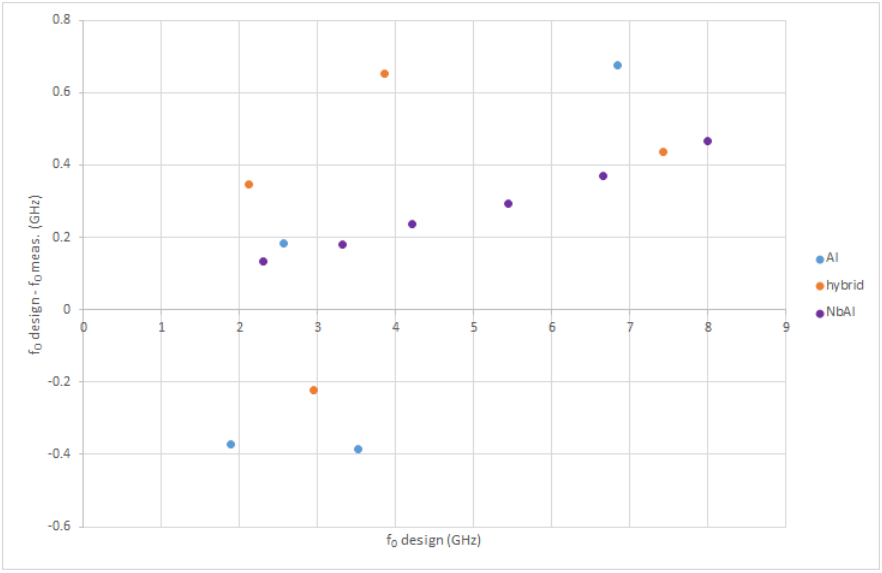

Figure 7.9: Plot showing the disparity between the measured and design f0 values as a function of designed f_0. Positive disparity represents a decrease from the expected f_0 and a negative disparity represents an increase. Unidentified resonators are not shown.

onators have been correctly identified. The method for eliminating the NbAl resonators is also fool-proof. Though the frequency dependence hints that the wrong kinetic inductance was used for the simulations.

The Al and hybrid data points show very clearly there can be no confidence in the identification between these resonator pairs. The large scatter suggests the pairs may no longer be in frequency order either. It is possible this scatter may be due to the processing of the array. Recall Section 5.6; any NbAl features are patterned and lithographed. This is the first step after material deposition. Whereas, for any Al features, the Nb layer on top is etched away. The fact that the identified NbAl resonators show a clear trend suggests that this etching process could be the cause of the scatter. However, without clear identification of the resonators, this is only speculation at this stage.

7.3 Material Properties

7.3.1 Critical Temperature & Normal Resistivity

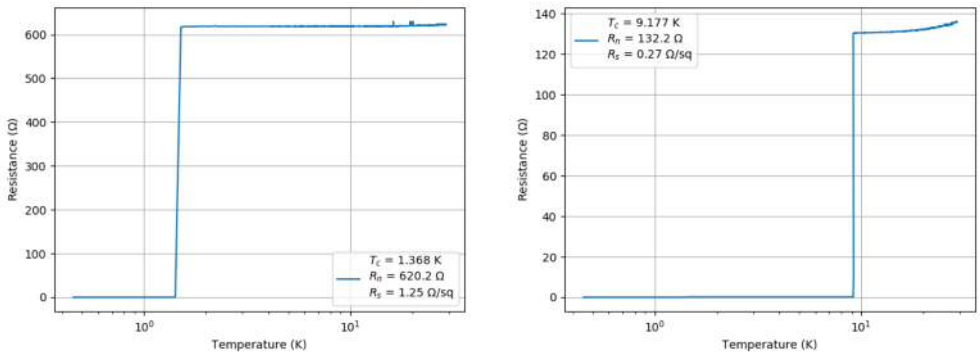

(a) (b)

Figure 7.10: Measured resistance of DC test structure as a function of temperature. The test structure has 498 squares. a) Al b) NbAl.

The critical temperature and sheet resistance are measured by monitoring the resistance of the DC test structures, shown in Figure 5.5, as the test system is cooled down to base temperature. The measurements are shown in Figure 7.10. The nor-

mal resistance is required to obtain a value for the normal conductivity of the material. The critical temperature is taken as the median temperature of the two data points about the resistance drop-off. From these measurements, the kinetic inductance has been calculated using (2.14) and (2.24): $L_{k,Al} \sim 1.3$ pH/sq and $L_{k,NbAl} \sim 0.03$ pH/sq.

7.3.2 Quasiparticle Lifetime

The complexity of the test chip and the likely mis-identification of resonators means the quasiparticle lifetime of each resonator must be measured. A robust set of square-wave measurements, as described in Section 4.2.3.1, were made for each resonator. The resulting extraction of $\tau_{qp}(T)$ for many resonators does not appear as expected. There is a question on the reliability of the measurements, so further analysis on the detectors relies upon the lifetime extracted from the averaged and stacked detections; as performed in Section 4.3 Figure 4.19. These values can be seen in Table 7.2. Some scatter can be seen across the array but without identification of the resonators it is difficult to see any trend. It should also be noted that these values are low for Al measured at 100 mK; even with the quasiparticle lifetime saturation. This could be a result of the fabrication process.

7.4 Single-Photon Detection

Despite not having full confidence in the identification of the Al and hybrid devices, optical measurements have shown clear single-photon detection. These results are presented here. The same optical measurements described in Chapter 4 were taken for every Al and hybrid resonator; at every available laser diode wavelength.

Table 7.2: Quasiparticle lifetime extracted from single-photon detections; for the Al and hybrid devices.

LEKID	τ_{qp} (ms)
K001	0.13
K003	0.05
K004	0.12
K006	0.12
K007	0.10
K008	0.13
K010	0.19
K011	0.15
K012	0.13
K014	0.10
K015	0.12
K017	0.10

7.4.1 Detection Extraction Method

A modified approach based on the method for extracting detections described in Chapter 4 has been employed here. The time-stream data is low-pass filtered with a bandwidth of 2 kHz. An example of the raw and filtered time-stream can be seen in Figure 7.11a. In Figure 7.11b the expected impulse response is based on(3.11). The time-stream is convolved with the impulse response function. The same filtering is applied to the expected response and is then match-filtered to the filtered time-stream. Note that the match filter was selected to be up to the point where the filtered impulse response is at 80% of the maximum. This is depicted as the green line in Figure 7.11b. This was done because each resonator had a slightly different time-constant. This increased the effective integration to $\sim 1.8\tau_{qp}$. The matched filtered responses are then converted to an equivalent unfiltered response to find the unfiltered response amplitude. This method has been applied to both the illuminated and dark detector.

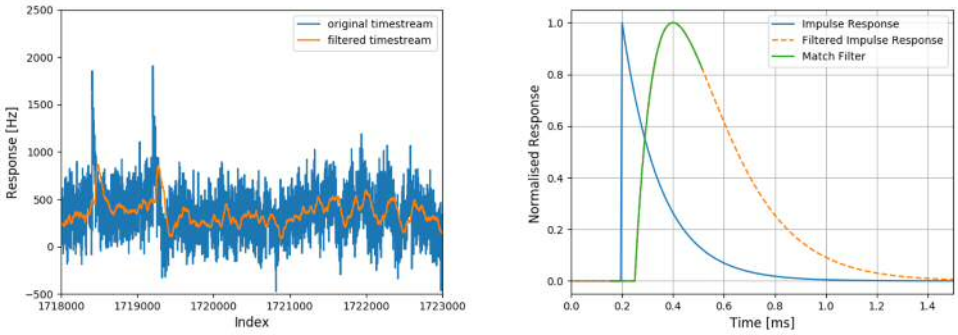

(a) (b)

Figure 7.11: a) Raw (blue) and filtered (orange) time-stream. b) Example of match filtering process.

7.4.2 Extracted Detections

The resulting detection extractions for each detector – at each wavelength – can be seen in this section; including examples of the raw measurement data with suspected responses to absoprtion events. Extractions from the illuminated detector are shown by the black line and dark extractions are shown by the orange line. The dark extractions are subtracted from the illuminated extractions (with a coefficient of 1) to show the difference; this is shown by the blue line. A Gaussian distribution is fitted to the blue lined data to extract values for the peak amplitude and the FWHM. A summary of these values can be seen in Table 7.3 and 7.4. Single-photon detection in each device is evident if the following is observed:

1. Dark detections (LED off) show an equal number of positive and negative detector responses; as expected from noise in a detector.

2. Dark detections measure the same amplitude shift in f_0 in both the positive and negative directions.

3. The number of positive detections increases under illumination.

4. Subtraction of the dark counts from the illuminated counts leaves a clear positive residual excess with negligible negative counts.

Table 7.3: Table of extracted peak amplitude values from the Gaussian fitting. Resonators in bold are use for further analysis in Section 7.4.3.

	Peak Amplitude (Hz)			
λ (nm)	1550	780	670	405
K001	115 ± 1	123 ± 1	118 ± 2	122 ± 7
K003	543 ± 9	559 ± 4	565 ± 22	571 ± 36
K004	158 ± 1	178 ± 1	191 ± 1	272 ± 2
K006	427 ± 3	462 ± 4	469 ± 3	608 ± 9
K007	312 ± 2	340 ± 3	360 ± 2	498 ± 3
K008	634 ± 10	750 ± 8	812 ± 6	1167 ± 23
K010	531 ± 7	669 ± 5	738 ± 3	1186 ± 10
K011	879 ± 6	994 ± 7	1037 ± 5	1396 ± 8
K012	745 ± 7	907 ± 7	1020 ± 6	1522 ± 24
K014	1726 ± 21	2483 ± 15	3019 ± 33	4193 ± 155
K015	-	2041 ± 23	1986 ± 22	2433 ± 120
K017	2580 ± 39	2762 ± 27	2620 ± 58	3439 ± 199

Table 7.4: Table of extracted FWHM values from the Gaussian fitting. Resonators in bold are use for further analysis in Section 7.4.3.

	FWHM (Hz)			
λ (nm)	1550	780	670	405
K001	63 ± 3	66 ± 3	76 ± 4	89 ± 12
K003	236 ± 22	259 ± 10	264 ± 53	191 ± 84
K004	85 ± 3	78 ± 2	81 ± 3	92 ± 5
K006	220 ± 8	265 ± 10	240 ± 7	285 ± 22
K007	158 ± 6	162 ± 7	159 ± 5	211 ± 7
K008	297 ± 23	343 ± 19	374 ± 15	468 ± 53
K010	262 ± 15	323 ± 13	361 ± 8	519 ± 26
K011	425 ± 15	532 ± 18	597 ± 13	753 ± 21
K012	476 ± 19	532 ± 17	597 ± 15	1018 ± 63
K014	878 ± 46	1058 ± 42	1490 ± 87	2833 ± 406
K015	-	1124 ± 68	1068 ± 52	1335 ± 284
K017	1244 ± 92	1422 ± 63	1213 ± 83	1845 ± 429

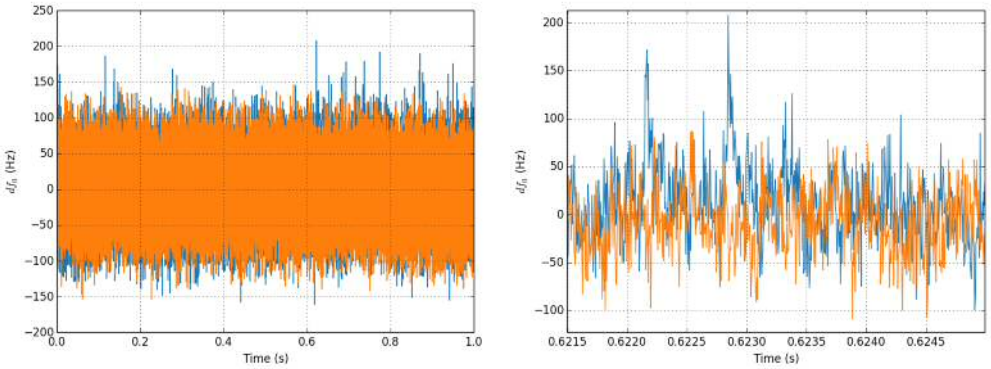

(a) (b)

Figure 7.12: Example time-stream capture with 405 nm LD on (blue) and off (orange) of resonator K001: a) full 1 s time-stream and b) zoomed version showing two absorption event responses.

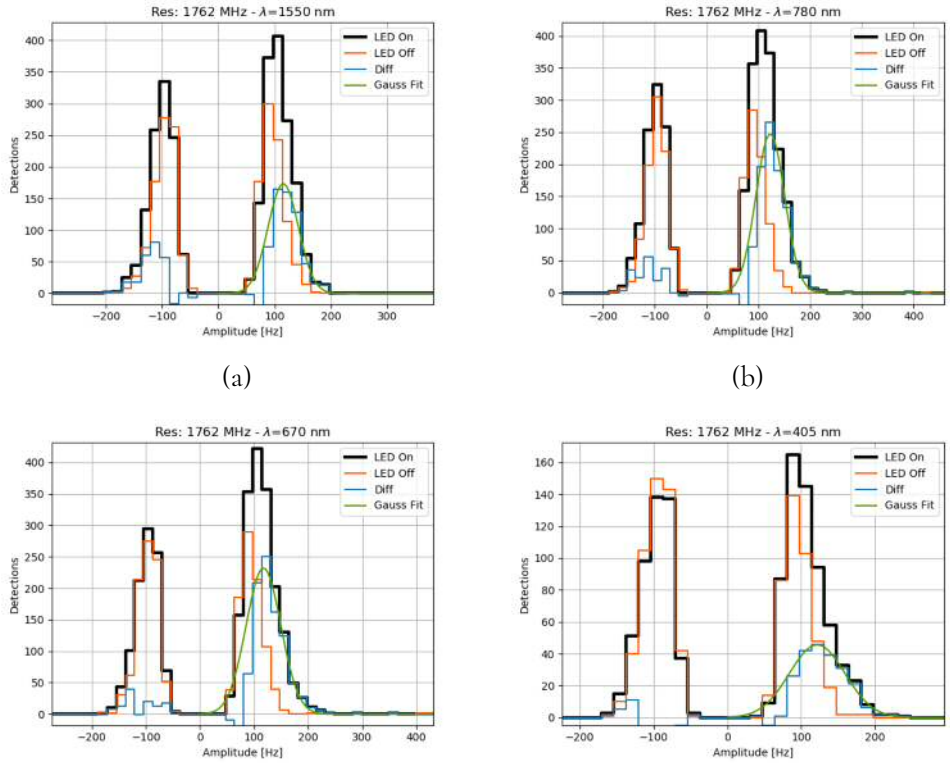

(a) (b)

(c) (d)

Figure 7.13: Extracted single-photon detections in resonator K001 with a) 1550 nm, b) 780 nm, c) 670 nm and d) 405 nm wavelengths.

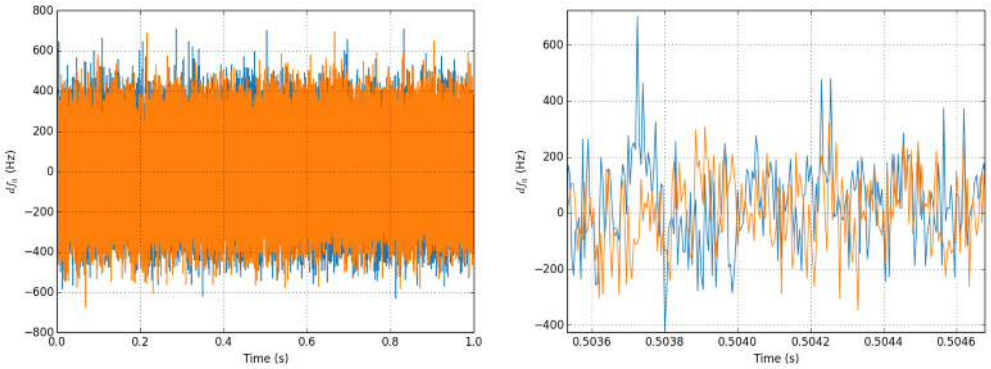

(a) (b)

Figure 7.14: Example time-stream capture with 670 nm LD on (blue) and off (orange) of resonator K003: a) full 1 s time-stream and b) zoomed version showing two absorption event responses.

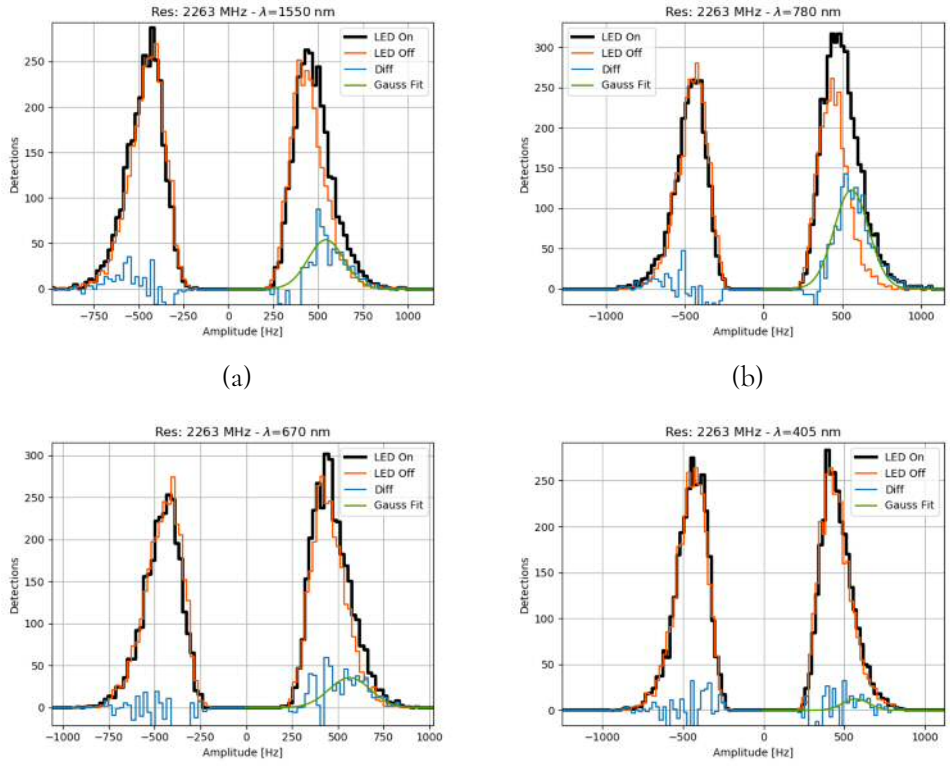

(a) (b)

(c) (d)

Figure 7.15: Extracted single-photon detections in resonator K003 with a) 1550 nm, b) 780 nm, c) 670 nm and d) 405 nm wavelengths.

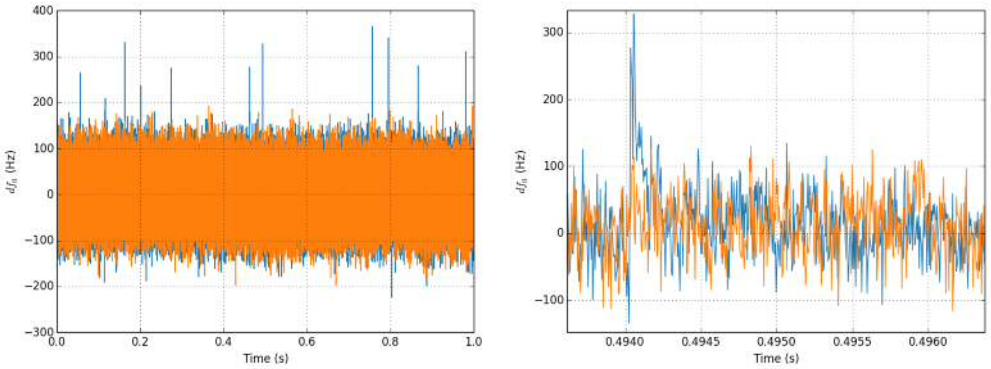

(a) (b)

Figure 7.16: Example time-stream capture with 405 nm LD on (blue) and off (orange) of resonator K004: a) full 1 s time-stream and b) zoomed version showing two absorption event responses.

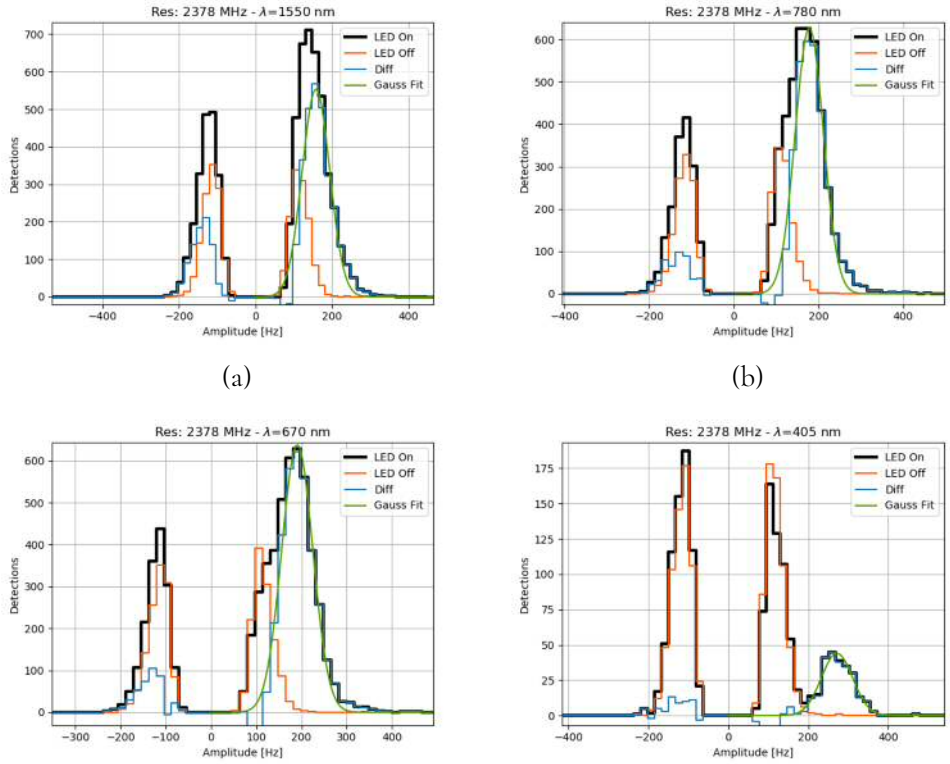

(a) (b)

(c) (d)

Figure 7.17: Extracted single-photon detections in resonator K004 with a) 1550 nm, b) 780 nm, c) 670 nm and d) 405 nm wavelengths.

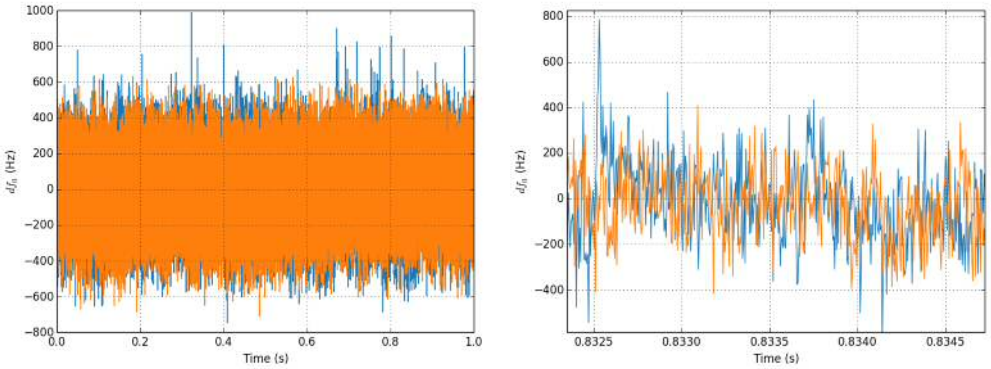

(a) (b)

Figure 7.18: Example time-stream capture with 405 nm LD on (blue) and off (orange) of resonator K006: a) full 1 s time-stream and b) zoomed version showing two absorption event responses.

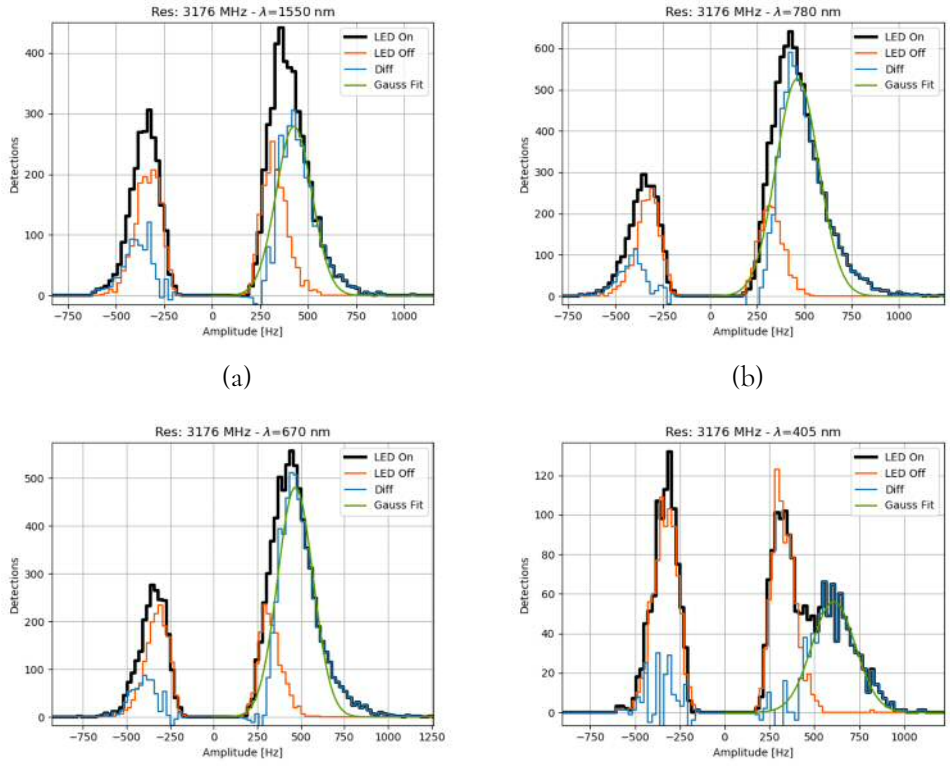

(a) (b)

(c) (d)

Figure 7.19: Extracted single-photon detections in resonator K006 with a) 1550 nm, b) 780 nm, c) 670 nm and d) 405 nm wavelengths.

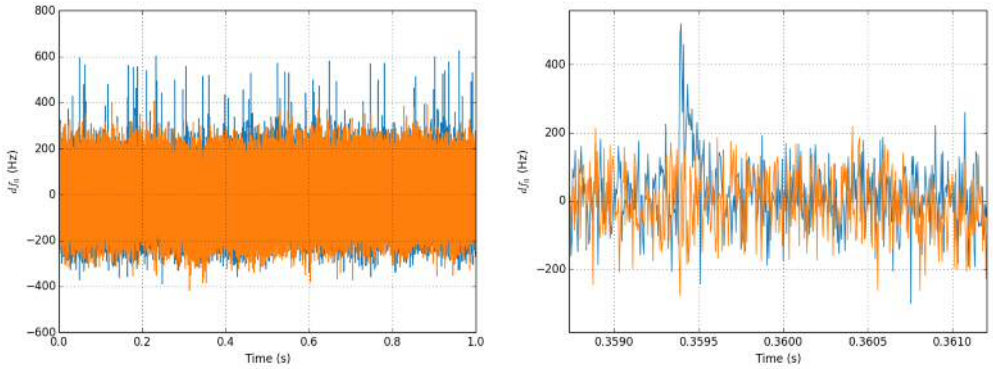

(a) (b)

Figure 7.20: Example time-stream capture with 405 nm LD on (blue) and off (orange) of resonator K007: a) full 1 s time-stream and b) zoomed version showing two absorption event responses.

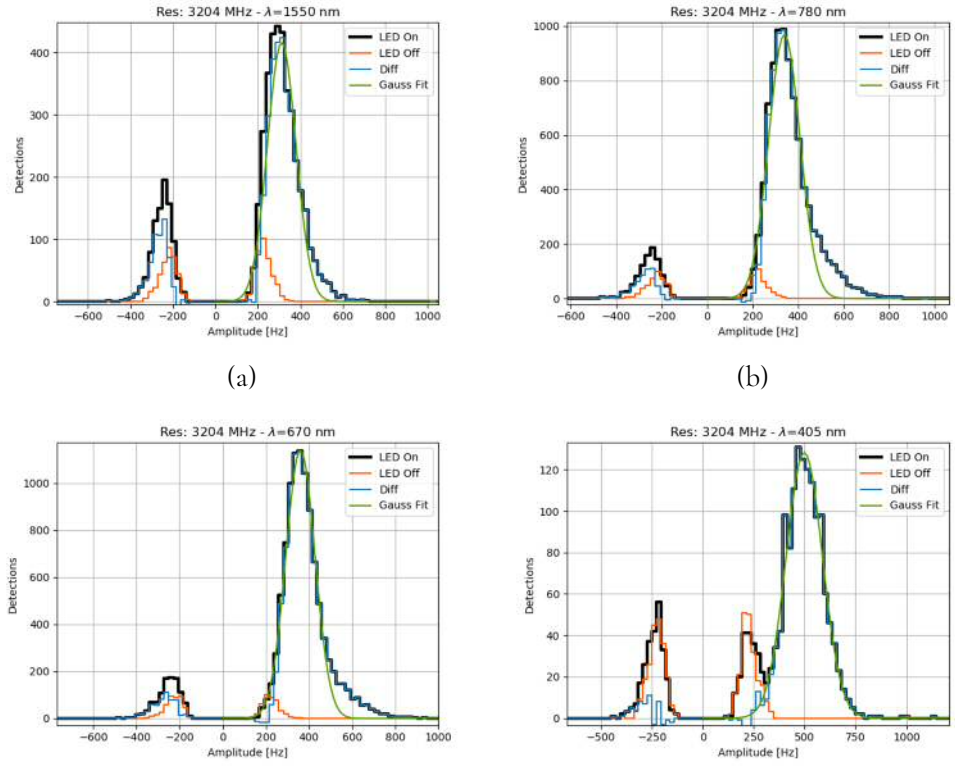

(a) (b)

(c) (d)

Figure 7.21: Extracted single-photon detections in resonator K007 with a) 1550 nm, b) 780 nm, c) 670 nm and d) 405 nm wavelengths.

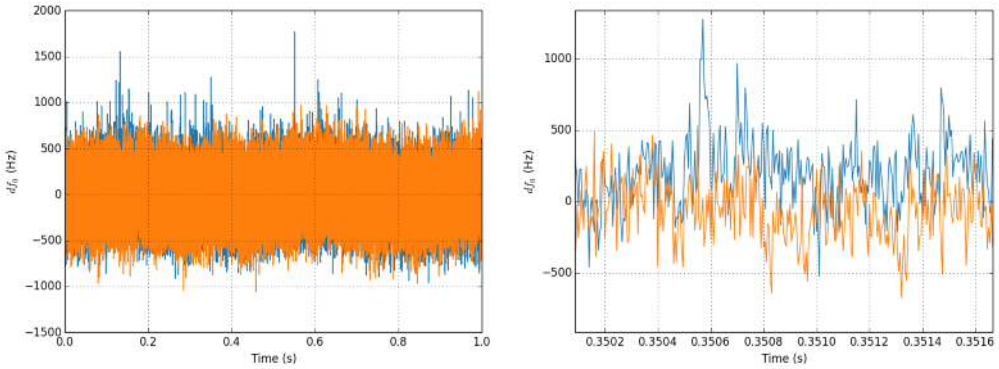

(a) (b)

Figure 7.22: Example time-stream capture with 670 nm LD on (blue) and off (orange) of resonator K008: a) full 1 s time-stream and b) zoomed version showing two absorption event responses.

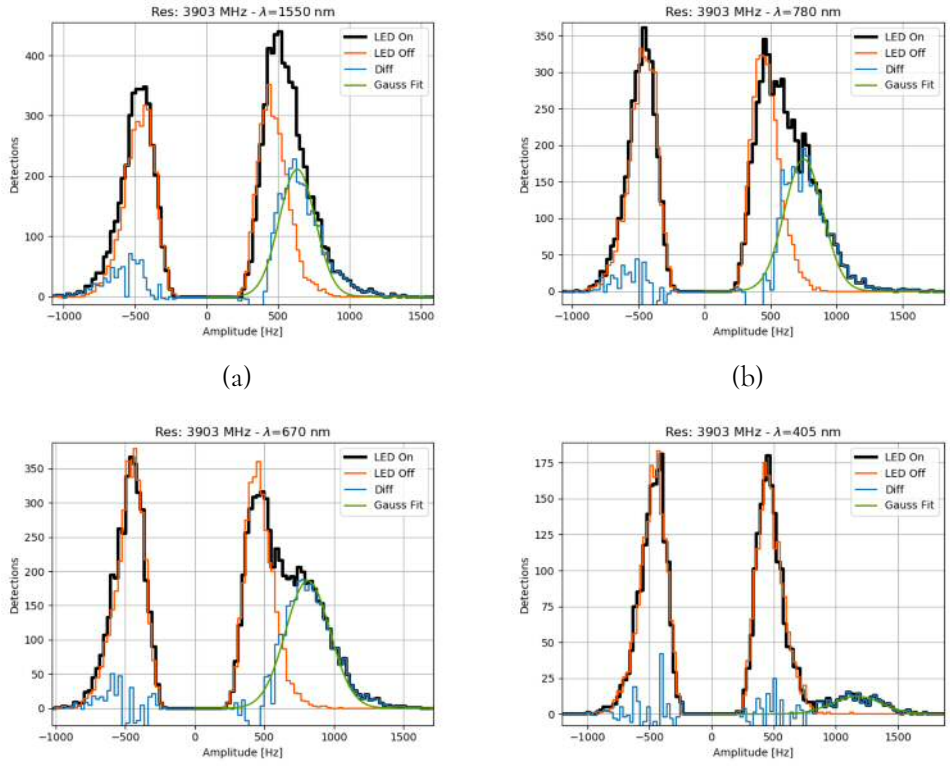

(a) (b)

(c) (d)

Figure 7.23: Extracted single-photon detections in resonator K008 with a) 1550 nm, b) 780 nm, c) 670 nm and d) 405 nm wavelengths.

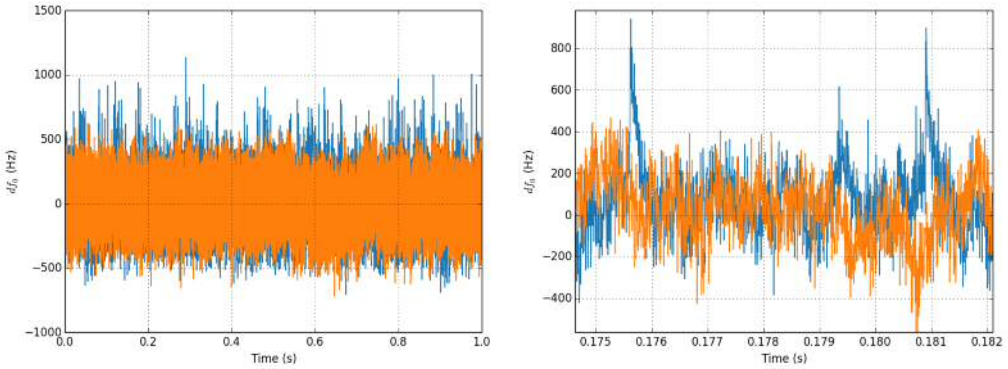

(a) (b)

Figure 7.24: Example time-stream capture with 670 nm LD on (blue) and off (orange) of resonator K010: a) full 1 s time-stream and b) zoomed version showing two absorption event responses.

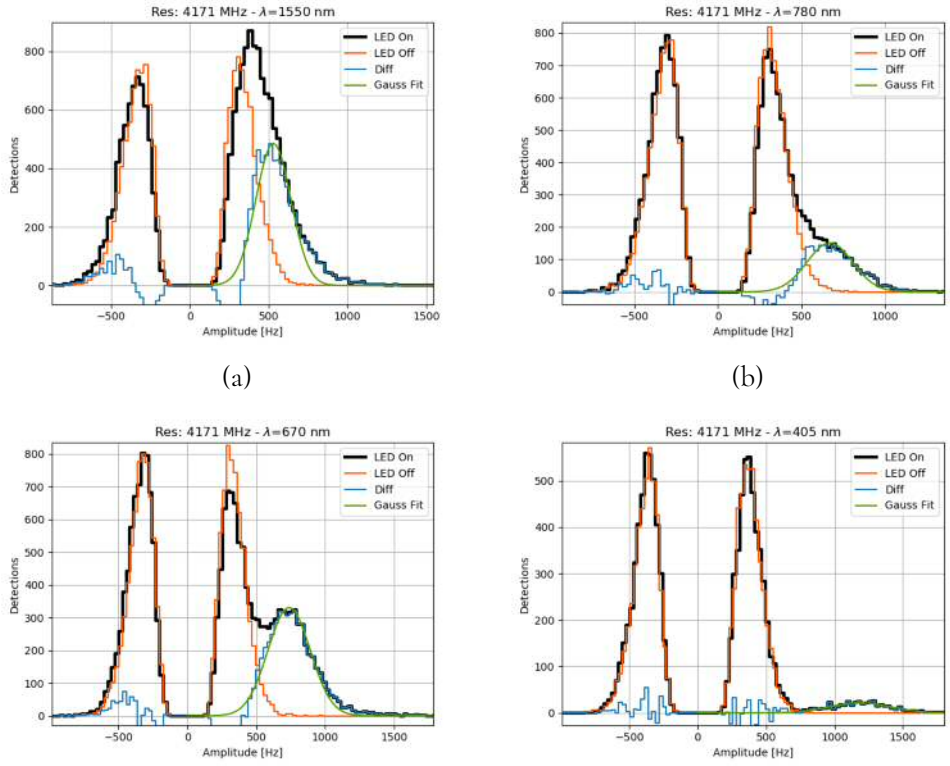

(a) (b)

(c) (d)

Figure 7.25: Extracted single-photon detections in resonator K010 with a) 1550 nm, b) 780 nm, c) 670 nm and d) 405 nm wavelengths.

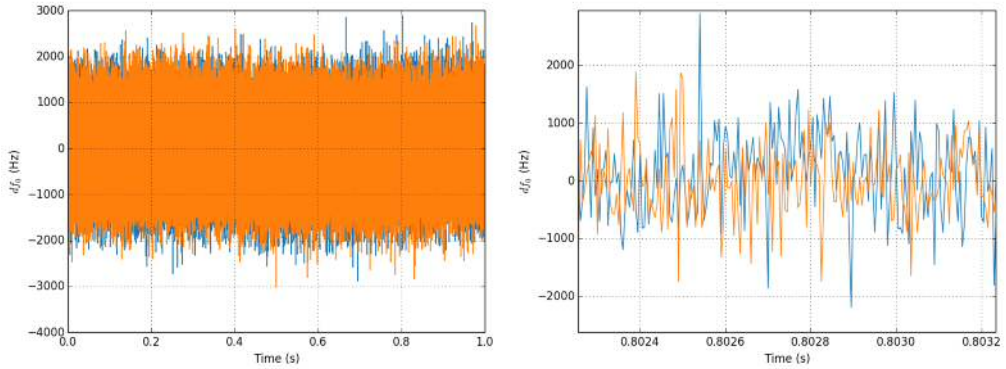

(a) (b)

Figure 7.26: Example time-stream capture with 405 nm LD on (blue) and off (orange) of resonator K011: a) full 1 s time-stream and b) zoomed version showing two absorption event responses.

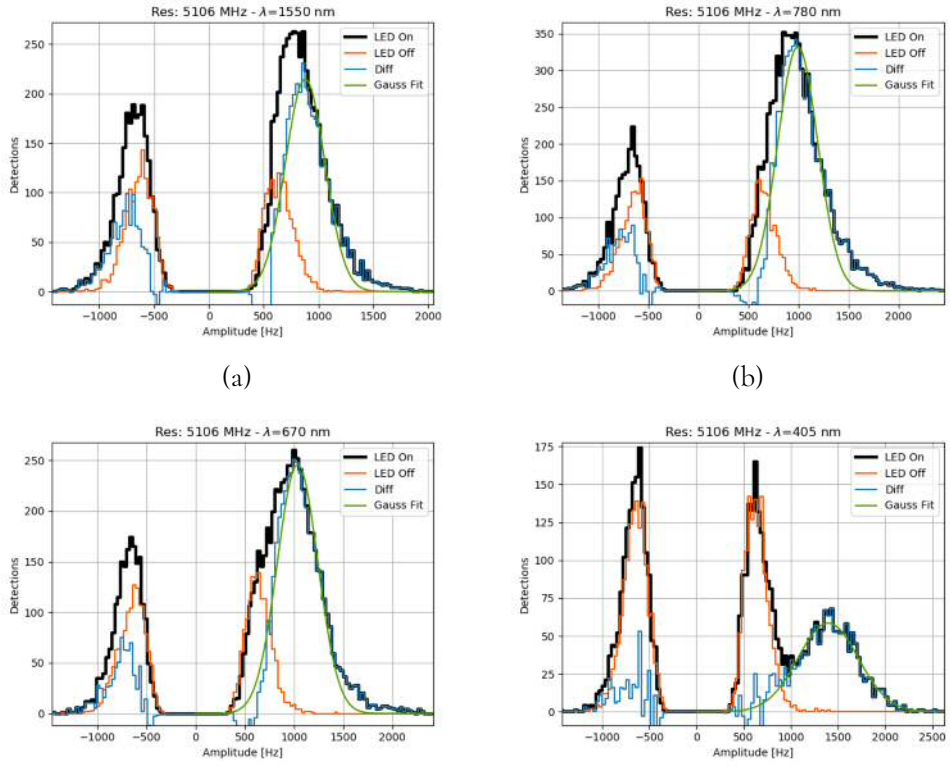

(a) (b)

(c) (d)

Figure 7.27: Extracted single-photon detections in resonator K011 with a) 1550 nm, b) 780 nm, c) 670 nm and d) 405 nm wavelengths.

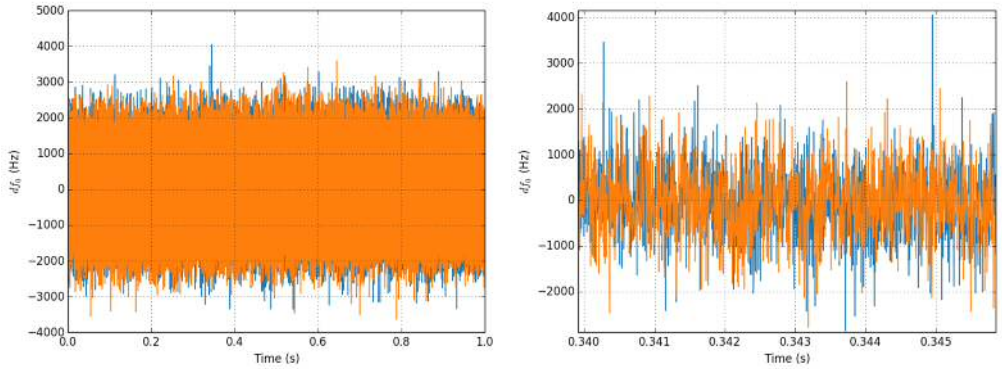

(a) (b)

Figure 7.28: Example time-stream capture with 405 nm LD on (blue) and off (orange) of resonator K012: a) full 1 s time-stream and b) zoomed version showing two absorption event responses.

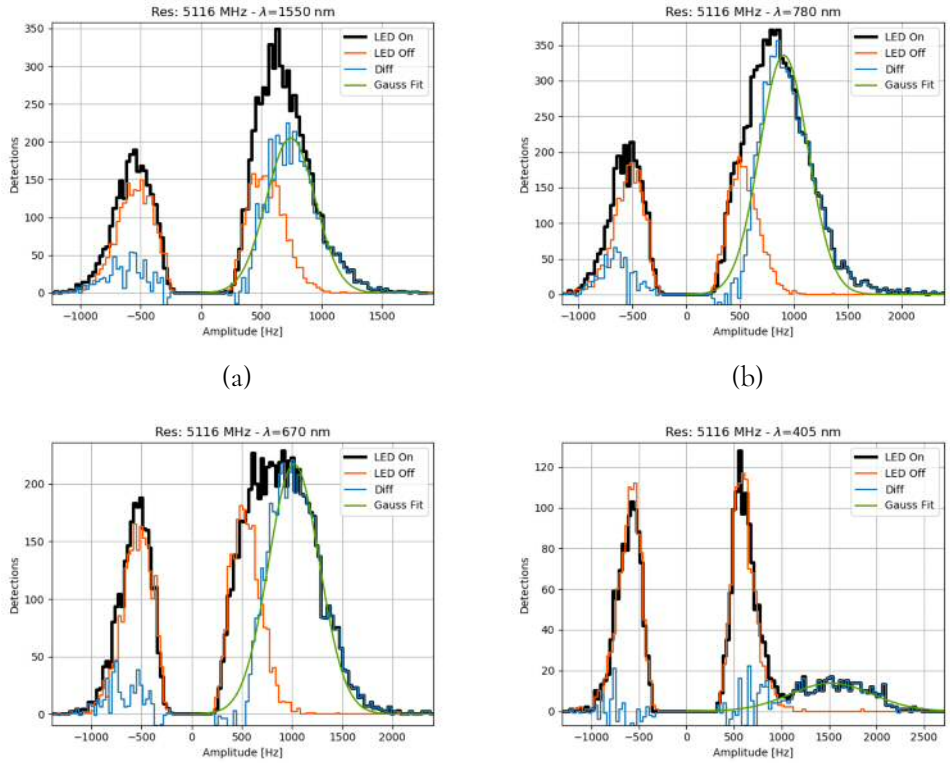

(a) (b)

(c) (d)

Figure 7.29: Extracted single-photon detections in resonator K012 with a) 1550 nm, b) 780 nm, c) 670 nm and d) 405 nm wavelengths.

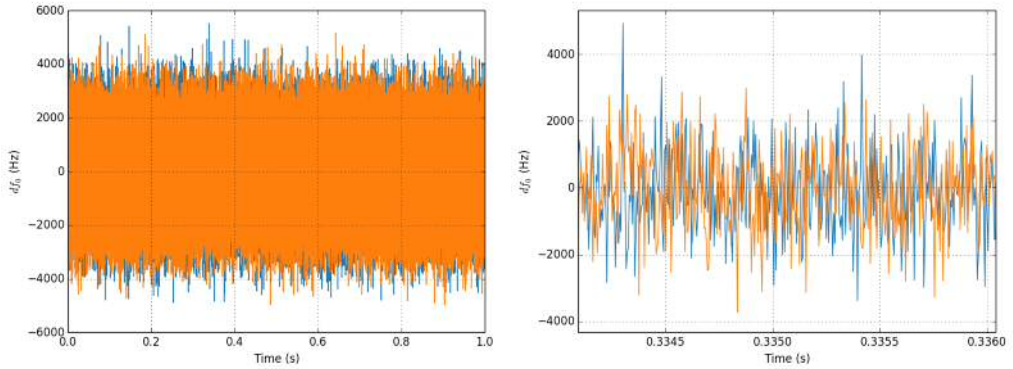

(a) (b)

Figure 7.30: Example time-stream capture with 405 nm LD on (blue) and off (orange) of resonator K014: a) full 1 s time-stream and b) zoomed version showing two absorption event responses.

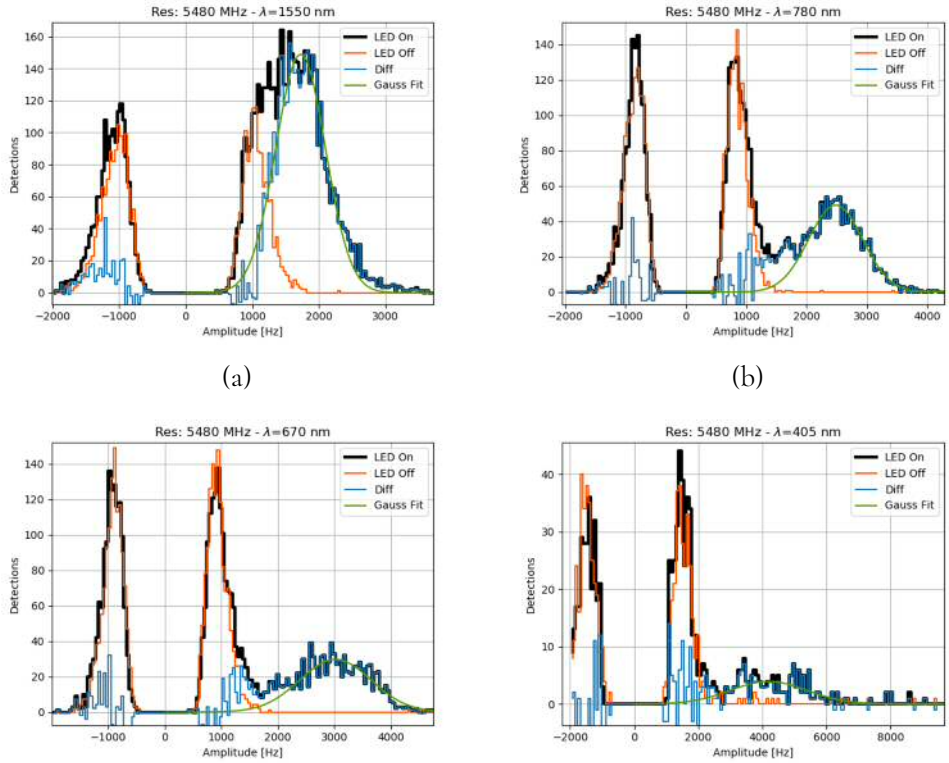

(a) (b)

(c) (d)

Figure 7.31: Extracted single-photon detections in resonator K014 with a) 1550 nm, b) 780 nm, c) 670 nm and d) 405 nm wavelengths.

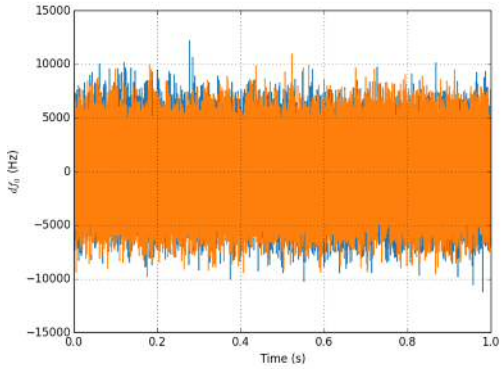

Figure 7.32: Example 1 s time-stream capture with 405 nm LD on (blue) and off (orange) of resonator K015.

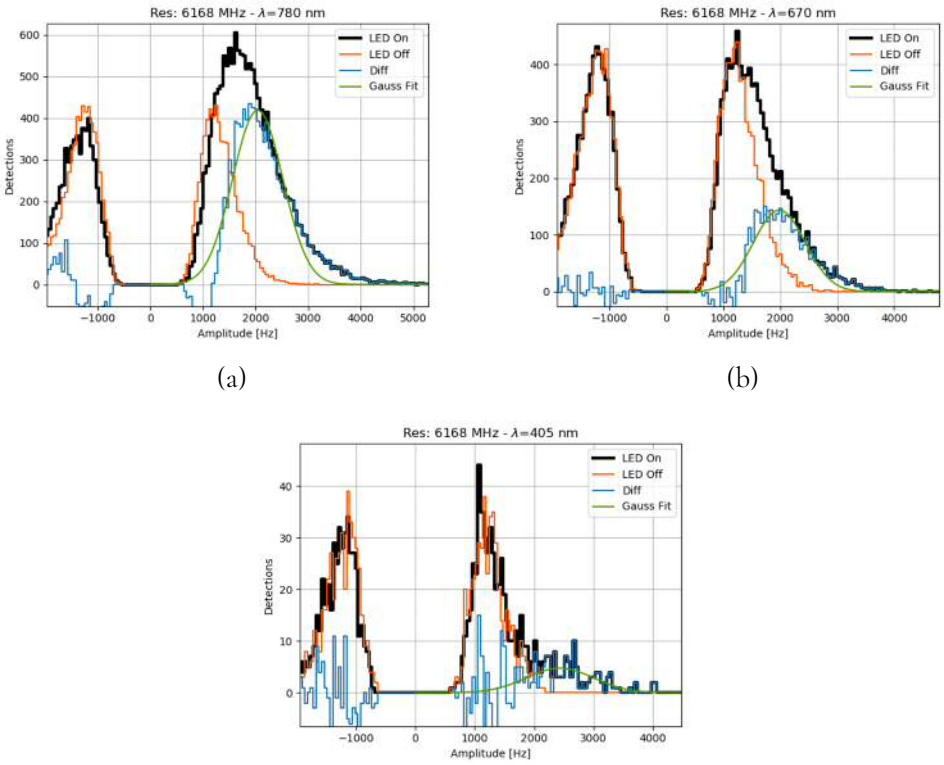

Figure 7.33: Extracted single-photon detections in resonator K015 with a) 780 nm, b) 670 nm and c) 405 nm wavelengths. Note data with 1550 nm diode was corrupted.

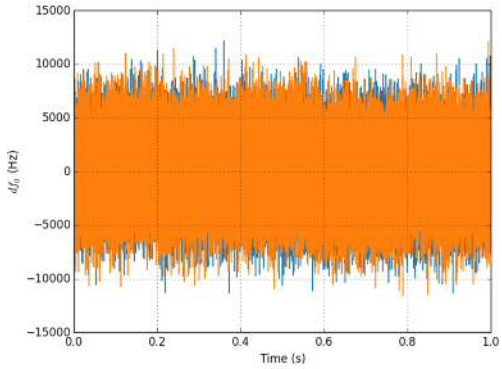

Figure 7.34: Example 1 s time-stream capture with 670 nm LD on (blue) and off (orange) of resonator K017.

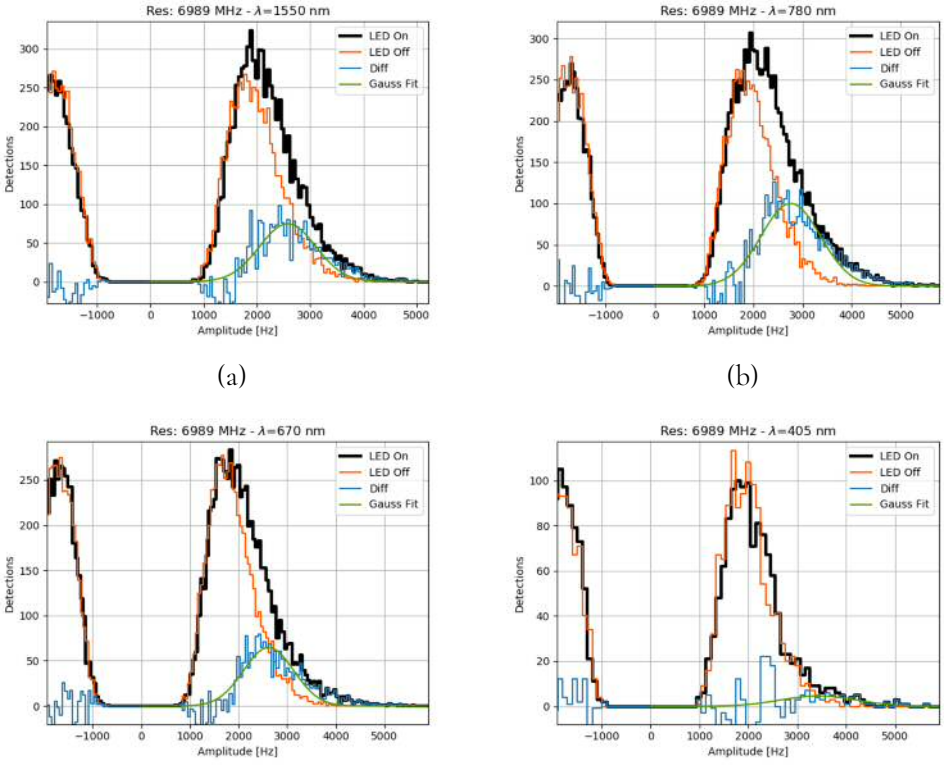

(a) (b)

(c) (d)

Figure 7.35: Extracted single-photon detections in resonator K017 with a) 1550 nm, b) 780 nm, c) 670 nm and d) 405 nm wavelengths.

7.4.3 Further Analysis

The best resonators were identified as having a clear linear response with photon energy; for all wavelengths. The responses can be seen in Figure 7.36. Note that

many other resonators show a linear response for the higher photon energy and it is possible some resonators are only capable of resolving two-photon or more absorption events at lower photon energies.

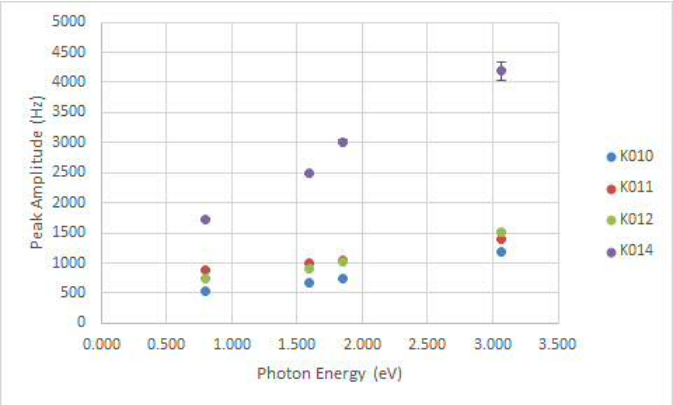

Figure 7.36: Plot of peak amplitude response as a function of photon energy. Error bars have been included for all data points but, as can be seen in table 7.4, they are mostly relatively small.

Figure 7.36 shows a mostly linear relationship between the peak amplitude extractions, from the Gaussian fitting, and the photon energy. The peak amplitude should correspond to $df_{0,max}$ from (3.10). The linearity in the responses - and the small error bars - show conclusive evidence these resonators are detecting single-photons but it is not clear which resonator belongs to which design. K014 has a much larger response compared to the other resonators analysed, suggesting it is one of the smaller volume devices. This would also make sense as it has a high resonant frequency. The similarity in response between K010, K011 and K012 would suggest these have a similar volume; with potentially an Al and hybrid pair.

The resolution is poor and not competitive with other energy-resolving detectors of the same regime. This can be seen in Figure 7.37. However, there has been some improvement upon the energy resolution quoted in Section 4.3.2. Although it is difficult to say which design these resonator belong to, it can be certain these are smaller volume devices; the lowest frequency devices had the pargest volumes

which were comparable to the test array detectors described in Section 4.1.3. This lends support for developing smaller volume devices.

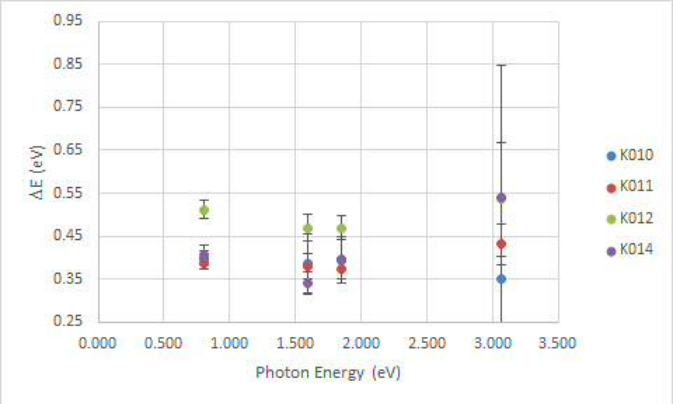

Figure 7.37: Plot of energy resolution as a function of photon energy.

Table 7.5: Table of energy resolution values from Figure 7.37.

	ΔE (eV)			
λ (nm)	1550	780	670	405
K010	0.395 ± 0.023	0.387 ± 0.031	0.392 ± 0.020	0.350 ± 0.068
K011	0.387 ± 0.014	0.379 ± 0.029	0.375 ± 0.024	0.432 ± 0.068
K012	0.511 ± 0.021	0.470 ± 0.031	0.469 ± 0.028	0.53 ± 0.13
K014	0.407 ± 0.022	0.341 ± 0.027	0.395 ± 0.054	0.54 ± 0.31

7.4.3.1 Evidence of Partial Responses

Of the resonators analysed further, there is some evidence of partial response, in that photon absorption has occured in regions of reduced current density. These are only observed in resonators which have a high responsivity and good enough energy resolution. Larger versions of the detection plots presented in Section 7.4.2 are shown here.

Figure 7.38 shows a broader tail on the left side the Gaussian. This is indicative of partial responses. For this resonator, only at the highest photon energy is this

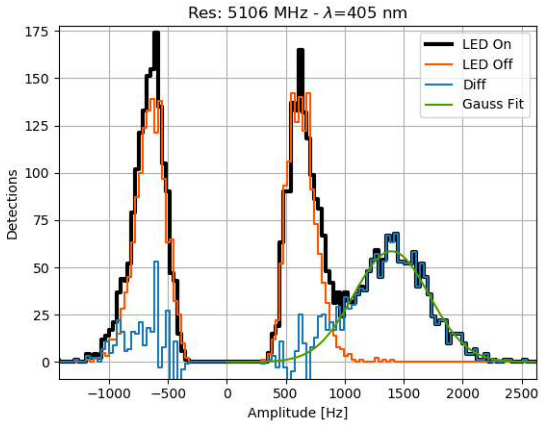

Figure 7.38: Detection extraction plot of K011 detecting 405 nm single-photons.

behaviour observed. This is likely due to the resonator not having a high enough response and so the partial responses are lost in the noise.

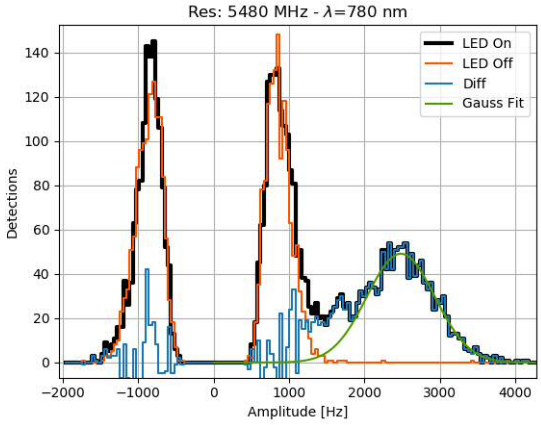

Figure 7.39: Detection extraction plot of K014 detecting 780 nm single-photons.

In Figure 7.39 the partial responses are more pronounced. This will be due to the detector having a higher responsivity. Note that the Gaussian is fitted to data points above 2000 Hz to counteract skewing from the long tail. As the photon energy increases, the effect of the partial responses becomes more pronounced. This can be seen in Figure 7.40. The distribution is much broader here, although there are also slightly fewer counts.

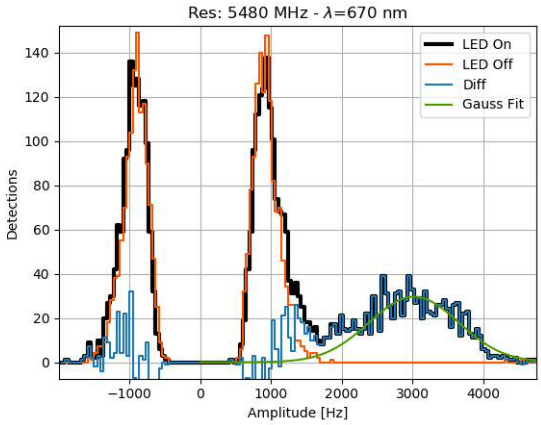

Figure 7.40: Detection extraction plot of K014 detecting 670 nm single-photons.

7.5 Discussion

The analysis of this test array has been severely limited by the inability to identify the resonators and further hindered by unreliable quasiparticle lifetime data. Without the quasiparticle saturation temperature, any modelling for the expected detector response is limited. Nonetheless, the results show conclusive evidence of single-photon detection in Al LEKIDs. At the very least, there are four resonators which show the expected linear response with incident photon energy. There is some small deviation from the linear trend for measurements made with the lowest photon energy. This could be due to the poor SNR: all measurements made with the 1550 nm had detections entangled within the noise. This may have skewed the fitting. The fitting may have also been skewed by potential, unresolved 2-photon absorption events. There are also many other resonators which show an apparent linear trend for the 780 nm, 670 nm ad 405 nm photons.

Notice that for some of the higher frequency detectors - see Figures 7.26b, 7.28b and 7.30b - it is difficult to clearly see the responses from absorption events. This may be due to those detectors having a fast quasiparticle lifetime. This can be

seen in Figure 7.41; a high energy cosmic ray response with very few data points in the pulse decay - indicating a fast decay time. Additionally, Figures 7.32 and 7.34 have no clear examples of absorption responses in the raw data. The accompanying extraction histograms suggest more data is required for thos detectors.

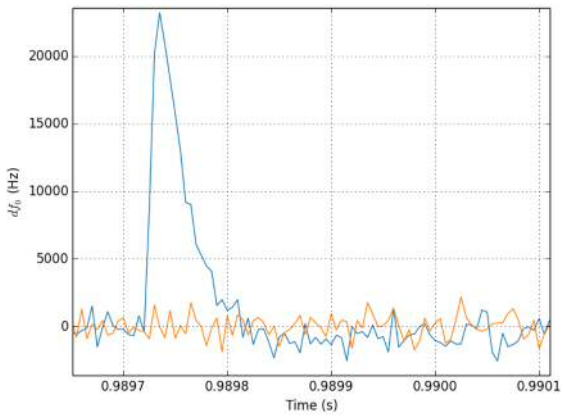

Figure 7.41: Example of a cosmic ray detection in K012.

The resonators evaluated in Section 7.4.3 also show an improved energy resolution upon the measurements made in Chapter 4. Here, the only difference we can be certain of is that the devices have a smaller volume. This is a clear demonstration of the need to work firmly below the expected GR noise limit.

The most interesting, and another first, is the demonstration of a broadened single-photon response due to partial responses. The simulations presented in Chapter 6 indicated that this could be due to a local response dependence within the meander as well as the IDC. Ideally, proper identification of the resonators would have shown this conclusively. Nonetheless, it is clearly a limiting factor of the energy resolution and will need to be addressed in future work. This could come in the form of modification to the meander design as in [86]; where uniform current density has been achieved within the meander by tapering the meander legs. Or the use of microlenses to focus light onto the array could also be used to

mitigate absoprtion in the IDC [87].

Chapter 8

Summary

The aim of the work presented in this thesis was to investigate the limits of single-photon detection in LEKIDs. Previous work with titanium nitride (TiN) KIDs [43, 42] have demonstrated single-photon detection in LEKIDs, with energy resolutions approaching the capability of TESs in the same regime (visible and near-infrared). However, both examples show a consistent deviation from the limit in energy resolution imposed by Poisson statistics. Given the consistency, it was apparent there may be some additional mechanism to single-photon detection that has been unaccounted for. This piece of work aimed to find the missing performance between the predictions and measurements.

A novel approach was taken by using Al LEKIDs in order to model single-photon detection using Mattis-Bardeen and Kaplan theory. TiN has been shown to deviate from conventional superconductivity theory so it is difficult to pin down the cause. Aluminium is not an optimal material for single-photon detection as it is highly reflective at visible wavelengths. However, the results presented in Chapter 4 show clear evidence of single-photon detection. The model and the limit in en-

ergy resolution described in Chapter 3 is shown to fit well with the measurements presented in Chapter 4. Those results are the first steps towards understanding the limits of single-photon detection in LEKIDs. The model required $\eta = 0.4$ for the 30 nm Al film of the device. This was the first known demonstration of work using a different value from the conventional $\eta = 0.57$. The modelling and measurements of Chapter 4 show that the quantum efficiency and the quasiparticle saturation temperature are the core limiting factors for single-photon detection in LEKIDs.

The method used to extract the single-photon responses - based on matched-filtering - was influenced by the methods used in [42]. The noisy data recorded from the test array presented in Chapter 4 motivated the further development of the extraction methods used in both Chapter 4 and Chapter 7 datasets.

The simulation work described in Chapter 6 and the results presented in Chapter 7 also show that partial responses are an artefact of LEKID architecture and must be taken into consideration. Single-photon detection requires high responsivity but this can leave the resonator susceptible to partial responses. The result can lead to a broadened energy resolution. Here, it has been shown smaller volume devices are likely to have less variation in response across the meander. However, a smaller volume will result in a higher responsivity by which photons absorbed in the IDC could generate measurable partial responses. Hence the novel concept of using an additional Nb absorbing layer covering the IDC regions of the devices in the test array was attempted.

The use of these hybrid structures has led to added complications to the test array design. Significant scatter in resonator position across the test array – thought to be due to processing effects – has made it difficult to reliably identify between Al only and hybrid (Al meander with NbAl IDC) devices. Here it should be noted

that the Al test array, used for the work presented in Chapter 4, was formed from a single deposition process that was then etched only to create the line features of the resonator design. Whereas any Al regions in the Chapter 7 test array had a Nb layer deposited in a second desposition process which was then removed after etching the resonator line features. It is likely both the second deposition and the removal processes have caused some, as yet, unquantifiable effect on the material. The result of this has meant only a very basic analysis of the data has been carried out. This said, conclusive evidence of single-photon detection in Al LEKIDs has been shown and a decrease in measured energy resolution (compared to measurements presented in Chapter 4) can be linked to a reduced detector volume.

Future work should entail a simplified test array design using the same resonator designs as those described in Chapter 5. A test array with easily identifiable resonators is required to probe the single-photon detection model that has been developed. A comparison between design and detector volumes will show any crucial gaps in the detection model. Another test array following the same array design fabricated from a single layer of Al should also be produced. Measurements from this can rule out most of the suspected processing effects that have hindered this work. After which, an optimised design iteration can be carried out.

Bibliography

[1] Christopher J. Chunnilall, Ivo Pietro Degiovanni, Stefan Kück, Ingmar Müller, and Alastair G. Sinclair. Metrology of single-photon sources and detectors: a review. *Optical Engineering*, 53:53 – 53 – 17, 2014.

[2] J. Sneider. Interactive extra-solar planets catalog. exoplanet.eu/catalog. Accessed: 30/08/2018.

[3] D. J. Cook, S. Schlemmer, N. Balucani, D. R. Wagner, B. Steiner, and R. J. Saykally. Infrared emission spectra of candidate interstellar aromatic molecules. *Nature*, 380:227, 1996.

[4] Lin Lin, Cheng Li, Yanqin He, Ting Xiao, and Enci Wang. Bar-induced central star formation as revealed by integral field spectroscopy from califa. *The Astrophysical Journal*, 838(2):105, 2017.

[5] KONG Xu, LIN Lin, LI Jin-rong, ZHOU Xu, ZOU Hu, LI Hong-yu, CHEN Fu-zhen, DU Wei, FAN Zhou, MAO Ye-wei, WANG Jing, ZHU Yi-nan, and ZHOU Zhi-min. Spectroscopic observations of the star formation regions in nearby galaxies. *Chinese Astronomy and Astrophysics*, 38(4):427 – 438, 2014.

[6] Michele Cappellari. Structure and kinematics of early-type galaxies from integral field spectroscopy. *Annual Review of Astronomy and Astrophysics*, 54(1):597–665, 2016.

[7] Jeffrey D. Crane, Steven R. Majewski, Helio J. Rocha-Pinto, Peter M. Frinchaboy, Michael F. Skrutskie, and David R. Law. Exploring halo substructure with giant stars: Spectroscopy of stars in the galactic anticenter stellar structure. *The Astrophysical Journal Letters*, 594(2):L119, 2003.

[8] M. Bonavita, R. U. Claudi, G. Tinetti, J. L. Beuzit, S. Desidera, R. Gratton, M. Kasper, and C. Mordasini. High contrast imaging: a new frontier for exoplanets search and characterization. *AIP Conference Proceedings*, 1094(1):429–432, 2009.

[9] Seth R. Meeker, Benjamin A. Mazin, Alex B. Walter, Paschal Strader, Neelay Fruitwala, Clint Bockstiegel, Paul Szypryt, Gerhard Ulbricht, Grégoire Coiffard, Bruce Bumble, Gustavo Cancelo, Ted Zmuda, Ken Treptow, Neal Wilcer, Giulia Collura, Rupert Dodkins, Isabel Lipartito, Nicholas Zobrist, Michael Bottom, J. Chris Shelton, Dimitri Mawet, Julian C. van Eyken, Gautam Vasisht, and Eugene Serabyn. Darkness: A microwave kinetic inductance detector integral field spectrograph for high-contrast astronomy. *Publications of the Astronomical Society of the Pacific*, 130(988):065001, 2018.

[10] N. Jovanovic, C. Schwab, N. Cvetojevic, O. Guyon, and F. Martinache. Enhancing stellar spectroscopy with extreme adaptive optics and photonics. *Publications of the Astronomical Society of the Pacific*, 128(970):121001, 2016.

[11] Julien Lozi, Nemanja Jovanovic, Olivier Guyon, Jared Males, Garima Singh, Danielle Doughty, Prashant Pathak, Sean Goebel, Tomoyuki Kudo, and Frantz

Martinache. Scexao: The first high contrast exoplanet imager on an elt? In *Adaptive Optics for Extremely Large Telescopes 4 - Conference Proceedings*. University of California Center for Adaptive Optics, 2015.

[12] David L. Fried. Probability of getting a lucky short-exposure image through turbulence*. *J. Opt. Soc. Am.*, 68(12):1651–1658, Dec 1978.

[13] Stefan Hippler, Carolina Bergfors, Brandner Wolfgang, Sebastian Daemgen, Thomas Henning, Felix Hormuth, Armin Huber, Markus Janson, Boyke Rochau, Ralf-Rainer Rohloff, and Karl Wagner. The astralux sur lucky imaging instrument at the ntt. *The Messenger*, 137:14–17.

[14] P. A. Oesch, G. Brammer, P. G. van Dokkum, G. D. Illingworth, R. J. Bouwens, I. Labbé, M. Franx, I. Momcheva, M. L. N. Ashby, G. G. Fazio, V. Gonzalez, B. Holden, D. Magee, R. E. Skelton, R. Smit, L. R. Spitler, M. Trenti, and S. P. Willner. A remarkably luminous galaxy at z=11.1 measured with hubble space telescope grism spectroscopy. *The Astrophysical Journal*, 819(2):129, 2016.

[15] F. Bouchy, D. Queloz, M. Deleuil, B. Loeillet, A. P. Hatzes, S. Aigrain, R. Alonso, M. Auvergne, A. Baglin, P. Barge, W. Benz, P. Bordé, H. J. Deeg, R. De la Reza, R. Dvorak, A. Erikson, M. Fridlund, P. Gondoin, T. Guillot, G. Hébrard, L. Jorda, H. Lammer, A. Léger, A. Llebaria, P. Magain, M. Mayor, C. Moutou, M. Ollivier, M. Pätzold, F. Pepe, F. Pont, H. Rauer, D. Rouan, J. Schneider, A. H. M. J. Triaud, S. Udry, and G. Wuchterl. Transiting exoplanets from the corot space mission* - iii. the spectroscopic transit of corot-exo-2b with sophie and harps. *A&A*, 482(3):L25–L28, 2008.

[16] Joanna K. Barstow, Neil E. Bowles, Suzanne Aigrain, Leigh N. Fletcher, Patrick G. J. Irwin, Ryan Varley, and Enzo Pascale. Exoplanet atmospheres with echo: spectral retrievals using echosim. *Experimental Astronomy*, 40(2):545–561, 2015.

[17] G. Tinetti, P. Drossart, P. Eccleston, P. Hartogh, A. Heske, J. Leconte, G. Micela, M. Ollivier, G. Pilbratt, L. Puig, D. Turrini, B. Vandenbussche, P. Wolkenberg, E. Pascale, J.-P. Beaulieu, M. Güdel, M. Min, M. Rataj, T. Ray, I. Ribas, J. Barstow, N. Bowles, A. Coustenis, V. Coudé du Foresto, L. Decin, T. Encrenaz, F. Forget, M Friswell, M. Griffin, P. O. Lagage, P. Malaguti, A. Moneti, J. C. Morales, E. Pace, M. Rocchetto, S. Sarkar, F. Selsis, W. Taylor, J. Tennyson, O. Venot, I. P. Waldmann, G. Wright, T. Zingales, and M. R. Zapatero-Osorio. The science of ariel (atmospheric remote-sensing infrared exoplanet large-survey), 2016.

[18] Sara Seager. The future of spectroscopic life detection on exoplanets. *Proceedings of the National Academy of Sciences*, 111(35):12634–12640, 2014.

[19] L. Pagnanini. Development of kinetic inductance detectors for cuore and lucifer. *Nuovo Cimento della Societa Italiana di Fisica C*, 38, 2015.

[20] B Seitz. Position sensitive photon detectors for nuclear physics, particle physics and healthcare applications. *Journal of Instrumentation*, 7(01):C01031, 2012.

[21] E. S. Battistelli, F. Bellini, C. Bucci, M. Calvo, L. Cardani, N. Casali, M. G. Castellano, I. Colantoni, A. Coppolecchia, C. Cosmelli, A. Cruciani, P. de Bernardis, S. Di Domizio, A. D'Addabbo, M. Martinez, S. Masi, L. Pagnanini, C. Tomei, and M. Vignati. Calder: neutrinoless double-beta decay identification in teo$$_2$$2bolometers with kinetic inductance detectors. *The European Physical Journal C*, 75(8):353, 2015.

[22] Hiroaki Shishido, Shigeyuki Miyajima, Yoshito Narukami, Kenichi Oikawa, Masahide Harada, Takayuki Oku, Masatoshi Arai, Mutsuo Hidaka, Akira Fujimaki, and Takekazu Ishida. Neutron detection using a current biased kinetic inductance detector. *Applied Physics Letters*, 107(23):232601, 2015.

[23] A. Giachero, P. K. Day, P. Falferi, M. Faverzani, E. Ferri, C. Giordano, M. Maino, B. Margesin, R. Mezzena, R. Nizzolo, A. Nucciotti, A. Puiu, and L. Zanetti. Development of microwave superconducting microresonators for neutrino mass measurement in the holmes framework. *Journal of Low Temperature Physics*, 184(1):123–130, 2016.

[24] James G. Fujimoto, Costas Pitris, Stephen A. Boppart, and Mark E. Brezinski. Optical coherence tomography: An emerging technology for biomedical imaging and optical biopsy. *Neoplasia (New York, N.Y.)*, 2:9–25, 2000.

[25] Georgeta Crivat and Justin W. Taraska. Imaging proteins inside cells with fluorescent tags. *Trends in biotechnology*, 30:8–16, 2012.

[26] K. Inderbitzin, A. Engel, and A. Schilling. Soft x-ray single-photon detection with superconducting tantalum nitride and niobium nanowires. *IEEE Transactions on Applied Superconductivity*, 23(3):2200505–2200505, 2013.

[27] S. Komiyama, O. Astafiev, V. Antonov, T. Kutsuwa, and H. Hirai. A single-photon detector in the far-infrared range. *Nature*, 403:405–407, 2000.

[28] G. S. Buller and R. J. Collins. Single-photon generation and detection. *Measurement Science and Technology*, 21(1):012002, 2010.

[29] Aaron J. Miller, Sae Woo Nam, John M. Martinis, and Alexander V. Sergienko. Demonstration of a low-noise near-infrared photon counter with multiphoton discrimination. *Applied Physics Letters*, 83(4):791–793, 2003.

[30] Sander Nugraha Durenbos. *Superconducting Single Photon Detectors*. PhD thesis, Technische Universiteit Delft, Netherlands, 2011.

[31] M. D. Eisaman, J. Fan, A. Migdall, and S. V. Polyakov. Invited review article: Single-photon sources and detectors. *Review of Scientific Instruments*, 82(7):071101, 2011.

[32] Eric A. Dauler, Matthew E. Grein, Andrew J. Kerman, Francesco Marsili, Shigehito Miki, Sae Woo Nam, Matthew D. Shaw, Hirotaka Terai, Varun B. Verma, and Taro Yamashita. Review of superconducting nanowire single-photon detector system design options and demonstrated performance. *Optical Engineering*, 53:53 – 53 – 13, 2014.

[33] B. Cabrera, R. M. Clarke, P. Colling, A. J. Miller, S. Nam, and R. W. Romani. Detection of single infrared, optical, and ultraviolet photons using superconducting transition edge sensors. *Applied Physics Letters*, 73(6):735–737, 1998.

[34] Adriana E. Lita, Aaron J. Miller, and Sae Woo Nam. Counting near-infrared single-photons with 95% efficiency. *Opt. Express*, 16(5):3032–3040, 2008.

[35] Robert H. Hadfield. Single-photon detectors for optical quantum information applications. *Nature Photonics*, 3:696.

[36] Blas Cabrera, Roland Clarke, Aaron Miller, Sae Woo Nam, Roger Romani, Tarek Saab, and Betty Young. Cryogenic detectors based on superconducting transition-edge sensors for time-energy-resolved single-photon counters and for dark matter searches. *Physica B: Condensed Matter*, 280(1):509 – 514, 2000.

[37] Peter C. Nagler, Matthew A Greenhouse, S. Harvey Moseley, Bernard J. Rauscher, and John E. Sadleir. Development of transition edge sensor detectors optimized for single-photon spectroscopy in the optical and near-infrared, 2018.

[38] Dongdong Jin, Huijun Hu, Xinbo Chu, Wencong Wang, Yuxiang Luo, Shukun Sun, and Shipei Shao. The development of x-ray single photon detector, 2017. Selected Papers of the Chinese Society for Optical Engineering Conferences held October and November 2016.

[39] P. D. Mauskopf. Transition edge sensors and kinetic inductance detectors in astronomical instruments. *Publications of the Astronomical Society of the Pacific*, 130(990):082001, 2018.

[40] A. D. Semenov, P. Haas, B. Günther, H.-W. Hübers, K. Il'in, and M. Siegel. Energy resolution of a superconducting nanowire single-photon detector. *Journal of Low Temperature Physics*, 151:564–569, 2008.

[41] A. Peacock, P. Verhoeve, N. Rando, A. van Dordrecht, B. G. Taylor, C. Erd, M. A. C. Perryman, R. Venn, J. Howlett, D. J. Goldie, J. Lumley, and M. Wallis. On the detection of single optical photons with superconducting tunnel junction. *Journal of Applied Physics*, 81(11):7641–7646, 1997.

[42] W. Guo, X. Liu, Y. Wang, Q. Wei, L. F. Wei, J. Hubmayr, J. Fowler, J. Ullom, L. Vale, M. R. Vissers, and J. Gao. Counting near infrared photons with microwave kinetic inductance detectors. *Applied Physics Letters*, 110(21):212601, 2017.

[43] B. A. Mazin, S. R. Meeker, M. J. Strader, P. Szypryt, D. Marsden, J. C. van Eyken, G. E. Duggan, A. B. Walter, G. Ulbricht, M. Johnson, B. Bumble, K. O'Brien, and C. Stoughton. Arcons: A 2024 pixel optical through near-ir cryogenic imaging spectrophotometer. *Publications of the Astronomical Society of the Pacific*, 125(933):1348–1361, 2013.

[44] Henry G. Leduc, Bruce Bumble, Peter K. Day, Byeong Ho Eom, Jiansong Gao, Sunil Golwala, Benjamin A. Mazin, Sean McHugh, Andrew Merrill, David C. Moore, Omid Noroozian, Anthony D. Turner, and Jonas Zmuidzinas. Titanium nitride films for ultrasensitive microresonator detectors. *Applied Physics Letters*, 97(10):102509, 2010.

[45] J. Bardeen, L. N. Cooper, and J. R. Schrieffer. Microscopic theory of superconductivity. *Phys. Rev.*, 106:162–164, Apr 1957.

[46] Leon N. Cooper. Bound electron pairs in a degenerate fermi gas. *Phys. Rev.*, 104:1189–1190, Nov 1956.

[47] Philip Hofmann. *Solid State Physics: An introduction*. Wiley-VCH, 2008.

[48] J. R. Hook and H. E. Hall. *Solid State Physics*. John Wiley & Sons, 2nd edition, 1991.

[49] T. Van Duzer and C. W. Turner. *Principles of Superconductive Devices and Circuits*. Edward Arnold Limited, 1981.

[50] C.J Gorter and H Casimir. On supraconductivity i. *Physica*, 1(1):306 – 320, 1934.

[51] John Bardeen. Two-fluid model of superconductivity. *Phys. Rev. Lett.*, 1:399–400, Dec 1958.

[52] F. London and H. London. The electromagnetic equations of the supraconductor. *Proceedings of the Royal Society of London A: Mathematical, Physical and Engineering Sciences*, 149(866):71–88, 1935.

[53] S. M. Doyle. *Lumped Element Kinetic Inductance Detectors*. PhD thesis, Cardiff University, United Kingdom, 2008.

[54] D. C. Mattis and J. Bardeen. Theory of the anomalous skin effect in normal and superconducting metals. *Phys. Rev.*, 111:412–417, 1958.

[55] B. Geilikman and V. Kresin. *Kinetic and Nonsteady-state effects in Superconductors*. John Wiley and sons, 1974.

[56] P. J. De Visser. *Quasiparticle Dynamics in Aluminium Supeconducting Microwave Resonators*. PhD thesis, Technische Universiteit Delft, Netherlands, 2014.

[57] S. B. Kaplan, C. C. Chi, D. N. Langenberg, J. J. Chang, S. Jafarey, and D. J. Scalapino. Quasiparticle and phonon lifetimes in superconductors. *Phys. Rev. B*, 14:4854–4873, 1976.

[58] Benjamin A. Mazin. *Microwave Kinetic Inductance Detectors*. PhD thesis, California Institute of Technology, United States - California, 2004.

[59] David M. Pozar. *Microwave Engineering*. John Wiley and sons, 2012.

[60] Peter Stuart Barry. *On the Development of SuperSpec; A Fully Integrated On-Chip Spectrometer for Far-Infrared Astronomy*. PhD thesis, Cardiff University, United Kingdom, 2014.

[61] J. Gao, J.and Zmuidzinas, A. Vayonakis, P. Day, B. Mazin, and H. Leduc. Equivalence of the effects on the complex conductivity of superconductor due to temperature change and external pair breaking. *Journal of Low Temperature Physics*, 151(1):557–563, 2008.

[62] A. V. Sergeev, V. V. Mitin, and B. S. Karasik. Ultrasensitive hot-electron kinetic-inductance detectors operating well below the superconducting transition. *Applied Physics Letters*, 80(5):817–819, 2002.

[63] P. J. de Visser, J. J. A. Baselmans, P. Diener, S. J. C. Yates, A. Endo, and T. M. Klapwijk. Generation-recombination noise: The fundamental sensitivity limit for kinetic inductance detectors. *Journal of Low Temperature Physics*, 167(3):335–340, 2012.

[64] P. D. Mauskopf, S. Doyle, P. Barry, S. Rowe, A. Bidead, P. A. R. Ade, C. Tucker, E. Castillo, A. Monfardini, J. Goupy, and M. Calvo. Photon-noise limited performance in aluminum lekids. *Journal of Low Temperature Physics*, 176(3):545–552, 2014.

[65] U. Fano. Ionization yield of radiations. ii. the fluctuations of the number of ions. *Phys. Rev.*, 72:26–29, 1947.

[66] T Guruswamy, D J Goldie, and S Withington. Quasiparticle generation efficiency in superconducting thin films. *Superconductor Science and Technology*, 27(5):055012, 2014.

[67] T Guruswamy, D J Goldie, and S Withington. Nonequilibrium superconducting thin films with sub-gap and pair-breaking photon illumination. *Superconductor Science and Technology*, 28(5):054002, 2015.

[68] P. J. de Visser, S. J. C. Yates, T. Guruswamy, D. J. Goldie, S. Withington, A. Neto, N. Llombart, A. M. Baryshev, T. M. Klapwijk, and J. J. A. Baselmans. The non-equilibrium response of a superconductor to pair-breaking radiation measured over a broad frequency band. *Applied Physics Letters*, 106(25):252602, 2015.

[69] Josie Dzifa Akua Parrianen, Andreas Papageorgiou, Simon Doyle, and Enzo Pascale. Modelling the performance of single-photon counting kinetic inductance detectors. *Journal of Low Temperature Physics*, 193(3):113–119, 2018.

[70] Peter K. Day, Henry G. LeDuc, Benjamin A. Mazin, Anastasios Vayonakis, and Jonas Zmuidzinas. A broadband superconducting detector suitable for use in large arrays. *Nature*, 425:817–821, 2003.

[71] M. Griffin, J. Baselmans, A. Baryshev, S. Doyle, M. Grim, P. Hargrave, T. Klapwijk, J. Martin-Pintado, A. Monfardini, A. Neto, H. Steenbeek, I. Walker, K. Wood, A. D'Addabbo, P. Barry, A. Bideaud, B. Blázquez, J. Bueno, M. Calvo, J-L. Costa-Kramer, L. Ferrari, A. Gómez-Gutiérrez, J. Goupy, N. Llombart, and S. Yates. Spacekids: kinetic inductance detectors for space applications, 2016.

[72] Jiansong Gao. *The Physics of Superconducting Microwave Resonators*. PhD thesis, California Institute of Technology, United States - California, 2008.

[73] T. Lindström, J. E. Healey, M. S. Colclough, C. M. Muirhead, and A. Ya. Tzalenchuk. Properties of superconducting planar resonators at millikelvin temperatures. *Phys. Rev. B*, 80:132501, 2009.

[74] J. Hubmayr, J. Beall, D. Becker, H.-M. Cho, M. Devlin, B. Dober, C. Groppi, G. C. Hilton, K. D. Irwin, D. Li, P. Mauskopf, D. P. Pappas, J. Van Lanen, M. R. Vissers, Y. Wang, L. F. Wei, and J. Gao. Photon-noise limited sensitivity in titanium nitride kinetic inductance detectors. *Applied Physics Letters*, 106(7):073505, 2015.

[75] L. Cardani, N. Casali, I. Colantoni, A. Cruciani, F. Bellini, M. G. Castellano, C. Cosmelli, A. D'Addabbo, S. Di Domizio, M. Martinez, C. Tomei, and M. Vignati. High sensitivity phonon-mediated kinetic inductance detector with combined amplitude and phase read-out. *Applied Physics Letters*, 110(3):033504, 2017.

[76] Simon Doyle, Philip Mauskopf, Jin Zhang, Stafford Withington, David Goldie, Dorota Glowacka, Alessandro Monfardini, Loren Swenson, and Markus Roesch. Optimisation of lumped element kinetic inductance detectors for use in ground based mm and sub-mm arrays. *AIP Conference Proceedings*, 1185(1):156–159, 2009.

[77] O. Noroozian, P. K. Day, B. H. Eom, H. G. Leduc, and J. Zmuidzinas. Crosstalk reduction for superconducting microwave resonator arrays. *IEEE Transactions on Microwave Theory and Techniques*, 60(5):1235–1243, 2012.

[78] S. Wuensch, C. Groetsch, M. Merker, and M. Siegel. Optimized lekid structures with low crosstalk for large detector arrays. *IEEE Transactions on Applied Superconductivity*, 25(3):1–5, 2015.

[79] J. Gao, M. R. Vissers, M. O. Sandberg, F. C. S. da Silva, S. W. Nam, D. P. Pappas, D. S. Wisbey, E. C. Langman, S. R. Meeker, B. A. Mazin, H. G. Leduc, J. Zmuidzinas, and K. D. Irwin. A titanium-nitride near-infrared kinetic inductance photon-counting detector and its anomalous electrodynamics. *Applied Physics Letters*, 101(14):142602, 2012.

[80] P. Szypryt, B. A. Mazin, G. Ulbricht, B. Bumble, S. R. Meeker, C. Bockstiegel, and A. B. Walter. High quality factor platinum silicide microwave kinetic inductance detectors. *Applied Physics Letters*, 109(15):151102, 2016.

[81] P. Szypryt, S. R. Meeker, G. Coiffard, N. Fruitwala, B. Bumble, G. Ulbricht, A. B. Walter, M. Daal, C. Bockstiegel, G. Collura, N. Zobrist, I. Lipartito, and B. A. Mazin. Large-format platinum silicide microwave kinetic inductance detectors for optical to near-ir astronomy. *Opt. Express*, 25(21):25894–25909, 2017.

[82] Christophe Peroz and Catherine Villard. Flux flow properties of niobium thin films in clean and dirty superconducting limits. *Phys. Rev. B*, 72:014515, 2005.

[83] J. J. A. Baselmans and S. J. C. Yates. Long quasiparticle lifetime in aluminum microwave kinetic inductance detectors using coaxial stray light filters. *AIP Conference Proceedings*, 1185(1):160–163, 2009.

[84] Sonnet Software Inc. 13th edition, 2011.

[85] S. Y. Hsieh and James L. Levine. Diffusion of quasiparticles in superconducting aluminum films. *Phys. Rev. Lett.*, 20:1502–1504, 1968.

[86] Danica Marsden, Benjamin A. Mazin, Bruce Bumble, Seth Meeker, Kieran O'Brien, Sean McHugh, Matthew Strader, and Eric Langman. Optical lumped element microwave kinetic inductance detectors. *Proc. SPIE 8453, High Energy, Optical and Infrared Detectors for Astronomy V*, 8453, 2012.

[87] Benjamin A. Mazin, Kieran O'Brien, Sean McHugh, Bruce Bumble, David Moore, Sunil Golwala, and Jonas Zmuidzinas. Archons: a highly multplexed superconducting optical to near-ir camera. *Proc. SPIE 7735, Ground-based and Airborne Instrumentation for Astronomy III*, 7735, 2010.